COMPREHENSIVE CHARACTERIZATION OF SHALE GAS SEEPAGE IN NANOSCALE ORGANIC-RICH SHALES

By

© 2020

Di Chai

Submitted to the graduate degree program in Chemical and Petroleum Engineering Department and the Graduate Faculty of the University of Kansas in partial fulfillment of the requirements for the degree of Doctor of Philosophy.

Chair: Dr. Xiaoli Li

Dr. Shapour Vossoughi

Dr. Kyle Camarda

Dr. Jyun-Syung Tsau

Dr. Huazhen Fang

Date Defended: August 19th, 2020

The dissertation committee for Di Chai certifies that this is the approved version of the following dissertation:

Comprehensive Characterization of Shale Gas Seepage in Nanoscale Organic-Rich Shales

Chair: Dr. Xiaoli Li

Date Approved: August 19th, 2020

ABSTRACT

Unlike conventional gas reservoirs, the shale gas resources are widely distributed in organic-rich shale formations with most pore sizes down to nanoscale. Such nanoscale confinement has invalidated the conventional gas transport mechanisms which are characterized by the Navier-Stokes equations. A common practice in shale reservoir simulation, which arbitrarily increases intrinsic matrix permeability to match the production data, has been proven inefficient and unreliable. This research work aims to bridge the gap in scientific understanding of the shale gas transport across the hierarchical structures of organic-rich matrix by developing different analytical and numerical models which incorporate various mechanisms in shale formations. More specifically, this work explores the qualitative and quantitative influences of the rarefaction effect, real gas effect, multilayer adsorption, surface diffusion, nano-confinement effect, and pore-structure heterogeneity on the shale gas flow.

First, a new unified gas transport model is developed by modifying Bravo's model to describe the rarefaction which is commonly in presence in nanopores. Particularly, a straight capillary tube is characterized by a conceptual layered model consisting of a viscous flow zone, a Knudsen diffusion zone, and a surface diffusion zone. To specify the contributions of the viscous flow and the Knudsen diffusion, the virtual boundary between the viscous flow and Knudsen diffusion zones is firstly determined based on Kennard's analytical kinetics approach. Then, the model considers the real gas effect, multilayer adsorption and nano-confinement effect to quantify the density oscillation and phase behavior in confined nanopores. Meanwhile, the apparent permeability (AP) model is analytically derived and numerically simulated at core-scale. In addition, the field scale production rate is numerically calculated by coupling the nanoscale mechanisms. Furthermore, the

pore-structure heterogeneity impact on production rate is studied by the fuzzy statistical method in which the Monte Carlo simulation is implemented for the sensitivity analyses of the structural parameters in the fractal model.

The proposed analytical model has been successfully validated against molecular dynamic simulation and experimental flux results for five types of gases (i.e., methane, nitrogen, helium, argon, and oxygen) with the assistance of optimization methods. One of the advantages of the new unified gas transport model is its great flexibility which is capable to cover the full flow regimes. It is found that the increase of real gas viscosity can reduce the total molar flux in the inorganic pores up to 66.0%. In addition, it is observed that the pore confinement effect is of importance when the pore size is smaller than 50 nm. The apparent permeability is found to increase greatly as the adsorption layer number increases, implying that the application of Langmuir model in existing gas transport models may substantially underestimate it. Given organic nanopores, the contribution of surface diffusion is tangible when the pore size is below 150 nm and the Knudsen diffusion is negligible under high pressures. Compared with the flow mechanisms in the nanopores, it is found that the fractal dimension of the tortuosity has the largest impact on the production rate than the pore size and the fractal dimension of pore size distribution. In addition, the fuzzy statistical method can quantify the confidence interval within which the satisfactory flow rate results can be acquired. The fuzzy statistical method enables more flexibility to predict the realistic production profile with significant data fluctuations.

ACKNOWLEDGEMENTS

I would like to express my earnest gratitude and respect to my academic supervisor, Prof. Xiaoli Li, who offers me the precious opportunity, generous financial support, and inspirational guidance during my graduate study at University of Kansas. In addition to her invaluable technical instructions, I also appreciate her mentorship in my life such as the capability of problem-solving, the communication skills, and the critical thinking.

I expand my thanks to University of Kansas and scholarship donors for the financial support during my graduate study. Moreover, I appreciate the help and support from all the committee members, faculty and staff members in Chemical and Petroleum Engineering Department. In addition, I thank the scholars outside the department to selflessly inspire and instruct me including but not limited to: Prof. Paul Cazeaux and Prof. Xuemin Tu from the Department of Mathematics, Prof. Chi Zhang from the Department of Geology, Prof. Bao Jia from University of North Dakota, Dr. Wennan Long from Stanford University, Dr. Ying Gao from Imperial College London, Dr. Xutao You and Prof. Jianyi Liu from Southwest Petroleum University, Prof. Yuliang Su and Prof. Wendong Wang from China University of Petroleum (East), Prof. Keliu Wu from China University of Petroleum (Beijing). I am truly thankful to the past and present research group members including: Prof. Baohui Wang, Dr. Gang Yang, Dr. Ruyi Zheng, Dr. Xuejia Du, Dr. Zhixing Wang, Dr. Yang Zheng, Dr. Wenli Qiao, Dr. Junchen Lv, Mrs. Julia Espinoza Mejia, and Mr. Yuhao Yang for their technical discussions and companions during my graduate study.

Last but not the least, I am deeply indebted to my dear fiancée, Dr. Jing Fu, for her unfailing love, endless patience, tremendous support, and strong belief in me during my tough times.

DEDICATION

This dissertation is dedicated to my dearest parents, Mr. Jian Chai and Mrs. Yuhua Li, my beloved fiancée, Dr. Jing Fu, all my dear family members and friends who have cared, encouraged and inspired me in the past.

TABLE OF CONTENTS

LIST OF FIGURES

LIST OF TABLES

CHAPTER 1: INTRODUCTION

1.1 Problem Statement and Significance

The hydrocarbons in the form of liquid and gas extracted from the petroleum reservoir have been serving as a key enabler of living standards providing reliable and steady energy supply. Nonetheless, the consensus has been reached that the fuel switching from crude oil to natural gas (mainly methane) for power generation has beneficial impacts on controlling the greenhouse gas (GHG) emissions due to the superior burning efficiency and less CO_2 production (Zoback and Arent, 2014). According to 2018 Energy Information Administration (EIA) as illustrated in Figure 1.1, the production of shale gas plays will be the largest contributor to natural gas production growth in terms of both optimistic and reserved projections, accounting for more than three-quarters of the U.S. natural gas production by 2050. Moreover, the large-scale commercial development of shale gas has catalyzed the renaissance of U.S. manufacturing from revitalizing the chemical industry to boosting job creations, which is vital to the economy (Hughes, 2013).

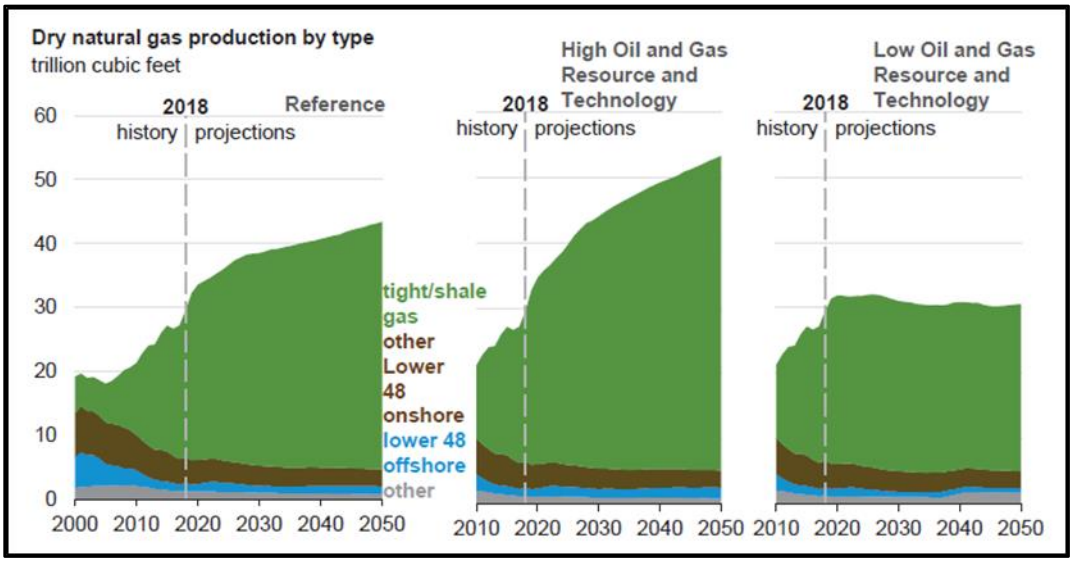

Figure 1.1: Schematic diagram showing that U.S. dry natural gas production increases as a result of continued development of tight and shale resources (EIA, 2018).

Unlike conventional gas reservoirs, the shale gas resources are widely distributed in organic-rich shale formations with most pore sizes down to nanoscale. Such nanoscale confinement has invalidated the conventional gas transport mechanisms (Ambrose et al., 2012). It is commonly observed that the shale gas production rate declines rapidly after the peak in early time, and then enters the long-tail production phase of low rates that may span up to a decade (Middleton et al., 2017). As a matter of fact, the total gas production is typically controlled by the long-term tail production rate which is contributed by the slow gas transport in matrix (Zhao and Alexandroff, 2019). Hence, it is essential to deepen the comprehensive understanding of transport mechanisms in nanoscale shale matrix and enrich the knowledge of the interaction between the slow gas transport at fine-scale level and ultimate production rate at coarse-scale level. However, it is still challenging to establish the fundamental theories of the shale gas transport through a hierarchy of scales.

1.2 Research Objective and Scope

The overall objective of this dissertation is to study single-phase gas flow behaviors across the hierarchical structures of organic-rich matrix in a hybrid framework including both numerical and analytical approaches. More specifically, the research scope can be categorized as following aspects:

1) Gas flow in nano-pores of the shale matrix is significantly different from that in macropores of the conventional reservoir. Thus, it is necessary to gain a holistic knowledge of flow behaviors at fine-scale pore level (i.e., organic and inorganic nanopores) and analytically characterize the gas transport coupling multiple mechanisms in confined nanopores;

2) Reasonably upscale the gas transport from the pore scale to the matrix scale (i.e., core and field) and facilitate the simulations using the empirical correlations;

3) Study shale gas production performance coupling fine-scale phenomena and expand our understanding of structural heterogeneity effects on the gas transport for improved prediction of the fate of methane and its management.

1.3 Outline of the Dissertation

The dissertation is organized by multiple tasks which are presented in Figure 1.2. Several tasks have been assigned to each chapter for the detailed descriptions. According to Figure 1.2, the fine scale transport is mainly studied in Chapter 1 and 2. Chapter 1 provides the method to develop a new analytical model which can fully depict the flow behaviors in nanopores under reservoir condition. Meanwhile, rarefaction effect, pore roughness, real gas effect, monolayer adsorption, and surface diffusion are considered in the model. Chapter 2 provides a more complicated analytical model based on Chapter 1 to incorporate the multilayer adsorption and pore confinement effect. In contrast, the coarse scale transport is investigated in Chapter 3 and 4. In Chapter 3, one numerical scheme coupling the pore-scale analytical model is adopted to implement the spatial-temporal simulation at core level during the pulse-decay test. In Chapter 4, a fractal model incorporating the pore-scale analytical model is utilized to simulate the unit matrix in shale formation. Then, the sector model is adopted to couple each unit matrix and the hydraulic fracture for the gas production simulation in field. Finally, the heterogeneity of structural parameters in fractal model is evaluated by the fuzzy statistical method.

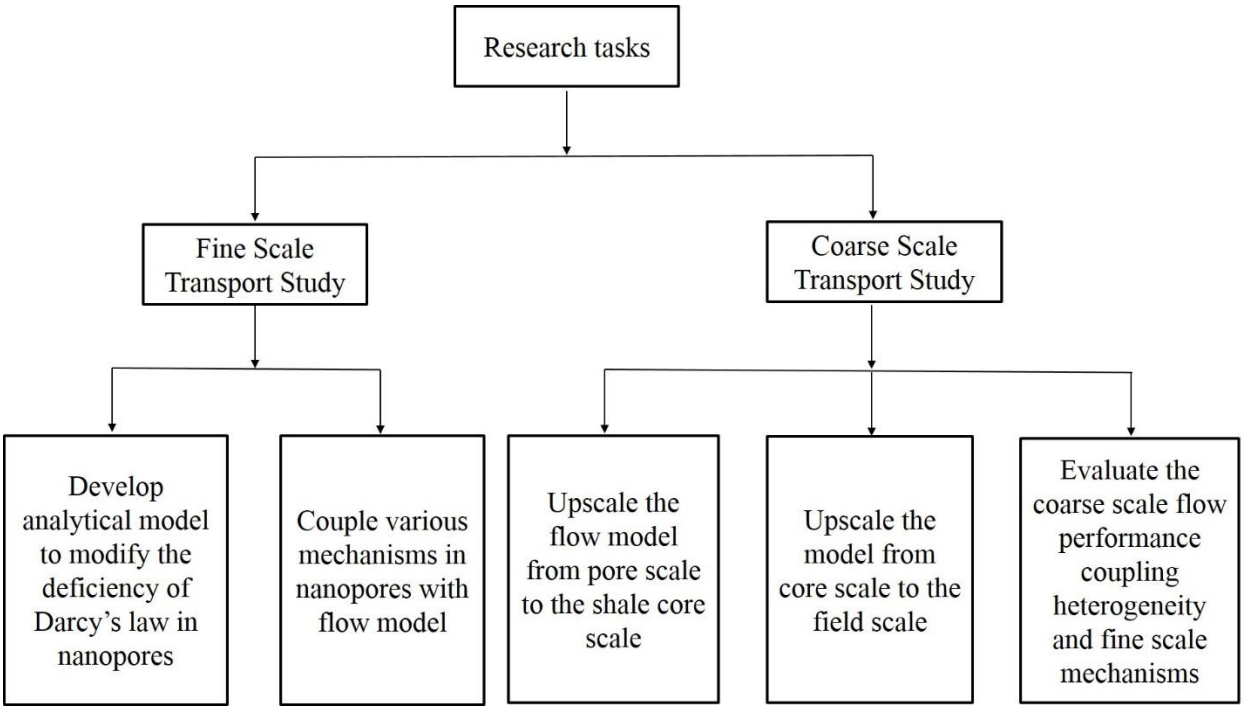

Figure 1.2: Research tasks of the dissertation.

CHAPTER 2: LITERATURE REVIEW

2.1 Shale Gas

2.1.1 Shale Gas Evolution

Shale is a fine grained, dark colored, and clastic sedimentary rock which is a mix of organic matter (e.g., kerogen), consolidated clay minerals (clay, silica), and tiny interbedded minerals (e.g., feldspar and pyrite). During the deposition of fine-grained sediments, organic matter accumulates in the form of algae, plankton, and animal derived organic debris which are from nearby land areas and the water column (Könitzer et al., 2014). The gas and oil are gradually generated from these organic matter accumulations via a series of chemical reactions at high temperatures and pressures in the deep burial. It is indicated that the temperature window for the hydrocarbon conversion is between 60°C and 120°C, with gas and oil being formed at the upper and lower limit of this range, respectively (Ambrose et al., 2012). Moreover, tight nature of the matrix and the ability to retain the gas make these environments important gas trapping and storage locations. Hence, the organic-rich shale formations are typically regarded as both source and sealing cap rocks.

2.1.2 Shale Gas Exploitation

In general, the extracted shale gas is dry gas primarily composed of methane (> 90% mole fraction) (Javadpour et al., 2007). The shale gas resources are significantly abundant worldwide that are estimated to be 22,470 trillion cubic feet (Wu et al., 2016). According to EIA, the United States and Canada are the only major producers of commercially viable shale gas while China claims to be the largest holder of shale gas reserves. The boom of shale gas production arises from the buoyant gas market and the rapid technology advances including the hydraulic fracturing and horizontal drilling. The mineral materials that make up the bulk of shale are very fine with the

result that gas cannot readily move within the rock. Thus, the artificial hydraulic fracturing with over-pressured fluids and proppants are usually used to induce the open fracture network around the borehole and bridge the natural fractures in matrices to stimulate flow of the trapped gas by increasing permeability (Bousige et al., 2016). It is approximately estimated that 90% of drilled gas wells in the United States are fractured every year (Prud'homme, 2014).

2.1.3 Primary Shale Plays in the States

The Barnett shale in North Texas is the first shale play for the industrial exploitations, which is regarded as the most productive source of shale gas in the U.S. from 2002 to 2010 (EIA, 2013). Then, the success in the Barnett shale boosted the commercial developments in other explored shale plays such as Eagle Ford shale, Haynesville shale, and Marcellus shale (Wang et al., 2014). The Eagle Ford shale in Texas spreads over the area of 20,000 square miles and an average thickness of 250 feet. Another main play in Texas, Haynesville shale, extends from East Texas to West Louisiana covering the area of about 9,000 square miles and an average thickness of about 200 to 300 feet (Stephenson, 2016). However, the deep formation depth (i.e., 10,500 to 13,000 feet below the surface) in Haynesville shale lead to expensive drilling costs which hindered the profitable development as the gas prices dropped in recent years. Thus, Eagle Ford shale became the more profitable target for companies instead of Haynesville shale after the year of 2012 (Stephenson, 2016). The Marcellus shale trends across the significantly large area from Northeast New York to Southwest Pennsylvania covering 104,000 square miles and the thickness of more than 50 feet, which makes it the largest potential shale region in the States (Darrah et al., 2014). The primary shale plays in U.S. are illustrated in Figure 2.1.

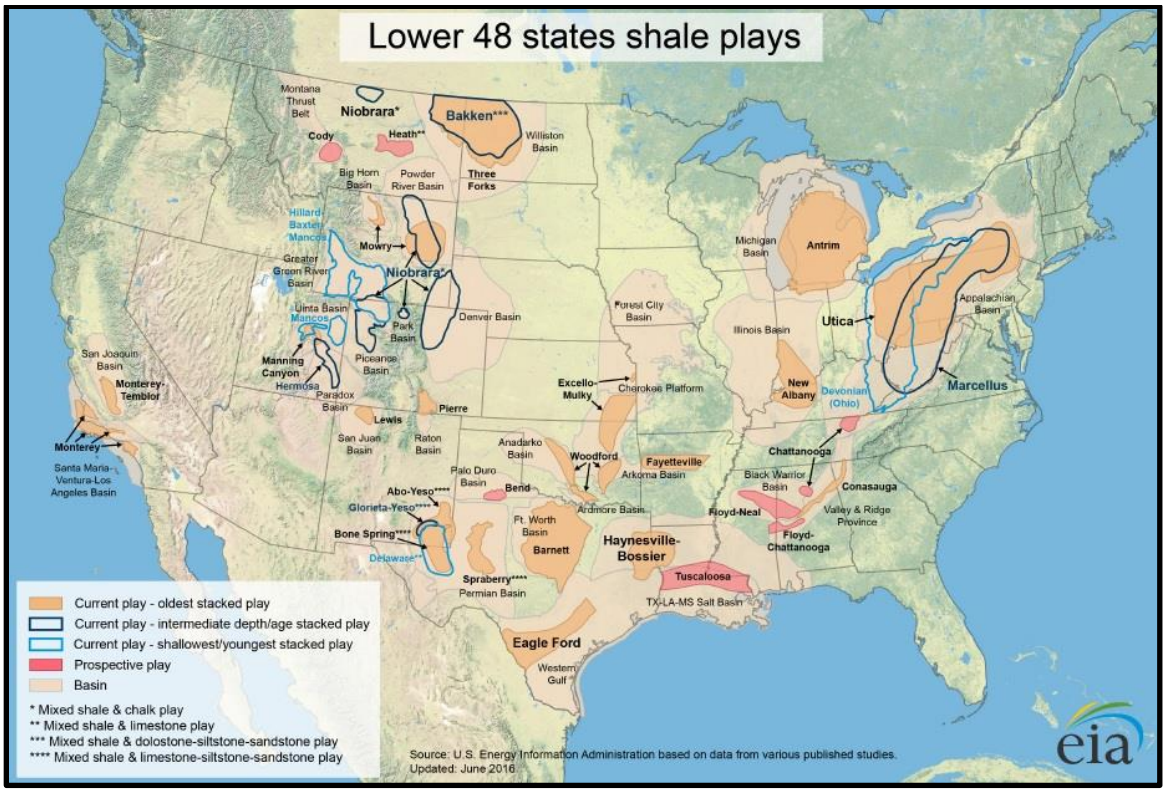

Figure 2.1: Distribution of shale gas plays in U.S. lower 48 states (EIA, 2016).

2.2 Shale Reservoir Characteristics

2.2.1 Shale Pore and Pore-Throat Size

The pore types in shale matrix can be roughly categorized as nanopores (diameter < 0.75 μm) and micropores (diameter ≥ 0.75 μm) in term of pore sizes (Loucks et al., 2009). And the nanopore is the predominantly abundant pore type. Moreover, the nanopore can be further subdivided into interparticle inorganic pores, intraparticle inorganic pores, and intraparticle organic pores. More specifically, the interparticle pores are found between inorganic particles and crystals whereas intraparticle pores are formed within inorganic particles or the organic matter (Loucks et al., 2012; Sondergeld et al., 2010). Slatt and Brien (2011) have found the dominant presence of intraparticle organic nanopores in organic-rich shales. In addition, shale gas is mostly stored in the intraparticle nanopores of the inter-connected network or bedding-parallel laminae in organic matter. In

contrast, the scattered presence of inorganic pores contributes much less to the gas transport in shale matrix.

The size of organic pore and pore-throat significantly controls the gas storage and transport capacity through the shale matrix, respectively. Typically, the organic pore size is less than 1,000 nm (Milliken et al., 2013). It is discovered that average pore size in Barnett shale ranges from 20 to 185 nm (Loucks et al., 2009). Curtis (2002) found a large amount of nanopores with size from 2 to 100 nm. In contrast, the size of organic pore-throat is commonly smaller than 20 nm. Nelson (2009) found that the pore-throat size ranges from 9 to 45 nm and 20 to 160 nm in the basin of Pliocene Beaufort-Mackenzie and Pennsylvanian Anadarko, respectively. In addition, the morphology of shale pores is in presence with sphere, parallel plates, elliptical, irregular polygons or combinations of above geometries. In contrast, the pore throat shows up with straight capillary or smoothly curving geometry (Loucks et al., 2012).

2.2.2 Shale Porosity and Tortuosity

The porosity in shale matrix is very low which is commonly smaller than 10% (Milliken et al., 2013). Chalmers et al. (2012) have claimed that shale porosity ranges from 2.5% to 6.6% via helium porosimetry experiment. Moncrieff (2009) pointed out the average porosity of Barnett shale could be as low as 2.0%. Chen et al. (2013) showed the total porosity of samples in Lower Silurian Longmaxi gas shale is between 2.05% and 5.87% with an average value of 4.04%. In addition, the porosity can be influenced by the fractions of mineral composition (i.e., organic matter, clay content, quartz content, and carbonate content). Wang et al. (2019) have indicated that the amount of total organic carbon (TOC) presents a positive relationship with porosity due to the

contributions of organic pores. Given that clay content increases with TOC content, clay content shows a positive correlation with porosity as well. Meanwhile, the porosity has the negative correlation with the quartz and carbonate content due to the dilution effect on TOC content.

The tortuosity in the shale is typically large and it increases with the TOC. It is reported that the average tortuosity is 2.5 in the shale with amount of organic matter as low as 0.1%-0.8%. However, the average tortuosity goes up to 8.5 as the TOC content reaches 2.2%-2.5% (Thomas and Clouse, 1990). Moreover, it is found that the tortuosity is direction-dependent due to the shale anisotropy. Revil et al. (2013) indicated that the transverse tortuosity could be almost one order of magnitude greater than the in-plane tortuosity. Based on the random walk method, Chen et al. (2015) found the calculated tortuosity values in the horizontal and vertical directions showed significant differences in the range of 1.26 to 2.99 and 3.27 to 7.6, respectively. However, it is difficult to attain the true tortuosity for the shale formation since it requires accurate numerical simulations on the high-resolution images of shale to predict the values of tortuosity (Srisutthiyakorn and Mavko, 2017).

2.2.3 Intrinsic Permeability

During the long geological period, shales are deposited as muds in low-energy environments such as tidal flats and deep-water basins where the fine-grained clay particles fall out of suspension in the quiet waters. Hence, the laminated layers of sediment result in the tight formation with extremely low permeability horizontally and vertically. Such low intrinsic permeability indicates that the stored gas in shale cannot quickly move unless the high-conductance channels like fractures are induced. In general, the intrinsic permeability in shale matrix falls in nano-Darcy

scale. Javadpour et al. (2007) measured permeability of 152 samples from 9 gas reservoirs and found that the permeability in 90% of samples were less than 150 nD. Besides, the intrinsic permeability in shale is more sensitive to the stress effect in comparison with those in conventional sandstone formations. Bowker (2007) found that the permeability under significant stress effect can be two orders of magnitude higher than the original one. Furthermore, it is reported that no clear correlations exist between the mineral contents and the intrinsic permeability (Wang et al., 2019). In addition, shale permeability exhibited the positive relationship with porosity if a large fraction of organic nanopores existed. This is because the pore network in mature organic matter provides better connectivity than the intraparticle and interparticle pores (Guidry et al., 1995).

2.2.4 Specific Surface Area and Wettability

The abundance of nanopores in organic matter results in the large specific surface area in shale porous medium. With the development of shale thermal maturity, the specific surface area continues to grow with the increase of organic nanopores. Meanwhile, much gases adsorb to the surface of nanopores, which might account for 20% to 85% of total amount of shale gas in nanopores (Bowker, 2007). It is reported that the specific surface area in North America shales ranges from 2.0 to 103.7 m^2/g (Clarkson et al., 2013). The plentiful organic matters in shale inevitably have an impact on the wettability. It is discovered that nanopores in the organic matter are prone to the oil wettability while inorganic pores in shale matrix commonly show the water or mixed wettability (Sondergeld et al., 2010; Passey et al., 2010).

2.3 Transport Mechanisms in Nanopores

Shale gas in nanopores are in the presence of two different states: 1) free gas in organic/inorganic nanopores; 2) adsorbed gas on the pore surface. The differences in the presence of states have resulted in the distinct transport mechanisms. The free gas transport cannot be characterized by the N-S equations due to the rarefaction effect. According to Gad-el-Hak's studies (1999), the characterization can be carried out by the numerical methods and analytical models. Aside from probing the nature of rarefaction in nanopores, a variety of experimentally confirmed mechanisms in shale formations have significantly influenced the gas transport. Hence, the analytical methods have been modified to incorporate multiple physical mechanisms which are commonly observed under reservoir conditions such as the real gas effect, adsorption (Jia et al., 2018a), surface diffusion (Michel et al., 2011; Riewchotisakul and Akkutlu, 2016), and confinement effect (Song et al., 2016; Yang et al., 2019a).

2.3.1 Rarefaction in Nanopores

Navier-Stokes (N-S) equations are the classic governing equations for the bulk gas transport in which the slip and temperature-jump boundary conditions are not defined. According to the continuum hypothesis, the macroscopic properties characterized in N-S equations such as density, velocity, stress and heat flux can be defined by the average local properties of microscopic molecules. Moreover, when the mean free path (i.e., average distance traveled by a molecule before collisions) is far less than the characteristic length of transport medium, the inter-molecule collision frequency is far more than molecule-wall collision frequency. In this case, macroscopic properties are capable to reach the thermodynamic equilibrium where the stress is linearly related to the strain gradient (Newtonian fluids) and the heat flux is linearly correlated with the

temperature gradient (Fourier fluids). However, as the characteristic dimension of transport medium is comparable with the gas mean free path, the flow dynamics exhibits the rarefied phenomena. The rarefaction indicates that the mean free path of the gas molecules is not a small magnitude compared with the characteristic length of the flow medium and the molecule-wall collisions become intensified when the density reaches a low level (Mason et al., 1967). Javadpour et al. (2007) have affirmed that shale formations are featured with a large amount of nano-pores where the gas transport presents the distinct rarefaction effect under thermo-equilibrium conditions (e.g., pressure of 3.0-70.0 MPa and temperature of 322-403 K). The rarefaction leads to the observed gas slippage on the pore surface. Moreover, the Newtonian linear viscosity correlation becomes inaccurate with the increase of rarefaction degree (Karniadakis et al., 2005). Due to the intensive density oscillation near the fluid-solid interface, the conventional continuum gas transport theories such as Darcy's equation, Hagen-Poiseuille equation, and Navier-Stokes equations cannot be directly applied to the nano-scale gas flow.

2.3.2 Knudsen Number

To quantify the degree of rarefaction effect (i.e., non-continuum) in nanopores, Knudsen number (Kn) which is defined as the ratio of the molecular mean free path (λ) to the characteristic length (e.g., pore radius, r) is typically adopted (Bird, 1994). From the expression, it is known that Knudsen number increases with the decrease of characteristic length or the increase of mean free path. Based on the Knudsen number, Roy et al. (2003) classified the rarefied gas flow into four realms: continuum flow regime ($Kn \leq 0.001$), slip flow regime ($0.001 < Kn \leq 0.1$), transition flow regime ($0.1 < Kn \leq 10$), and Knudsen diffusion regime ($Kn > 10$). Also, it is indicated that shale gas flow behaviors typically range from slip to Knudsen diffusion flow regimes (Wu et al., 2016). In

the slip flow regime, collisions between molecules and the wall cannot be ignored. The failure of the continuum hypothesis results in the fact that shear stress in the continuum equations of mass and momentum conservations cannot be characterized by the macroscopic magnitudes of lower order (i.e., velocity) (Shen et al., 2005), thus non-Darcy flow behaviors manifest themselves mainly at the vicinities of the boundaries (i.e., velocity slippage). Meanwhile, the analytical equations based on Navier-Stokes are still valid, but it is imperative to modify the boundary conditions (Civan, 2010). In the Knudsen diffusion regime, the gas is so rarefied that collisions of molecules with the pore wall prevail, and the velocity distribution becomes the equilibrium Maxwell distribution. In the transition flow regime, it is difficult to analyze the flow patterns since the molecule collisions between the wall and mutual collisions both have significant impacts, and the conventional Navier-Stokes equations break down (Chai et al., 2019a). Numerous attempts have been made to derive representative analytical equations to characterize the rarefaction in this flow regime (Javadpour, 2009; Civan, 2010; Sakhaee-Pour and Bryant, 2012; Riewchotisakul and Akkutlu, 2016; Jia et al., 2018b). The classification based on Knudsen number together with the corresponding governing equations have been illustrated in Figure 2.2. Such a classification mainly serves as a frame of reference and the critical Knudsen numbers for each regime are empirical in nature. That is because the value of characteristic length cannot be accurately determined.

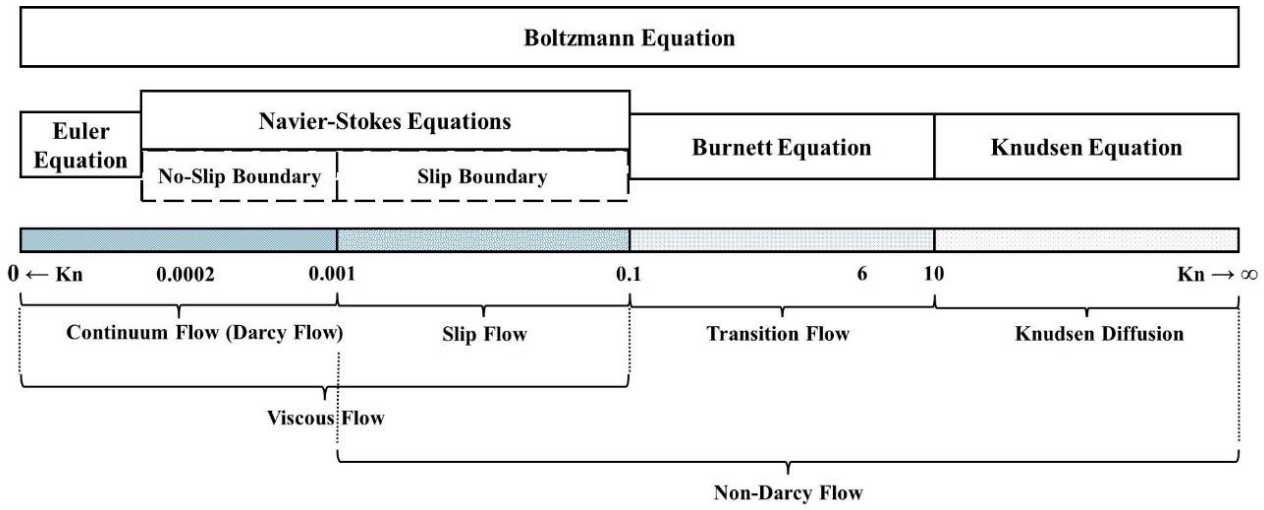

Figure 2.2: Flow regime classifications and corresponding governing equations.

2.3.3 Numerical Methods for Free Gas Transport

Numerical methods can be basically distinguished as the direct numerical solution of the Boltzmann equation (BE) and the microscopic particle-based simulation. Despite the fact BE is the basic equation of molecular gas dynamics, it is almost impossible to determine the exact solution of BE due to its complicated collision integral term and integro-differential mathematical expression. To overcome this difficulty, a variety of approaches aim to approximate BE and directly accomplish the numerical solution in the limit of errors. Nordsieck and Hicks (1967) used the Monte Carlo method of quadrature to evaluate the collision integral and finite difference method to calculate the BE. Loyalka and Hamoodi (1990) linearized the BE by simplifying the collision integral to obtain the numerical solution in late slip and transition flow regimes. However, there have been suspicions concerning the application of direct numerical solution over entire flow regimes owing to the complexity of BE and the instability problem related to the numerical scheme (Shen, 2005).

The microscopic particle-based simulation recognizes the gas as a swarm of discrete particles of which the position and momentum are calculated either deterministically or probabilistically (Javadpour, 2009). Currently, widely accepted methods include molecular dynamics simulation (MD), direct simulation Monte Carlo (DSMC), and Lattice Boltzmann simulation (LBM). The molecular dynamics (MD) method considers deterministic kinetics of each molecule based on Newton's laws of motion, thereby attains the highest accuracy compared with other methods (Binder, 2004; Kazemi and Takbiri-Borujeni, 2016). The DSMC is a probabilistic particle simulation based on kinetic theory in contrast to the deterministic MD method, and DSMC is typically applied for the high-*Kn* flow in transition flow regime (Christou and Dadzie, 2015). Unfortunately, both MD and DSMC have extremely slow convergence rates and requires prohibitively expensive computational resources, which are not practical in the simulation of large-scale and complex spatial-temporal system (Oran et al., 1998). Compared with MD and DSMC, LBM is the most efficient and practical approach for shale gas flow simulation where particles representing packets of gases are tracked through the computational domain of grids. Moreover, the method is relatively easy to code and ideally suited for parallel computing platforms. The primary drawback is that the conventional LBM method can only cover the continuum and slip flow regimes because the governing equation is based on Navier-Stokes equation which is invalid for the high-*Kn* number flow in transition and Knudsen diffusion flow regimes (Chen and Doolen, 1998).

2.3.4 Analytical Modeling for Free Gas Transport

Analytical methods characterize the rarefied gas flow from the perspective of continuum hypothesis (i.e., reduced Navier-Stokes equations), which shows advantages over numerical

approaches in terms of computation efficiency and practicality at various scales (Roy et al., 2003). Different analytical models have been developed in the scientific community of rarefied gas dynamics to interpret counter-intuitive phenomena in micro-capillaries such as the slippage effect near the wall and nonlinear pressure distribution. On the grounds that the rarefaction effect exists in nanopores, a variety of models from rarefied gas community are either directly used or modified to explain the shale gas flow behavior in the natural gas engineering community. Representative analytical models in both communities have been summarized and categorized into three classes based on theoretical hypotheses as shown in Table 2.1. It is seen that theoretical hypotheses for three classes are listed in the first column. Accordingly, analytical models in the second column are originally derived to characterize the rarefied gas flow in mechanical and chemical engineering. Such models are adopted and modified as listed in the third column to represent the shale gas flow. Note that the collected models are only applicable for the cylindrical nanocapillary.

Table 2.1: Summary of representative analytical models

	Mathematical Expressions	*Formulae Developed in Mechanical/Chemical Engineering* **Rarefied Gas in Micro-Capillary/Channel**	*Formulae Applied in Natural Gas Engineering* **Gas Flow in Tight Sandstone/Shale Cores**
First Class	Continuum Flow and Slip Boundary	Cercignani (1964) Sreekanth (1969) Arkilic et al. (1997) Beskok and Karniadakis (1999) Hadjiconstantinou (2003) Maurer et al. (2003) Ewart et al. (2007) Yamaguchi et al. (2011)	Klinkenberg (1941) Jones and Owens (1980) Sampath and Keighin (1982) Florence et al. (2007) Civan (2010) Sakhaee-Pour and Bryant (2012) Fathi et al. (2009) Okamoto et al. (2017)
Second Class	Weighted Continuum Flow and Fickian Diffusion	Adzumi (1937) Mason et al. (1967) (DGM) Ertekin et al. (1986) Veltzke and Thöming (2012)	Michel et al. (2011) Swami and Settari (2012) Singh et al. (2014) Wasaki and Akkutlu (2015)
Third Class	Weighted Viscous Flow and Knudsen Diffusion	Brown et al. (1946) Scott and Dullien (1962)	Javadpour (2009) Darabi et al. (2012) Rahmanian et al. (2013) Wu et al. (2015)

(1) The First Class

The first class of analytical models defines the rarefaction via the slip theory which extends the Hagen-Poiseuille equation (i.e., solution of reduced N-S equation for capillary) by assuming a non-zero tangential slip velocity (u_s) on the wall. The velocity profiles of Hagen-Poiseuille flow (i.e., blue curve) and slip flow (i.e., green curve) are shown in Figure 2.3. Since Navier-Stokes (N-S) equations break down beyond the continuum flow regime, the no-slip boundary is typically replaced by the slip boundary (i.e., Maxwell's slip boundary condition) as follows (details can be seen in Appendix A).

$$u_s = C_1 Kn\left(\frac{\partial u}{\partial n}\right)_s + C_2 Kn^2\left(\frac{\partial^2 u}{\partial n^2}\right)_s \tag{2.1}$$

where u_s is slip velocity, *Kn* is Knudsen number, C_1 and C_2 are slip coefficients for the first and second order terms, respectively. $(\partial u/\partial n)_s$ and $\left(\partial^2 u/\partial n^2\right)_s$ denote the first and second derivative of tangential velocity with respect to normal direction of control surface, respectively. Note that when C_2 is equal to zero, Eq. 2.1 reduces to the first-order Maxwell slip model which has been widely used to characterize gas slippage in tight cores (Klinkenberg, 1941; Jones and Owens, 1980; Sampath and Keighin, 1982; Florence et al., 2007).

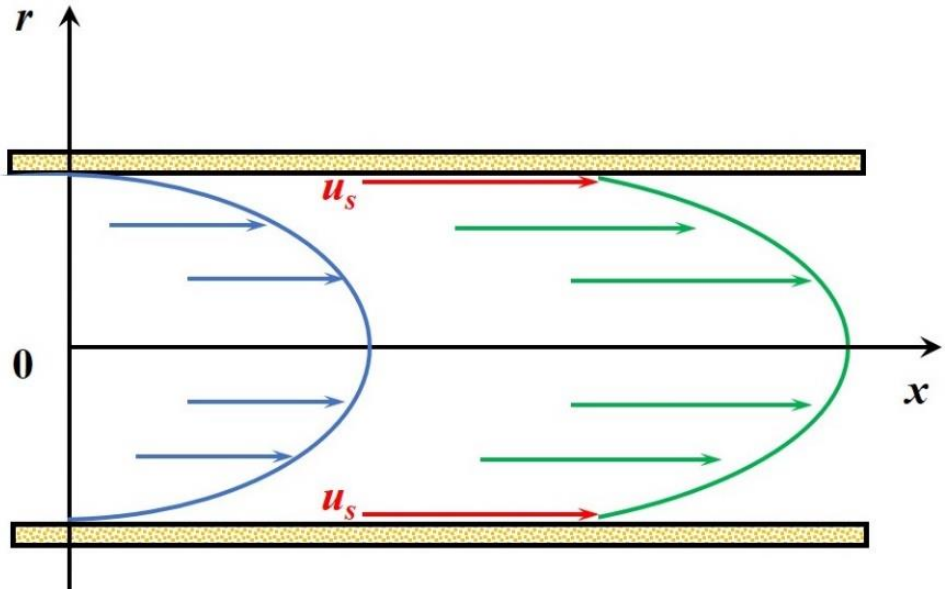

Figure 2.3: Velocity profile of continuum flow and slip flow in the nanocapillary.

Klinkenberg (1941) discovered the presence of rarefaction effect may account for the unexpected higher permeability in tight cores and proposed the well-known Klinkenberg's effect to elaborate the gas slippage near the pore wall. Klinkenberg correction for slippage is an empirical model and does not take Knudsen diffusion into account. Arkilic et al. (1997) noticed that the measured mass flow is higher than predicted by the continuum model and adopted the first-order Maxwell slip model to fit the data. However, Beskok and Karniadakis (1999) have pointed out that the first-

order Maxwell model is insufficient to represent the velocity profile beyond the slip flow regime. In contrast, the second-order velocity model is competent to cover full flow regimes, and various empirical slip coefficients have been suggested in the work of first classes of models (Cercignani, 1964; Sreekanth, 1969; Maurer et al., 2003; Florence et al., 2007; Ewart et al., 2007; Yamaguchi et al., 2011; Sakhaee-Pour and Bryant, 2012). Given Eq. 2.1, a closed form solution for gas flow velocity in the capillary can be obtained by solving Eqs. 2.2 and 2.3 as follows.

$$\frac{1}{r}\frac{d}{dr}\left(r\frac{du}{dr}\right)=\frac{1}{\mu}\frac{dP}{dx} \tag{2.2}$$

$$S.T.\ \frac{du}{dr}|_{r=0}=0\ ;\ u|_{r=r_o}=u_s \tag{2.3}$$

where r is arbitrary radius, du/dr is tangential velocity gradient with respect to radial axis, μ is gas viscosity at standard condition, dP/dx is pressure gradient with respect to longitudinal axis, r_o is capillary radius. Therefore, the total mass flux of gas flow, F_t, can be derived by the integration with respect to radius,

$$F_t=\frac{\bar{P}M}{\pi r_o^2 RT}\int_0^{r_o} u\cdot 2\pi r dr \tag{2.4}$$

where R is universal gas constant, T is temperature, $\bar{P}$ is capillary average pressure, M is molar mass. However, it is indicated the predicted fluxes based on the second-order model deviate from experimental data despite the consistency with velocity profile on entire flow regimes. Based on large volume of industrial data, Florence et al. (2007) defined a pseudo Knudsen number and modified the model proposed by Beskok and Karniadakis, which was applicable to ultra-tight porous media. Civan (2010) proposed a simple inverse power-law relationship of rarefaction factor via the regression with experiment data. However, the model is not applicable in the late transition and Knudsen diffusion flow regimes.

The disadvantages of the first class of models are twofold: 1) it is demonstrated that Knudsen diffusion in free molecular flow regime cannot be neglected in nanopores under reservoir conditions (Darabi et al., 2012; Singh et al., 2014; Wu et al., 2015). Nonetheless, the slip theory inherently ignores Knudsen diffusion in its formulation because the streamwise velocity in slip theory follows first-order $\boldsymbol{O}(Kn)$ or second-order correction $\boldsymbol{O}(Kn^2)$ while the Knudsen diffusion asymptotes to the order of $\boldsymbol{O}(lnKn)$ as *Kn* approaches infinity (Cercignani, 1963); 2) two unknown slip coefficients in the slip velocity model need to be determined by experiments, which increases the uncertainty for applications.

(2) The Second Class

The second class of analytical models characterize the rarefaction by advection-diffusion model (ADM) where the flux is expressed via linear summation of the Hagen-Poiseuille equation and Fickian diffusion equation. The intermolecular and molecule-wall interactions are characterized as the continuum flow and Fickian diffusion, respectively. It is contended that the slippage near the wall results from the diffusion according to Fick's first law, and the total mass flux, F_t, can be written as

$$F_t = w_c F_c + w_f F_f \tag{2.5}$$

where w_c and w_f are weights for continuum flow and Fickian diffusion, respectively. F_c is mass flux of continuum flow which is expressed by Hagen-Poiseuille equation as follows.

$$F_c = -\frac{r_o^2}{8}\frac{\overline{P}M}{\mu RT}\nabla P \tag{2.6}$$

where ∇P is pressure gradient. F_f is mass flux of Fickian diffusion which is given as (Wang et al., 2019)

$$F_f = -\frac{D_f M}{RT}\nabla P \tag{2.7}$$

where D_f is Fickian diffusion coefficient. Since Knudsen diffusion is the dominant diffusive mechanism in nanocapillary, Fickian diffusion coefficient, D_f, can be defined as Knudsen diffusion coefficient which is expressed as $D_k = \left(2r_o/3\right)\sqrt{\left(8RT\right)/\left(\pi M\right)}$. Then, Eq. 2.7 reduces to the Knudsen equation as follows (Adzumi, 1937; Mason et al., 1967; Ertekin et al., 1986).

$$F_k = -\frac{D_k M}{RT}\nabla P = -\frac{2r_o}{3}\sqrt{\frac{8M}{\pi RT}}\nabla P \tag{2.8}$$

In addition, different constant weights have been recommended to fit the experiment data (Michel et al., 2011; Veltzke and Thöming, 2012; Singh et al., 2014).

The disadvantages of the second class of models are twofold: 1) Kazemi and Takbiri-Borujeni (2015) have emphasized the importance of slip flow mechanism under reservoir conditions. However, the ADM model is in nature formulated based on the first-order Maxwell velocity which may generate large deviations of fluxes in late slip and transition flow regime (details can be seen in Appendix B); 2) the constant weight assignment is not flexible to provide a smooth transition from continuum to free molecular flow regime as the rarefaction increases. The weight coefficients for representative equations in the second class over entire flow regimes are presented in Figure 2.4. Particularly, subplots (*a*), (*b*), and (*c*) show the continuum flow weight and Fickian diffusion weight versus Knudsen number. It is seen that the characteristics for the second class is the constant weight assignment which is physically invalid in specific flow regimes. For instance, the

continuum weight is one in free molecular flow regime indicating that the continuum flow still exists in this regime.

(3) The Third Class

Despite of various expressions for flow regimes, the implicit dependency on Knudsen number exists across each flow regime. Numerous efforts have been made derive a generalized model which is capable to include all the flow regimes. Nevertheless, the universal governing equation is yet established due to the significant inconsistency among current models and the scarcity of solid experimental data. The third class of analytical models quantify the rarefaction effect based on the weighted superposition coupling viscous flow and Knudsen diffusion. It is noted that viscous flow includes continuum and slip flow, and it can be expressed by Eqs. 2.1-2.4. Hence, these models incorporate the merits from the first and second class of models which are capable to accurately capture the flow behavior in full flow regimes. The total mass flux, F_t, is given as

$$F_t = w_v F_c + w_k F_k \tag{2.9}$$

where w_v and w_k is weight for viscous flow and Knudsen diffusion, respectively. Note that the slip velocity is coupled to the weight of viscous flow (i.e., w_v) as opposed to the weight of continuum flow (i.e., w_c). Moreover, various weights are proposed to adjust the contributions of viscous flow and Knudsen diffusion to match the flow pattern in each flow regime (Brown et al., 1946; Scott and Dullien, 1962; Javadpour, 2009; Wu et al., 2015). Javadpour (2009) proposed a concise formulation which unites the viscous flow and Knudsen diffusion with weight of one. Liu et al. (2002) used defined the weight of Knudsen diffusion term as the proportion of slip area over pore cross-section area. However, the weight becomes negative which is physically invalid in the late transition and Knudsen diffusion flow regimes.

The disadvantage of the third class of models is that most weight coefficients are not physically reasonable. The weight coefficients for representative equations in the third class in full flow regimes are presented in Figure 2.4 as well. Specifically, subplots (*d*), (*e*), and (*f*) illustrate the viscous flow weight and Knudsen diffusion weight versus Knudsen number. It is noticed that the characteristics for the third class is the parameterized weight coefficients with Knudsen number. Such treatments enhance the suitability of analytical equations as the Knudsen number varies with the rarefaction effect. However, it is observed that the weights in (*d*) and (*e*) are not fully sensible across different flow regimes. For instance, Javadpour's model assigned the weight of Knudsen diffusion as value one (i.e., $w_k = 1$), thus the model cannot reduce to the slip flow and Knudsen diffusion equation in corresponding flow regimes as the *Kn* number changes; the viscous flow weight in the model of Rahmanian et al. (2013) becomes negative in the Knudsen diffusion flow regime; the weights in the model of Wu et al. (2015) are physically plausible since each weight can be adjusted with Knudsen number so that the model can reduce to Darcy equation or Knudsen equation in corresponding flow regimes.

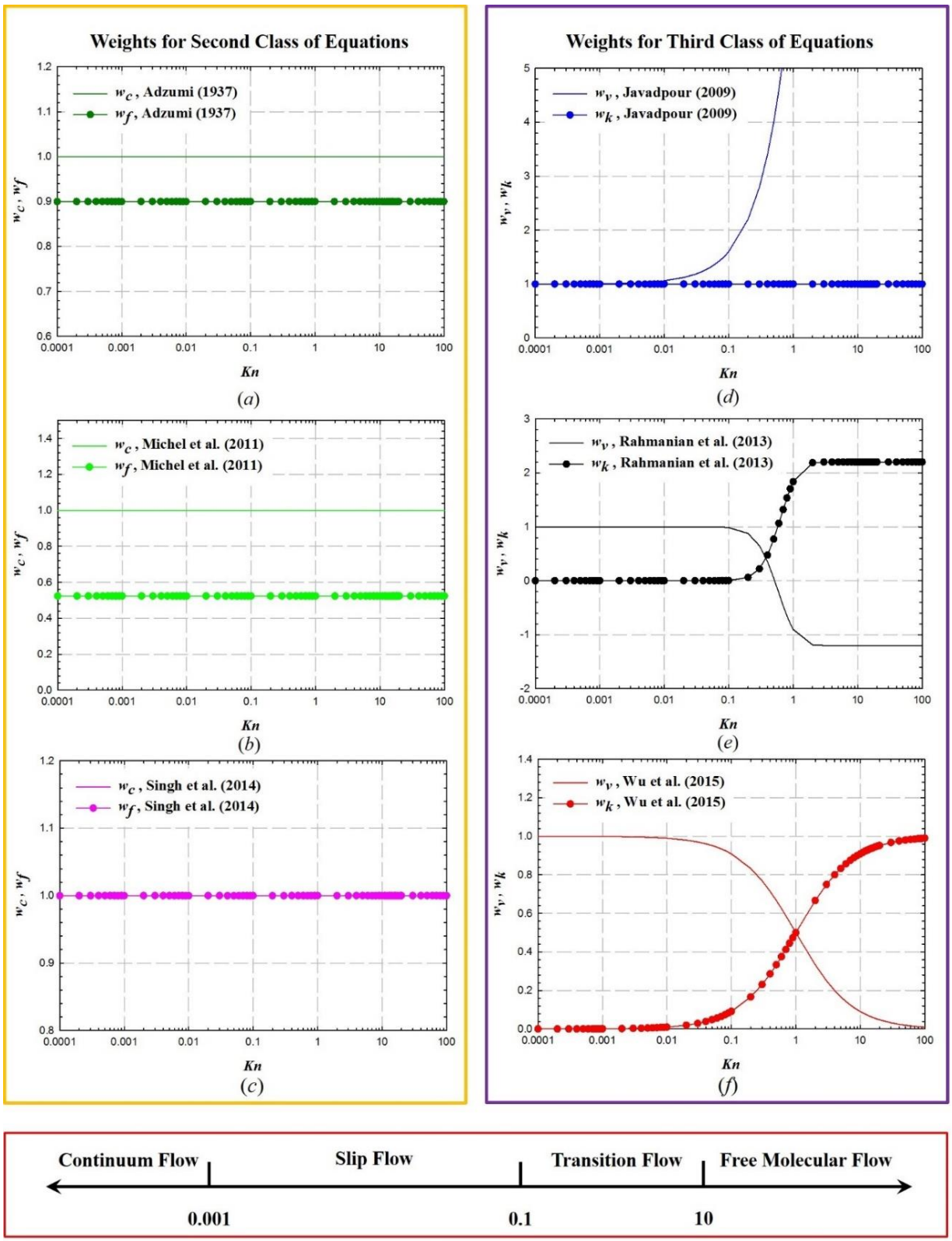

Figure 2.4: Weights versus Knudsen number for full flow regimes. Subplots (*a*), (*b*), and (*c*) illustrate the continuum flow weights (w_c) and Fickian diffusion weights (w_f) of representative equations in the second class; subplots (*d*), (*e*), and (*f*) illustrate the viscous flow weights (w_v) and Knudsen diffusion weights (w_k) of representative equations in the third class.

2.3.5 Impact Factors of Gas Transport in Nanopores

(1) Real Gas Effect

The common burial depth in North America is around 500-3,000m and the formation pressure ranges from 5.0 to 30.0 MPa. Curtis (2002) has summarized geological parameters for five representative shale gas systems (i.e., Antrim, Ohio, New Albany, Barnett, and Lewis) in the U.S. with the pressure from 2.0 to 28.0 MPa and temperature from 298 to 366 K. It is found the shale gas behavior cannot be described sufficiently by the ideal gas law at such reservoir conditions. Since real gas molecules possess a finite volume and experience the intermolecular force (i.e., van der Waals force) mutually, the collisions between molecules turn to be non-elastic. And the gas apparent permeability could be greatly reduced due to the intensification of such property (Michel et al., 2011). Hence, it is essential to consider the molecular volume and attractions in real gas flow models (Al-Hussainy et al., 1966). Azom and Javadpour (2012) provided an analytical model considering real gas effect based on Javadpour's model and showed that real gas effect was controlled by the pressure, temperature, pore size and gas type. Swami et al. (2012) derived a new expression of mean free path to account for the real gas behavior. However, a systematic error was introduced because the mean molecular velocity was still derived based on the ideal gas law. Michel et al. (2011) investigated the real gas effect by modifying the mean free path but failed considering the real gas impact on viscosity. Ren et al. (2016) incorporated an empirical Z-factor correlation to characterize the real gas effect. Wu et al. (2017) adopted empirical equations of compressibility factor and viscosity to characterize the real gas effect. Nonetheless, the compressibility factor calculated from the empirical equation was always larger than unity which was against the reality. Overall, majority of existing models demonstrating the transport mechanisms in nano-scale gas reservoirs are insufficient to embody the real gas effect.

(2) Gas Adsorption

Gas transport in organic nanopores behaves differently from that in inorganic nanopores because the nanopores in organic-rich shale matrix are characterized with large specific surface area and strong sorption affinity. Lu et al. (1995) showed that adsorption phase can account for 61% after testing 24 Devonian Shale samples. A significant amount of methane adsorption on the pore-wall can decrease the nominal pore size and make additional influences on the free gas flow (Santos and Akkutlu, 2013; Jia et al., 2018b). The adsorption of shale gas is mainly a reversible physical process, and the force between molecules and the wall is Van Der Waals force. Since the entire process is under the supercritical condition of methane, the significant capillary condensation is rarely discovered (Yu et al., 2016).

It is noticed that adsorption structure respectively characterized by Langmuir and BET isotherms may impose distinct influences on the apparent permeability (Chai et al., 2019b). It has been reported that adsorbed methane in various shales (e.g., Marcellus Shale) are prone to form multilayer adsorption at high pressures (Yu et al., 2016). Molecular dynamics simulation results have also demonstrated that the oscillation of gas density near the wall is caused by multilayer adsorption (Didar and Akkutlu, 2013; Riewchotisakul and Akkutlu, 2016). Hence, it is more reasonable to characterize methane adsorption in nanopores using the multilayer adsorption models such as BET isotherm model (Brunauer et al., 1938).

(3) Surface Diffusion

It also has been reported that molecules in the adsorbed layer can hop forward driven by the gradient of chemical potential along the pore wall. The movements of molecules induce the non-

negligible molar flux along the wall called surface diffusion (Fathi and Akkutlu, 2009). Studies have shown that the concentration gradient is the driven force of surface diffusion. In fact, the surface diffusion is an activation process in which the activated energy surpasses the bond strength (Yeh and Yang, 1989). It assumes that adsorbed molecule can jump over the energy barrier between two neighboring sites after adsorbing some energy, then the surface diffusion is activated (Chen and Yang, 1991).

Wu et al. (2016) have indicated such adsorbed-phase transport co-exists with free gas flow and cannot be ignored in organic nanopores. Due to the extremely small pore size, the free gas flow may be overwhelmed by the surface diffusion. Majumder et al. (2011) showed that surface diffusion flux can be 20 times larger than the free gas flux at low temperatures or pressures. Wu et al. (2017) pointed out surface diffusion can account for 92.95% of total flux in the nanopores (diameter < 2 nm). Various analytical models have been proposed to describe the surface diffusion. Hwang and Kammermeyer (1966) derived a model based on the hopping model of molecules at low pressures. Kapoor and Yang (1990) develop the model considering heterogeneous activation energy distribution on the surface. Wu et al. (2015) generalized the model of Hwang and Kammermeyer at low pressures incorporating the adsorption coverage, heterogeneous activation energy distribution on the surface, and isothermal adsorption. In addition, the surface diffusion coefficient is influenced by multiple factors such as temperature, pressure, and adsorption coverage. Arrhenius correlation quantitatively describes the temperature impact on the diffusion coefficient which increases with the temperature (Choi et al., 2001). Yang et al. (1973) showed surface diffusion coefficient increased with the pressure. Higashi et al. (1963) pointed out the diffusion coefficient increased with coverage in monolayer adsorption. However, most works have

modeled the methane adsorption/desorption process by use of Langmuir isotherm with an assumption of monolayer adsorption, which undermines the validity of the proposed surface diffusion models (Cui et al., 2009; Xiong et al., 2012; Wasaki and Akkutlu, 2015; Wu et al., 2016).

(4) Pore Confinement Effect

Another concern in nanopores is pore confinement effect which has been ignored in most of models. Once a fluid is subject to geometric constraints in a nanoscale, the molecule-molecule and the molecule-wall interactions can alter its thermodynamic properties such as Z-factor and critical properties (Singh et al., 2009). Based on the molecular dynamic simulations, Ingebrigtsen and Dyre (2014) demonstrated a large density oscillation for Lennard-Jones liquid near the slit pore walls. Miyahara and Gubbins (1997) showed that freezing point temperature was strongly affected by the strength of the attractive forces between fluid molecules and pore walls. Similarly, molecule-wall interaction in confined space is also the underlying mechanism of critical property shift of confined fluids (Gelb et al., 1999). Song et al. (2016) have considered the confinement effect into the gas transport model by introducing a critical-property correlation based on van der Waals EoS and a Z-factor correlation. Nonetheless, the introduced EOS and Z-factor are only valid for bulk fluid. In addition, the phase behaviors and kinetic behaviors of methane gas can be heavily influenced by the coupling effects from pore-confinement and real gas effect under reservoir conditions. Yang et al. (2019a; 2019b) have pointed out the deviation factor and gas critical properties are significantly different from that of bulk gas in conventional formations.

2.4 Multiscale Characterization of Transport Mechanisms

Numerous efforts have been made on the gas transport modeling in the single nano-capillary. However, gaining a holistic knowledge of the gas transport from the micro-scale pore level to macro-scale continuum level remains a difficult task and the fundamental understanding of flow behaviors across a hierarchy of scales and heterogeneity effect is necessary for the improved prediction of methane recovery and its management during the long-term shale gas development. The hierarchy of scales in the shale gas development has been shown in Figure 2.5. In the subplot (*a*), it shows the gas transport in the single nanopore where gas is generated in kerogen and then diffuses to the capillary to become free gas. Meanwhile, a large amount of gas molecules adsorb to the surface and contribute to the surface diffusion during pressure depletion. The subplot (*b*) illustrates that the nanopores form the inter-connected pore network in the mature organic matter whereas the subplot (*c*) presents the matrix block including the organic matter and inorganic matrix at the larger scale. In the subplot (*d*), it shows the schematic diagram of horizontal well with hydraulic fractures and the shale matrix composed of the matrix blocks in the subplot (*c*). The subplot (*e*) exhibits the slow transport in matrix blocks contributes to the long-tail production.

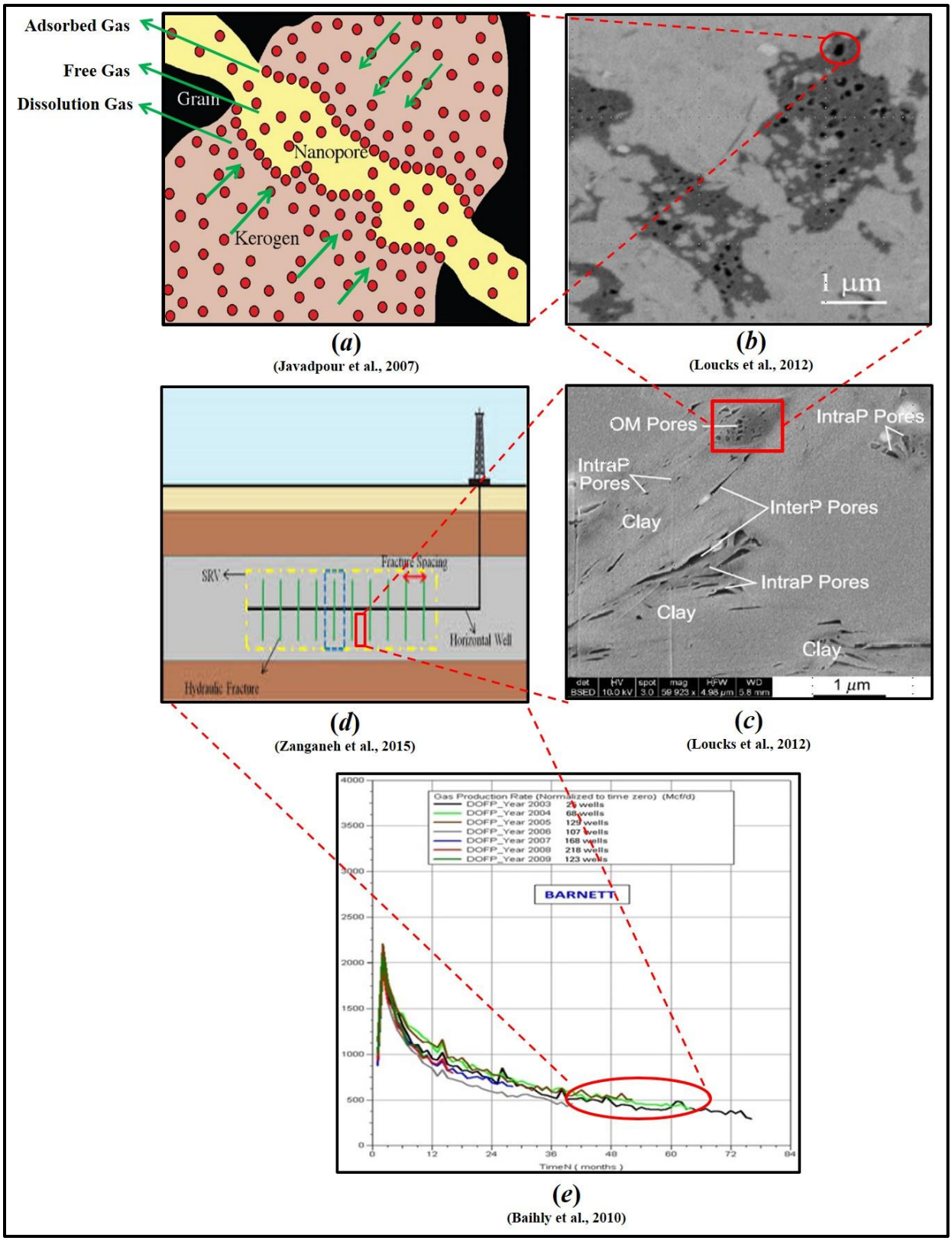

Figure 2.5: Schematic diagram of a hierarchy of scales during the shale gas development.

2.4.1 Upscaling Methods

The flow behavior at the coarse-scale continuum level (i.e., rock core and field) is significantly different from that pertaining to the fine-scale pore level. To elucidate flow performance differences across a hierarchy of scales, various upscaling techniques have been applied to bridge the gap. Some well-acknowledged upscaling approaches include the method of volume averaging (Whitaker, 1999), homogenization via multiple-scale expansions (Adler, 1992), and digital rock models based on imaging techniques (Dong and Blunt, 2009). To attain an averaged partial differential equation that characterizes the macroscopic behavior of the original equation is called homogenization. Tartakovsky (2000) derived the effective permeability based on stochastic averaging of nonlinear gas flow equations in heterogeneous porous media. Sahimi (2003) has adopted the upscaling technique of perturbation theory to statistically describe the effects of random heterogeneities in hydrology. The digital rock technique is the common approach for the multiscale characterization in shale matrix because they are capable to reveal useful information about the pore network and spatial connectivity. Specifically, a series of imaging experiments using Micro-Computed Tomography (Micro-CT), Scanning Electron Microscope (SEM), Focused Ion Beam Scanning Electron Microscope (FIB-SEM), or Helium Ion Microscopy (HIM) instruments can be implemented to collect the high-resolution pore-structure images. Such images enable to directly reconstruct the 3D digital model by using the pore segmentation and extraction (Silin and Patzek, 2006; Dong and Blunt, 2009) or using 2D images by means of stochastic methods such as the Markov Chain Monte Carlo (MCMC) method and the multiple-point statistics (MPS) method (Hazlett, 1997; Quiblier, 1984; Keehm et al., 2004; Wu et al., 2006; Tahmasebi et al., 2012). The re-constructed digital rock provides the platform for subsequent analytical and numerical analysis of shale gas transport coupling multi-physics in the heterogeneous matrix.

All upscaling methods require closure assumptions to decouple the average system behavior from the fine-scale information. On the other hand, existing methods have the limitations which include the loss of accuracy as the model scale becomes coarse (e.g., upscaling 1-D flow model to 2-D or 3-D model). For example, the digital rock technique is not applicable to large-scale simulation due to the computational capability (Chen et al., 2013). In addition, it is difficult to extract the interconnected pore-network for reconstruction because of the poor connectivity and the large range of pore size distribution (Mehmani et al., 2013). Inappropriate upscaling techniques may undermine the veracity of fine-scale simulations.

2.4.2 Heterogeneity Characterization

Nano-pore structure in ultra-tight shale formation is usually tortuous and irregular. Trying to capture the exact flow characteristics is impractical and daunting. Heterogeneity causes qualitative changes in behaviors of system, which requires accounting for the presence of percolation as well as the hierarchy of unit types at different scales. It is impossible and unnecessary to characterize the heterogeneity of shale matrix deterministically. Various theoretical approaches have been performed to quantify the heterogeneity impact via extracting the effective coefficient by homogenizing the heterogeneous shale matrix. Sahimi (2003) utilized the critical path analysis (CPA) to depict the flow in a highly heterogeneous porous medium and claimed the conductance was dominated by pore throats whose radii were slightly greater than a critical radius, which mapped the transport problem onto an equivalent percolation problem. Darabi et al. (2012) described the spatial heterogeneity of organic matter in the proposed conceptual matrix by the homogenization theory. Fathi and Akkutlu (2009) introduced the perturbation theory to the

governing diffusivity equation to characterize the weak heterogeneity induced by inherent porosity fluctuations in shale matrix. Ghanbarian and Javadpour (2017) applied the effective medium approximation (EMA) to smooth out the spatial heterogeneity with respect to the pore size distribution.

The heterogeneity characterized by aforementioned mathematical approaches cannot truly reflect the matrix heterogeneity due to the over-simplified physical model (e.g., periodic array of unit cells in shale matrix for homogenization analysis) and unavoidable theoretical assumptions (e.g., weak fluctuation assumption in perturbation theory application; narrow pore size distribution in EMA application). In addition, most of existing studies focusing on the shale heterogeneity influence have neglected the impact of multiple physical mechanisms under reservoir conditions (Fathi and Akkutlu, 2009; Akkutlu and Fathi, 2012; Akkutlu, et al., 2015).

2.5 Summary

Shale gas is natural gas which is generated and stored in the tight shale formations. In general, the predominant pore size and intrinsic permeability in the shale formation fall in the nanoscale and the trapped gases in intraparticle organic nanopores contribute most to the gas flow in matrix. Moreover, the porosity in shale matrix is very low which is commonly smaller than 10% while the tortuosity is typically large and it increases with the TOC. In addition, the large specific surface area of nanopores and oil wettability make substantial gas adsorb to the organic pore surface. The characterization of shale gas development involves the modeling from the micro-scale pore level to macro-scale continuum level. The gas transport at micro-scale pore level incorporates the modeling of free gas transport including the numerical and analytical methods. Meanwhile, the

model needs to consider the influence of multi-physics under reservoir condition such as real gas effect, gas adsorption, surface diffusion, and pore confinement effect. In contrast, the gas transport description at macro-scale continuum level should couple the flow behaviors in nanopores, organic matter, inorganic matrix, and the induced hydraulic fractures.

CHAPTER 3: A NEW UNIFIED GAS TRANSPORT MODEL FOR REAL GAS FLOW IN INORGANIC AND ORGANIC NANOPORES

3.1 Introduction

According to the analytical modeling analysis in the Literature Review 2.3.4, it shows that the mathematical expression based on the hypothesis of the third class (i.e., Eq. 2.9) would be appropriate to accurately characterize the shale gas flow in nanopores. To achieve this goal, it is important to assign the rational weights to viscous flow and Knudsen diffusion term in a way that they can be united in full flow spectrum.

Bravo (2007) firstly proposed a layer-sequence model that covered various flow regimes of ideal gas flow in nano-scale porous media. However, inappropriate assumptions in Bravo's model have weakened its accuracy to a certain degree. Bravo assumed that the nano-capillary could be partitioned into three zones, i.e., viscous flow in the central zone, transition flow in the middle annular zone, and Knudsen diffusion in the outer annular zone near the nano-capillary wall. In addition, the transition flow is considered to be independent of viscous flow and Knudsen diffusion mechanisms. Thus, three flow mechanisms are separately expressed in a piecewise formulation in terms of pressure and Knudsen number. Such an expression of transition flow is contradicted with other's work where the transition flow is dependent on both the viscous flow and the Knudsen diffusion (Javadpour, 2009; Veltzke and Thöming, 2012; Wu et al., 2016). Also, integrating the viscous flow, transition flow, and Knudsen diffusion in a piecewise manner significantly limits the flexibility and applicability of Bravo's model at a wide range of pressure conditions, e.g., unconventional reservoir conditions. Besides, four empirical parameters involved in the layer-sequence model simply intensify the uncertainties of Bravo's model and limit its application in

numerical simulations. Furthermore, the velocity profile in the central zone of Bravo's model only adopts the first-order correction, which has been demonstrated to be controversial (Beskok and Karniadakis, 1999).

A new unified gas transport model has been developed to characterize single-component real-gas flow in the homogeneous nano-scale organic and inorganic porous media by modifying Bravo's model. More specifically, a straight capillary tube is characterized by a conceptual layered model consisting of a viscous flow zone, a Knudsen diffusion zone, and a surface diffusion zone. To specify the contributions of the viscous flow and the Knudsen diffusion to the gas transport, the virtual boundary between the viscous flow and Knudsen diffusion zones is firstly determined based on an analytical molecular kinetics approach. As such, the new unified gas transport model is derived by integrating the weighted viscous flow and Knudsen diffusion, and coupling surface diffusion. The model is also comprehensively up-scaled to bundles-of-tubes model considering the roughness, rarefaction, and real gas effect. Nonlinear programming methods have been utilized to optimize the empirical parameters in the newly proposed gas transport model. Consequently, the newly proposed gas transport model yields the most accurate molar fluxes compared to Bravo's model and other four analytical models. One of the advantages of the new unified gas transport model is its great flexibility since the Knudsen number is included as an independent variable, which also endows the newly proposed model the capability to cover the full flow regimes. In addition, the apparent permeability has been mathematically derived from the new unified gas transport model. A series of simulations have been implemented based on methane gas. It is found that apparent permeability is strongly dependent on pore size, porosity, and tortuosity, and weakly dependent on surface diffusivity coefficient and pore-surface roughness through sensitivity

analysis. The increased viscosity can reduce the total molar flux in the inorganic pores up to 66.0% under the typical shale gas reservoir conditions. The viscous flow mechanism cannot be neglected at any pore sizes under reservoir conditions while the Knudsen diffusion is found to be important in the pore size below 2 nm and pressure less than 35.0 MPa. The contribution of surface diffusion cannot be ignored when the pore size is below 10 nm and the pressure less than 15.0 MPa.

3.2 Mathematical Modeling

Figure 3.1 presents the schematic diagram of a conceptual layered model for a straight capillary tube with a radius of R_0. As can be seen, the tube is hypothetically divided into three zones by the virtual boundary with a radius of r and the effective radius of R_e. It is assumed that the central cylindrical zone (i.e., blue zone) and the middle annular zone (i.e., pink zone within R_e) are dominated by inter-molecular collisions and collisions occur between molecules and the wall of the capillary tube, respectively. As aforementioned, the transition flow can be rationally assumed to be a function of the viscous flow and the Knudsen diffusion (Javadpour, 2009; Veltzke and Thöming, 2012; Wu et al., 2016). As such, the gas transport in the central and middle annular zones can be described by coupling viscous flow and Knudsen diffusion (Bravo, 2007; Civan, 2010; Firouzi et al., 2014). The outer annular zone is dominated by surface diffusion (i.e., between R_e and R_0) where large amounts of molecules are adsorbed on the wall and hop forward by the chemical potential. Compared with organic pores, sparse molecules can be adsorbed on the wall in inorganic pores (Bui and Akkutlu, 2017). Hence, the surface diffusion layer (i.e., outer annular zone) can be neglected and R_e can be equal to R_0. It is postulated that the gas transport model is developed under steady-state and isothermal condition. In addition, the pore confinement effect

which may lead to the critical property shift in nanopores is not considered in this work because it has not been well understood yet. Based on the conceptual layered model, the mathematical model in our work is derived as follows.

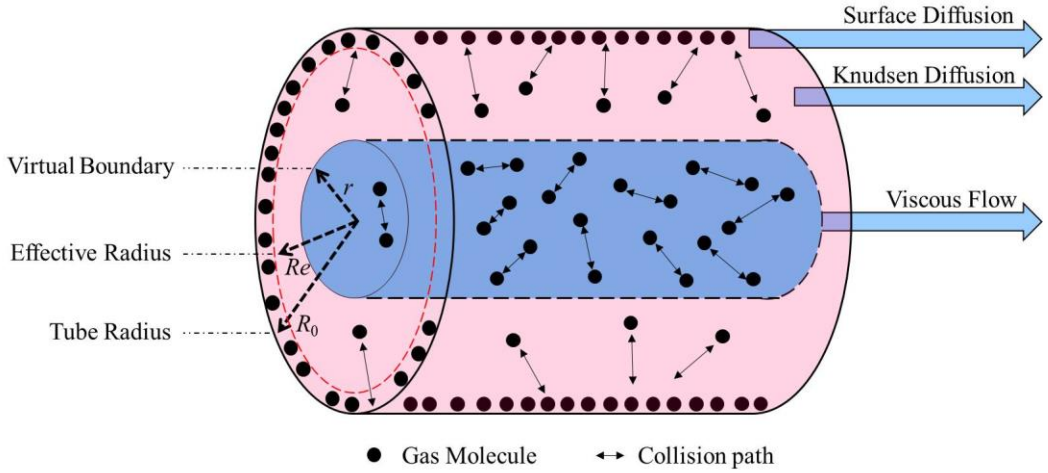

Figure 3.1: Schematic diagram of the conceptual layered model of a straight capillary tube (Blue central cylindrical zone - viscous flow; Pink middle annular zone - Knudsen diffusion; Outer annular zone – surface diffusion).

3.2.1 Viscous Flow in the Central Cylindrical Zone

Given the aforementioned assumptions, the viscous flow velocity can be represented by Poiseuille velocity coupled with a second-order slip velocity. However, the implementation of second-order slip boundary in Eq. 2.1 involves the calculation of $\left(\partial^2 u/\partial n^2\right)_s$ which leads to computational difficulties. Thus, a unified second-order velocity model is adopted for the simplicity (Beskok and Karniadakis, 1999) as follows.

$$u_s = \frac{Kn}{1-sKn}\left(\frac{\partial u}{\partial n}\right)_s \tag{3.1}$$

where s is the slip coefficient. The linearized Boltzmann solution has validated that $s=-1$ gives the best fitting of the slip velocity by the direct numerical solution of the BE (Civan, 2010). Given

the continuity equation by Eq. 2.2, constrained boundaries by Eq. 2.3, and slip velocity model by Eq. 3.1, the explicit velocity expression of viscous flow in central zone can be characterized by

$$v_v = -\frac{R_e^2}{4\eta}\left[1-\left(\frac{r}{R_e}\right)^2 + 2\frac{Kn}{1-sKn}\right]\nabla P \tag{3.2}$$

where v_v is the viscous flow velocity, R_e is the effective radius, η is the gas viscosity, r is the radius with respect to the central axis, Kn is the Knudsen number defined as λ/R_e, ∇P is the pressure gradient along the capillary. Note that $(\partial u/\partial n)_s$ in Eq. 3.2 is expressed as $(\partial u/\partial n)_s = -(\partial u/\partial r)_s \cdot R_0$. Subsequently, the viscous molar flow rate, Q_v, is obtained by the integration with respect to the radius,

$$Q_v = \frac{\bar{P}}{RT}\int_0^r v_v \cdot 2\pi r dr \tag{3.3}$$

where R is the universal gas constant, T is the temperature, $\bar{P}$ is the average pressure across the capillary tube.

3.2.2 Knudsen Diffusion in the Middle Annular Zone

Roth (1982) has claimed that the molar flow rate, Q_k, in the Knudsen diffusion zone which is controlled by non-equilibrium dissipative forces can be quantified by

$$Q_k = -\frac{4}{3}\frac{\bar{v}}{RT}\frac{A^2}{S}\nabla P \tag{3.4}$$

where A is the cross-section area of Knudsen diffusion and S is the perimeter of the cross-section. $\bar{v}$ is the apparent molecular thermal velocity expressed as $\bar{v} = \sqrt{(8RT)/(\pi M)}$ where M is

molar mass. Given Eq. 3.4, the Knudsen diffusion molar flow rate in the middle annular zone can be determined as follows.

$$Q_k = -\frac{4}{3}\frac{\bar{v}}{RT}\frac{\left[\pi R_e^2 - \pi r^2\right]^2}{2\pi R_e}\nabla P \tag{3.5}$$

Consequently, the total molar flux of free gas flow in the capillary tube, J_b, can be calculated by the superposition of the viscous flow and Knudsen diffusion according to Eqs. 3.3 and 3.5.

$$J_b = \frac{Q_v + Q_k}{\pi R_0^2} = \left[\frac{\bar{P}}{RT}\int_0^r v_v \cdot 2\pi r dr - \frac{4}{3}\frac{\bar{v}}{RT}\frac{\left[\pi R_e^2 - \pi r^2\right]^2}{2\pi R_e}\nabla P\right] \Big/ \pi R_0^2 \tag{3.6}$$

3.2.3 Surface Diffusion in the Outer Annular Zone

Surface diffusion is a complicated process of adsorption-phase transport which can be categorized into adatom diffusion and cluster diffusion. Adatom diffusion can be activated by a variety of mechanisms including hopping, atomic exchange, and vacancy diffusion. On the other hand, cluster diffusion occurs due to multiple mechanisms including dislocation, glide diffusion, and shearing (Kou et al., 2017). Various models have been proposed to characterize the surface diffusion phenomenon, among which Fick's first law of diffusion has been widely accepted due to its mathematical simplicity and physical validity (Xiong et al., 2012). Hence, Fick's first law of diffusion is applied to quantify the surface molar flux, J_s, in which the adsorbed gas molecules hop forward by the concentration gradient under the Langmuir isothermal condition. It is also presumed that adsorption/desorption process can reach the equilibrium instantly to satisfy the requirement of Langmuir equation (Cunningham and Williams, 1980; Fathi and Akkutlu, 2009; Jia et al., 2018b). This Fick's equation is given as

$$J_s = -D_s \nabla C_a \tag{3.7}$$

where D_s is the surface diffusion coefficient, C_a is the concentration of adsorbed gas. It indicates the concentration of adsorbed gas, C_a, can be calculated by monolayer Langmuir model (Xiong, et al., 2012; Wasaki and Akkutlu, 2015; Sheng et al., 2020)

$$C_a = C_{a\max} \frac{\bar{P}}{\bar{P} + P_L} \tag{3.8}$$

where P_L is the Langmuir pressure, $C_{a\max}$ is the maximum adsorption capacity in the organic nanopore. Additionally, Wasaki and Akkutlu (2015) pointed out that $C_{a\max}$ can be expressed by $C_{a\max} = \left(V_L \rho_{STG} \rho_{grain}\right) \big/ \left(\varepsilon_k M\right)$, where V_L is Langmuir volume indicating the maximum adsorbed phase volume per unit total grain mass at standard condition, ρ_{STG} is the gas density at standard condition, ρ_{grain} is the grain density, ε_k is the ratio of organic grain volume to the total grain volume. Thus, the molar flux of surface diffusion can be derived as

$$J_s = -D_s C_{a\max} \frac{P_L}{\left(\bar{P} + P_L\right)^2} \nabla P \tag{3.9}$$

3.2.4 Surface Determination of Virtual Boundary r and Effective Radius R_e

As defined in Eqs. 3.3 and 3.5, the radius of virtual boundary (i.e., r) plays a significant role in the calculations of the viscous flow and Knudsen diffusion. It implies that determining the radius of virtual boundary under a given condition is pivotal to the mathematical modeling of the gas transport in the conceptual layered model. However, no efforts have been made to quantify the virtual boundary, although Bravo (2007) preliminarily discussed the concept of virtual boundary. In this work, we propose to utilize an analytical molecular kinetics approach based on Kennard's

kinetic theory (1938) for quantitatively determining the radius of virtual boundary in the conceptual layered model. For simplicity, Kennard (1938) proposed several assumptions: i) a group of molecules with velocity $\bar{v}$ is flowing through a gas-molecules-filled cylindrical tube where the molecules in the flowing group mutually collide with the originally existing molecules. Moreover, a molecule is excluded from the flowing group once it experiences the collision; ii) the inter-molecular force is negligible; and iii) the derivation is based on elastic binary collisions; iv) the gas in the model is a single component.

Based on the assumptions, the number of molecules (i.e., *N*) not experiencing a collision after time interval *dt* is defined by Kennard (1938) as

$$N = -\frac{1}{\theta}\frac{dN}{dt} \tag{3.10}$$

where θ is the inter-molecular collision probability per unit time. To explicitly solve the Kennard's collision model (i.e., Eq. 3.10), θ can be represented by an equivalent kinetic equation $\bar{v}/\lambda$ proposed by Bird (1994). Hence, the number of gas molecules not experiencing collisions at any given time can be determined by

$$\int \frac{1}{N} dN = -\int \theta dt = -\int \frac{\bar{v}}{\lambda} dt \tag{3.11}$$

where λ is the mean free path of molecules moving at average velocity $\bar{v}$. By defining the initial number of molecules in the flowing group as N_0, Eq. 3.11 is integrated as follows.

$$N = N_0 \exp\left(-\frac{\bar{v}\Delta t}{\lambda}\right) \tag{3.12}$$

where $\bar{v}\Delta t$ denotes the distance of molecules with velocity $\bar{v}$ traversing within Δt. Note that such a distance can be either longer or shorter than the mean free path (i.e., λ) of molecules in the

cylindrical tube. However, the $\bar{v}\Delta t$ is constrained by the characteristic length of the cylindrical tube. As such, we further propose to use ξR_e as an approximation of such a distance, where ξ is an empirical parameter characterizing the chemical confinement effect caused by interactions between molecules and the pore-wall. Furthermore, as Knudsen number (i.e., *Kn*) can be expressed by λ / R_e (Bird, 1994), Eq. 3.12 can be rearranged as follows.

$$\frac{N}{N_0} = \exp\left(-\frac{\xi R_e}{\lambda}\right) = \exp\left(-\xi \frac{1}{Kn}\right) \tag{3.13}$$

Eq. 3.13 characterizes the fraction of molecules not experiencing inter-molecular collisions in the cylindrical tube.

As is stated in the conceptual model, the inter-molecular collisions only occur in the central zone while molecule-wall collisions only occur in the middle annular zone. Therefore, the number of molecules experiencing inter-molecular collisions per unit time is equivalent to the number of molecules in the central zone per unit time. Given the number density of molecules *n* (i.e., number of molecules per unit volume), the number of molecules experiencing inter-molecular collisions (i.e., N_c), in the central zone over a time interval Δt can be determined by (the details can be seen in Appendix C)

$$N_c = n\pi r^2 \bar{v}_{nc} \Delta t \tag{3.14}$$

where $\bar{v}_{nc}$ denotes the average velocity component normal to the central zone cross-section, $\bar{v}_{nc}\Delta t$ is the average translation distance of molecules over Δt. Similarly, the number of molecules experiencing either inter-molecular or molecule-wall collisions per unit time is equivalent to the number of molecules in the central and middle annular zone per unit time. By assuming that the density distribution of molecules in both central and middle annular zones is uniform, the total

number of molecules for free gas flow in the central and middle annular zone (i.e., N_t) over Δt can be achieved as (the details can be seen in Appendix C)

$$N_t = n\pi R_e^2 \bar{v}_{nt} \Delta t \tag{3.15}$$

where $\bar{v}_{nt}$ denotes the average velocity component normal to both the central and middle annular zone cross-section. As aforementioned, the inter-molecular and molecule-wall collisions only appear in the central and middle annular zones, respectively. Therefore, the fraction of inter-molecular collisions in the cylindrical tube can also be derived as $N_c / N_t = \kappa(r^2 / R_e^{\,2})$, where κ is an empirical parameter representing the heterogeneity of velocity directions (the details can be seen in Appendix C). Then, by incorporating Eq. 3.13 we obtain

$$\frac{N_c}{N_t} = 1 - \frac{N}{N_0} = 1 - \exp\left(-\xi \frac{1}{Kn}\right) \tag{3.16}$$

Eq. 3.16 describes the statistical proportion of molecules colliding mutually within the central zone. Subsequently, Eq. 3.16 is incorporated into the new unified gas transport model and then combined with Eqs. 3.14 and 3.15 to determine the virtual boundary

$$r = \frac{1}{\sqrt{\kappa}} R_e \sqrt{1 - \exp\left(-\xi \frac{1}{Kn}\right)} \tag{3.17}$$

However, the adsorbed layers of molecules in organic nanopores may cause the oscillation of density distribution near the pore-wall (Kazemi and Takbiri-Borujeni, 2016). Fortunately, it has been proven that the multilayer adsorption in molecular simulations can be treated as a monolayer adsorption in analytical derivations under Langmuir isothermal conditions (Ambrose et al., 2012; Rahmani and Akkutlu, 2013; Wasaki and Akkutlu, 2015, Riewchotisakul and Akkutlu, 2016). Figure 3.2 (a) illustrates the discrete density profile of methane gas in an organic nanopore (Ambrose et al., 2012). It can be seen there are four density layers in the surface diffusion zone

ranging from 0.281 to 0.126 g/cc. The gas molecules in the surface diffusion zone are considered as adsorbed gas, while the gas molecules in the viscous flow and Knudsen diffusion zones are in free gas phase. The molecular simulations have indicated that the multilayer adsorption in Figure 3.2 (a) can be simplified to a monolayer adsorption with the density of 0.331 g/cc as shown in Figure 3.2 (b) for modeling purpose. Such treatment does not undermine the nature integrity of adsorption phenomenon and calculation accuracy. It also provides the validity support to develop analytical models using monolayer Langmuir model (Wasaki and Akkutlu, 2015). Therefore, it is reasonable to deal with density distribution in the surface diffusion zone as the monolayer uniform-distribution in our conceptual model. Also, the uniform density distribution in central and middle annular zones is not affected by the density oscillations in the surface diffusion zone.

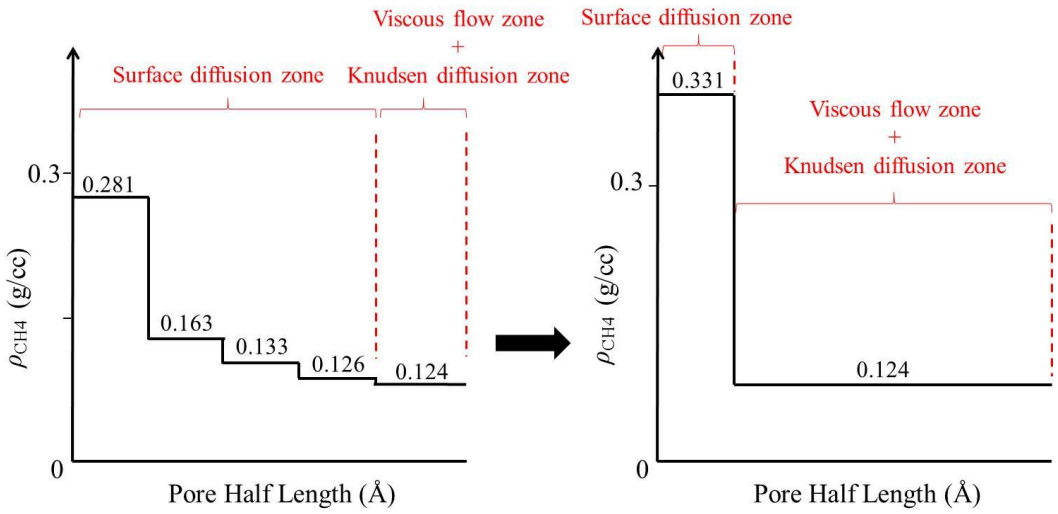

Figure 3.2: Schematic Discrete-density profile for methane at 176 ºF in a 3.93 nm-size-nanopore (a) is equivalent to the density profile using Langmuir single-layer adsorption model (b) (Ambrose et al., 2012).

The effective radius, R_e, is the radius corrected for the presence of adsorbed gas molecules in the organic nanopore. Xiong et al. (2012) proposed the monolayer thickness may be different from the

molecule diameter of adsorbed gas. Accordingly, the effective radius changes with the thickness of monolayer. A correlation introduced by Xiong et al. (2012) is used in this work:

$$R_e = R_0 - d_m \frac{\bar{P}}{\bar{P} + P_L} \tag{3.18}$$

where d_m is nominal molecule size, $\bar{P}$ is the average pressure across the capillary tube. Given the explicitly defined virtual boundary by Eq. 3.17 and effective radius by Eq. 3.18, the total free gas molar flux without including surface diffusion in the cylindrical tube, J_b, can be derived from Eq. 3.6.

$$J_b = w_v J_v + w_k J_k = -w_v \frac{R_e^4}{R_0^2} \frac{\bar{P}}{8\eta RT} \nabla P - w_k \frac{2}{3} \frac{R_e^3}{R_0^2} \sqrt{\frac{8}{\pi RTM}} \nabla P \tag{3.19}$$

$$w_v = \frac{1}{\kappa}\left[1 - \exp\left(-\xi \frac{1}{Kn}\right)\right]\left\{2 - \frac{1}{\kappa}\left[1 - \exp\left(-\xi \frac{1}{Kn}\right)\right] + \frac{4Kn}{1 - sKn}\right\} \tag{3.20}$$

$$w_k = \left\{1 - \frac{1}{\kappa}\left[1 - \exp\left(-\xi \frac{1}{Kn}\right)\right]\right\}^2 \tag{3.21}$$

where w_v and w_k are weights of the viscous molar flux and the Knudsen diffusion molar flux, respectively, which are used to ration the contribution of the viscous flow and Knudsen diffusion in the total free gas flow, respectively. It is noted that Eq. 3.19 can be used to calculate the total molar flux in inorganic nanopores by setting $R_e = R_0$ because surface diffusion can be ignored in inorganic pores as aforementioned.

The total molar flux in organic nanopores, J_t, can be characterized by the superposition of free gas flow and surface diffusion as follows,

$$J_t = w_v J_v + w_k J_k + J_s$$
$$= -w_v \frac{R_e^4}{R_0^2} \frac{\bar{P}}{8\eta RT} \nabla P - w_k \frac{2}{3} \frac{R_e^3}{R_0^2} \sqrt{\frac{8}{\pi RTM}} \nabla P - D_s C_{a\max} \frac{P_L}{\left(\bar{P} + P_L\right)^2} \nabla P \quad (3.22)$$

It is important to point out that the introduction of the Knudsen number in Eq. 16 enables the new unified gas transport model to calculate the gas molar flux of the full flow spectrum. In contrast, the applicability of Bravo's model (2007) is challenged since the total flux is computed by piecewise functions. Moreover, four empirical parameters involved in Bravo's model largely increase the uncertainties in the process of calculating fluxes under various experimental conditions. Such a limitation has been completely avoided in the proposed unified gas transport model with the determined virtual boundary. In addition, Klinkenberg (1941) considered a non-equilibrium region as a Knudsen layer which was near one mean free path thickness. In the present work, the thickness of the non-equilibrium region is explicitly expressed by the virtual boundary. In this case, the Knudsen layer determined by the local Knudsen number can reflect the pore-scale characteristics rather than a fixed value suggested by Klinkenberg.

3.2.5 Characterization of Roughness and Rarefaction

The roughness and rarefaction effect have remarkable influences on the performance of gas flow in nano-scale pores (Darabi et al., 2012). Considering the fractal dimension of the pore surface, Coppens and Dammers (2006) quantified the structural heterogeneity of the media by using a fractal dimension coefficient, D_f, which varied between 2.0 and 3.0 indicating changes from a smooth surface to a space-filling surface. Although the accurate estimation of D_f is unavailable from independent experiments, Darabi et al. (2012) have recommended a rational range of D_f for

various shale samples (i.e., $2.0 \le D_f \le 2.5$). Therefore, the Knudsen molar flux term in Eq. 3.22, i.e., J_k, is modified to represent the effect of roughness as follows (Wu et al., 2016).

$$J_k^n = \delta^{(D_f-2)} J_k = -\frac{2}{3}\frac{R_e^3}{R_0^2}\delta^{(D_f-2)}\sqrt{\frac{8}{\pi RTM}}\nabla P \tag{3.23}$$

where δ is the ratio of the normalized molecule diameter to the local effective pore diameter, i.e., $d_m/(2R_e)$. Note $\delta^{(D_f-2)}$ is termed as the roughness coefficient which represents coupled effects of surface fractal dimension, effective pore size, and gas molecule size (Darabi et al., 2012).

Since the confinement of nano-spaces may cause significant influences on the dynamic gas viscosity, it is essential to modify the dynamic gas viscosity to characterize the diffusion of momentum resulted from inter-molecular collisions so as to embody the increased rarefaction effect (Roohi and Darbandi, 2009). The degree of rarefaction is typically calculated by an explicit function of the local Knudsen number (Michalis et al., 2010). Therefore, we modified the viscous molar flux in Eq. 3.22, i.e., J_v, by incorporating a rarefaction term proposed by Beskok and Karniadakis (1999), which yields

$$J_v^n = (1+\alpha Kn)J_v = -(1+\alpha Kn)\frac{R_e^4}{R_0^2}\frac{\bar{P}}{8\eta RT}\nabla P \tag{3.24}$$

where α is a dimensionless rarefaction coefficient, which can be obtained from an analysis of the linearized Boltzmann equation (Loyalka and Hamoodi, 1990) or experimental results (Tison, 1993). Beskok and Karniadakis (1999) recommended calculating the α by using the equation $\alpha = 2\alpha_0 \tan^{-1}\left(\alpha_1 Kn^{\beta}\right)/\pi$ where $\alpha_0 = 64/\left[3\pi(1-4/s)\right]$, α_1 and β are fitting parameters obtained from experiments, *s* is equal to -1 following the second-order slip boundary condition.

Therefore, the total molar flux in Eq. 3.22 can be updated by integrating the roughness and rarefaction effect as follows.

$$\begin{aligned} J_t^n &= w_v J_v^n + w_k J_k^n + J_s \\ &= -w_v\left(1+\alpha Kn\right)\frac{R_e^4}{R_0^2}\frac{\bar{P}}{8\eta RT}\nabla P - w_k\frac{2}{3}\frac{R_e^3}{R_0^2}\delta^{\left(D_f-2\right)}\sqrt{\frac{8}{\pi RTM}}\nabla P - D_s C_{a\max}\frac{P_L}{\left(\bar{P}+P_L\right)^2}\nabla P \end{aligned} \tag{3.25}$$

3.2.6 Characterization of Real Gas Effect

To represent the differences between ideal gas and real gas, compressibility factor, *Z*, is considered and incorporated into the developed ideal gas model, i.e., Eq. 3.25. The compressibility factor is a dimensionless parameter, which represents the deviation behavior of real gas from the ideal gas (Loebenstein, 1971). Since Standing-Katz correlation (1942) failed to make accurate predictions of compressibility factor at high pressures, Mahmoud (2013) improved such a correlation as follows.

$$Z = 0.702e^{-2.5T_r}P_r^2 - 5.524e^{-2.5T_r}P_r + 0.044T_r^2 - 0.164T_r + 1.15 \tag{3.26}$$

where P_r is the reduced pressure expressed by $P_r = \bar{P}/P_c$, P_c is the critical pressure, T_r is the reduced temperature expressed by $T_r = T/T_c$, and T_c is the critical temperature. Furthermore, the dynamic viscosity of real gas also changes with reservoir pressures and temperatures compared to the constant value under ideal gas conditions. Sutton (2007) have developed one reliable and superior correlation to estimate the dynamic viscosity of light hydrocarbon gas mixtures, which is expressed as follows.

$$\eta_r = 10^{-7}\eta\exp\left[X\left(\frac{\rho}{1000}\right)^Y\right] \tag{3.27}$$

$$\eta\zeta = 0.807T_r^{0.618} - 0.357\exp\left(-0.449T_r\right) + 0.340\exp\left(-4.058T_r\right) + 0.018 \tag{3.28}$$

$$\zeta = \frac{0.949T_c^{\frac{1}{6}}}{P_c^{\frac{2}{3}}\sqrt{1000M}} \tag{3.29}$$

$$X = 3.47 + \frac{1588}{1.8T} + 0.9M \tag{3.30}$$

$$Y = 1.66378 - 0.04679X \tag{3.31}$$

where η_r is the real gas viscosity, $\rho = \left(\bar{P}M\right)/\left(ZRT\right)$. Considering the compressibility factor and dynamic viscosity, the Knudsen number conditioned to real gas effect is obtained as $Kn_r = \eta_r\sqrt{\pi ZRT/\left(2M\right)}/\bar{P}R_e$. The viscous flux, J_{vr}^n, of real gas is obtained as follows.

$$J_{vr}^n = -\left(1 + \alpha_r Kn_r\right)\frac{R_e^4}{R_0^2}\frac{\bar{P}}{8Z\eta_r RT}\nabla P \tag{3.32}$$

Subsequently, the Knudsen diffusion molar flux, i.e., J_{kr}^n, for real gas flow is rewritten as

$$J_{kr}^n = -\frac{2}{3}\frac{R_e^3}{R_0^2}\bar{P}\delta^{\left(D_f-2\right)}C\sqrt{\frac{8}{\pi ZRTM}}\nabla P \tag{3.33}$$

The surface diffusion molar flux, i.e., J_{sr}, for real gas flow is expressed as

$$J_{sr} = -D_s C_{a\max}\frac{P_L\bar{P}ZC}{\left(\bar{P} + ZP_L\right)^2}\nabla P \tag{3.34}$$

where $C = \frac{1}{\bar{P}} - \frac{1}{Z}\frac{dZ}{dP}$ indicating the volume compressibility of real-gas phase in Eqs. 3.33 and 3.34.

3.2.7 Gas Flow in Porous Media

In this work, it is assumed that the effect of interconnected matrix structure of porous media on gas flow is negligible. Hence, the new unified gas transport model for a capillary tube can be extended to bundles of tortuous capillaries with identical geometries, which is sufficient to represent porous media (Wu et al., 2017). Accordingly, the molar flux in the single-tube model can be up-scaled by using a correction factor, which assembles both porosity, ϕ, and tortuosity, τ, of the porous media (Wu et al., 2016). In this case, the total molar flux for real gas, i.e., J_{tr}^{n}, in porous media can be derive as

$$\begin{aligned} J_{tr}^{i} &= \frac{\phi}{\tau} w_{vr} J_{vr}^{n} + \frac{\phi}{\tau} w_{kr} J_{kr}^{n} + \frac{\phi}{\tau} J_{sr} \\ &= -w_{vr} \frac{\phi}{\tau} \left(1 + \alpha_r Kn_r\right) \frac{R_e^4}{R_0^2} \frac{\bar{P}}{8Z\eta_r RT} \nabla P \\ &\quad -w_{kr} \frac{\phi}{\tau} \frac{2}{3} \frac{R_e^3}{R_0^2} \bar{P} \delta^{\left(D_f - 2\right)} C \sqrt{\frac{8}{\pi ZRTM}} \nabla P - \frac{\phi}{\tau} D_s C_{a\max} \frac{P_L \bar{P} ZC}{\left(\bar{P} + ZP_L\right)^2} \nabla P \end{aligned} \tag{3.35}$$

$$w_{vr} = \frac{1}{\kappa}\left[1 - \exp\left(-\xi \frac{1}{Kn_r}\right)\right]\left\{2 - \frac{1}{\kappa}\left[1 - \exp\left(-\xi \frac{1}{Kn_r}\right)\right] + \frac{4Kn_r}{1 - sKn_r}\right\} \tag{3.36}$$

$$w_{kr} = \left\{1 - \frac{1}{\kappa}\left[1 - \exp\left(-\xi \frac{1}{Kn_r}\right)\right]\right\}^2 \tag{3.37}$$

To apply the newly proposed model at different scales, the viscous molar flux and Knudsen diffusion molar flux have been normalized by using Eq. 3.38 and Eq. 3.39, respectively. The normalized viscous molar flux, i.e., J_{vr_norm}, and normalized Knudsen diffusion molar flux, i.e., J_{kr_norm}, are presented as

$$J_{vr\_norm} = \frac{J_{tr}^i}{J_{vr}^i} = w_{vr}\left(1+\alpha_r Kn_r\right) + w_{kr}\delta^{\left(D_f-2\right)}\frac{64}{3\pi}\bar{P}CKn_r \tag{3.38}$$

$$J_{kr\_norm} = \frac{J_{tr}^i}{J_{kr}^i} = w_{vr}\left(1+\alpha_r Kn_r\right)\frac{3\pi}{64\delta^{\left(D_f-2\right)}C\bar{P}Kn_r} + w_{kr} \tag{3.39}$$

where $J_{vr}^i = -\frac{\phi}{\tau}\frac{R_e^4}{R_0^2}\frac{\bar{P}}{8Z\eta_r RT}\nabla P$, $J_{kr}^i = -\frac{\phi}{\tau}\frac{2}{3}\frac{R_e^3}{R_0^2}\bar{P}\delta^{\left(D_f-2\right)}C\sqrt{\frac{8}{\pi ZRTM}}\nabla P$. To quantify the real gas effect, the deviation of molar fluxes between real gas model and ideal gas model, i.e., ψ as shown in Eq. 3.40, has been calculated and discussed in Section 3.3.

$$\psi = \frac{J_{tr}^i - J_t^i}{J_t^i}\times 100\% \tag{3.40}$$

where J_{tr}^i is total gas molar flux for real gas in porous media and J_t^i is total gas molar flux for ideal gas in porous media which is expressed as $J_t^i = \phi J_t^n / \tau$.

Considering the importance of permeability to shale reservoir simulations, it is essential to evaluate the feasibility of the unified gas transport model to estimate the permeability. As such, the effective apparent permeability for real gas in porous media, i.e., K_{tr}^i, is determined as,

$$\begin{aligned} K_{tr}^i &= \frac{\phi}{\tau}K_{tr} = \frac{\phi}{\tau}w_{vr}K_{vr} + \frac{\phi}{\tau}w_{kr}K_{kr} + \frac{\phi}{\tau}K_{sr} \\ &= w_{vr}\frac{\phi}{\tau}\left(1+\alpha_r Kn_r\right)\frac{R_e^4}{8R_0^2} + w_{kr}\frac{\phi}{\tau}\frac{8R_e^4}{3\pi R_0^2}\delta^{\left(D_f-2\right)}C\bar{P}Kn_r \\ &+ \frac{\phi}{\tau}D_s C_{a\max}\frac{P_L Z^2 CRT\eta_r}{\left(\bar{P}+ZP_L\right)^2} \end{aligned} \tag{3.41}$$

where K_{vr}, K_{kr}, and K_{sr} is the apparent permeability of viscous flow, Knudsen diffusion and surface diffusion, respectively.

3.3 Validation: Physical and Numerical Experiments

Data from the cylindrical tube have been properly collected to validate the developed gas transport model for both organic and inorganic nanopores by including and excluding the surface diffusion. Table 3.1 lists the experimentally measured and numerically simulated data used to validate the gas flow in inorganic nanopores where surface diffusion is neglected. It is known that the experimental flux data in nanopores at high pressures can be rarely found in literature. The experimental fluxes at relatively low pressures covering slip and transition flow regimes (Tison, 1993; Ewart et al., 2007; Yamaguchi et al., 2011) are well utilized for validation since it has been claimed that the shale gas transport is mainly characterized as slip and transition flow (Wu et al. 2016). Even though the numerical solution of the linearized Boltzmann equation and the lattice Boltzmann model is time-consuming and computationally expensive, it has been widely recognized as one of the most accurate modeling approaches. In this work, the data from numerical solutions for methane gas transport in nanopores (Loyalka and Hamoodi, 1990; Landry et al., 2016) are also collected for the model validation in Table 3.1. As for the model validation considering the surface diffusion in organic nanopores, the molecular dynamics (MD) data from Yu et al. (2018) are used in this work. The detailed parameters in MD simulation are tabulated in Table 3.2. The simulation system and methane molecules are generated by grand canonical Monte Carlo simulations under pressures from 5 to 50 MPa. The apparent permeability was simulated by non-equilibrium MD simulations.

Table 3.1: Summary of parameters used in rarefied gas model validations

Literature	Data Sources	Gas Type	Tube Size, d	Temperature, T
Tison (1993)	Experiments	Helium	1 cm	298 K
Ewart et al. (2007)	Experiments	Nitrogen	25.27 μm	298 K
Yamaguchi et al. (2011)	Experiments	Nitrogen	320 μm	293 K
Loyalka and Hamoodi (1990)	Numerical Solutions	Methane	10 nm	400 K
Landry et al. (2016)	Numerical Solutions	Methane	8.446 nm	400 K

Table 3.2: Summary of parameters used in organic nanopore validations (Yu et al., 2018)

Parameters	Symbol	Unit	Values
Maximum adsorption capacity	C_{amax}	mol/m^3	798
Surface diffusivity coefficient	D_s	m^2/s	1.1×10^{-7}
Reservoir temperature	T	K	298
Universal gas constant	R	J/(mol·K)	8.314
Nominal methane molecule size	d_m	nm	0.38
Pore size	d	nm	10.0
Methane molar mass	M	kg/mol	0.016
Methane critical pressure	P_c	Pa	4.60×10^6
Methane critical temperature	T_c	K	190.6

The calculation of dimensionless molar flux and apparent permeability requires estimations of three empirical parameters: D_f, ξ, and κ which should be optimized. Since D_f, ξ, and κ are independent continuous variables with certain constraints, the objective functions can be written as

$$\min f_1(D_{f1},\xi_1)=\sum_{i=1}^{I}\left(J_{vr\_norm}-J_{vr\_data}\right)^2 \tag{3.42}$$

$$\min f_2(D_{f2},\xi_2)=\sum_{j=1}^{J}\left(J_{kr\_norm}-J_{kr\_data}\right)^2 \tag{3.43}$$

$$S.T.\ \ 2\le D_f\le 2.5 \tag{3.44}$$

$$0 < \xi \le \frac{\sqrt{R_0^2 + L^2}}{R_0} \tag{3.45}$$

$$\kappa > 0 \tag{3.46}$$

where J_{vr_data} and J_{kr_data} are the collected reference data of normalized viscous molar flux and normalized Knudsen diffusion molar flux, respectively. In this work, a single objective function (i.e., Eq. 3.42) is needed for the data from Tison (1993), Ewart et al. (2007), Landry et al. (2016), and Yu et al. (2018), whereas two objective functions (i.e., Eqs. 3.42 and 3.43) need to be solved concurrently for the data from Loyalka and Hamoodi (1990) because it includes both normalized-viscous-flux and Knudsen-diffusion-flux.

The CONOPT solver which is a strong all-around nonlinear problem (NLP) solver in General Algebraic Modeling System (GAMS) software is used in this work to perform the optimization work. As for the multi-objective optimization (i.e., Eqs. 3.42 and 3.43), a pre-treatment of ε-constraint method (Haimes et al., 1971) is applied to transform it to the single-objective nonlinear problem so that it can be solved by using CONOPT solver. We assume f_1 as the primary objective function for maximization and f_2 as the constraint. Hence, Eqs. 3.42-3.46 are rearranged as

$$\max\ f_1(D_f, \xi) = \sum_{i=1}^{I} \left(J_{vr\_norm} - J_{vr\_data} \right)^2 \tag{3.47}$$

$$S.T.\ \ 2 \le D_f \le 2.5 \tag{3.48}$$

$$0 < \xi \le \frac{\sqrt{R_0^2 + L^2}}{R_0} \tag{3.49}$$

$$\kappa > 0 \tag{3.50}$$

$$f_2\left(D_f, \xi\right) \leq \varepsilon \tag{3.51}$$

Since an improper selection of ε can corrupt the optimization, Carmichael (1980) suggested a mathematical guideline for selecting ε,

$$f_1\left(x_i^*\right) < \varepsilon_i \leq f_2\left(x_i^*\right) \tag{3.52}$$

Subsequently, the CONOPT solver can be used to solve Eqs. 3.47-3.52 and obtain multiple local optimal solutions which form a boundary called Pareto-optimal front in a new data space formed by two objective functions. Fairly good solutions to the multi-objective problems can always be found on this Pareto-optimal front (Ruiz-Canales and Rufian-Lizana, 1995).

3.4 Results and Discussion

3.4.1 Validation Results

The optimized three parameters of D_f^*, ξ^*, and κ^* have been tabulated in Table 3.3. A complete Pareto-optimal front has been obtained for the data from Loyalka and Hamoodi (1990) as shown in Figure 3.3. The black points are a series of optimal objective function values $\left(f_1^*, f_2^*\right)$ with respect to the optimal D_f^*, ξ^*, and κ^*. Fairly good solutions are located in the red circle. D_f^* in Table 3.3 is constrained between 2 and 2.5 indicating the changes from a smooth surface to a rough surface (Darabi et al, 2012). Thus, $D_f^* = 2.00$ corresponds to the numerical simulation reference data since smooth surface are assumed in those models. Meanwhile, it is further demonstrated that D_f^* larger than 2.00 corresponds to the experimental reference data. Values of ξ^* and κ^* in Table 3.3 vary for each gas type.

Table 3.3: Summary of optimal solutions

Literature	Gas Type	Objective Function	D_f^*	ξ^*	κ^*
Tison (1993)	Helium	Single	2.15	0.97	1.05
Ewart et al. (2007)	Nitrogen	Single	2.05	1.54	0.74
Yamaguchi et al. (2011)	Nitrogen	Single	2.05	1.54	0.74
Loyalka and Hamoodi (1990)	Methane	Multiple	2.00	0.46	0.91
Landry et al. (2016)	Methane	Single	2.00	0.46	0.91
Yu et al. (2018)	Methane	Single	2.00	0.46	0.91

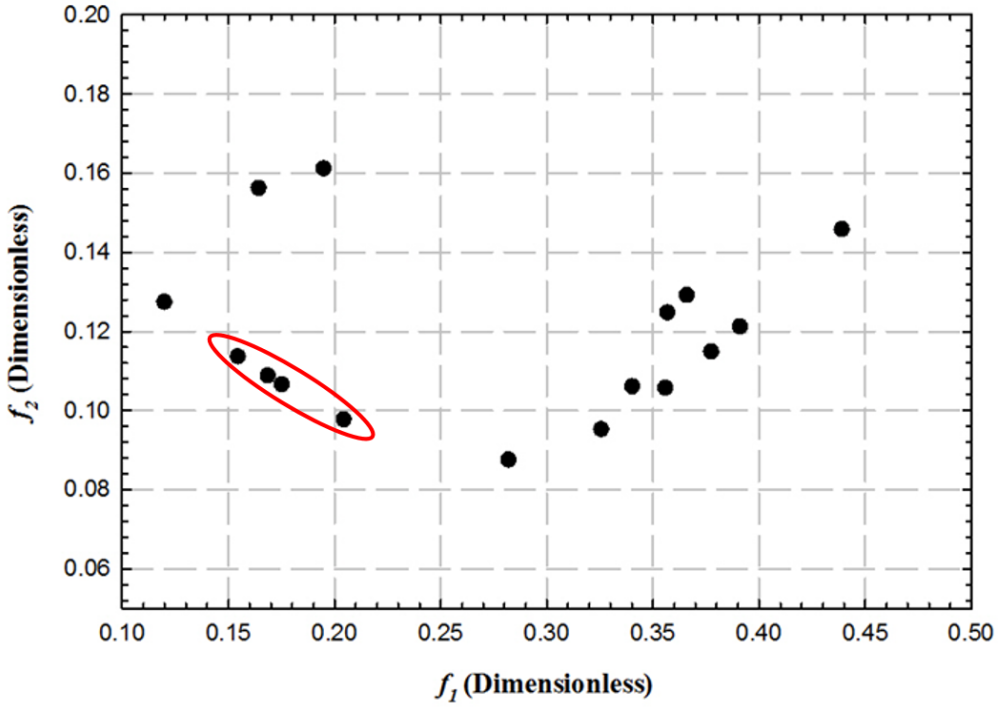

Figure 3.3: Pareto-optimal front obtained using ε-constraint method.

It can be seen in Table 3.3 that the optimized three parameters are same for all nitrogen data collected from two different resources, i.e., $D_f^* = 2.00$, $\xi^* = 1.54$, $\kappa^* = 0.74$. They are also same for all methane data collected from three different resources, i.e., $D_f^* = 2.00$, $\xi^* = 0.46$, $\kappa^* = 0.91$. Such finding indicates that the optimized parameters in this work can serve as reasonable empirical values for corresponding types of gas without the necessity of conducting additional experiments.

It allows the proposed analytical model to be easily implemented with the wider applications. As for the computation speed, the automated solver of CONOPT in GAMS software enables to solve the objective functions in a few seconds. Subsequently, the proposed model with obtained empirical parameters can be conveniently applied to simulate the gas transport in full flow spectrum. Comparing with simulation methods by deterministically or probabilistically solving Newton's laws of motion (Frenkel et al., 2001), the developed analytical model is more efficient and practical when dealing with the same scale problem.

The calculated and collected normalized viscous fluxes have been plotted against mean pressures as can be seen in Figure 3.4. It can be found that the newly developed model is able to accurately reproduce the reference data with an average error of 0.75% (Tison, 1993), 7.06% (Yamaguchi et al., 2011), 6.79% (Ewart et al., 2007), 2.11% (Landry et al., 2016), and 5.39% (Loyalka and Hamoodi, 1990), respectively. The collected normalized viscous molar fluxes mainly fall into the slip flow regime ($0.015 \le Kn \le 0.01$) and early transition flow regime ($0.13 \le Kn \le 0.52$). All the curves are inclined to converge to the unity, implying that the flow behavior gradually shifts from transition flow/slip flow to pure continuum flow as the mean pressure increases. Figure 3.4 exhibits normalized Knudsen diffusion fluxes simulated by the newly developed model and collected from Loyalka and Hamoodi (1990). As can be seen, the normalized Knudsen diffusion flux gradually decreases from a constant value (i.e., theoretical Knudsen diffusion limit) in the Knudsen diffusion regime ($12.24 \le Kn \le 100.00$). Subsequently, a concave emerges on the curve in early transition flow regime ($0.45 \le Kn \le 1.30$) and the normalized flux increases with the mean pressure in a quasi-exponential manner within the slip flow regime ($0.06 \le Kn \le 0.10$). Figure 3.5 compares the calculated and collected apparent permeability with the pressure by considering the surface

diffusion. The reference data reflects the methane flow in the organic nanopore ranging from 5.0 to 50.0 MPa which covers the shale gas reservoir condition. It can be found that the developed model can provide a good prediction with an error of 11.91%. In general, considering Figures 3.4-3.6, the new unified gas transport model proposed in this work can reproduce both experimental and the numerical data with an overall error of 5.67%.

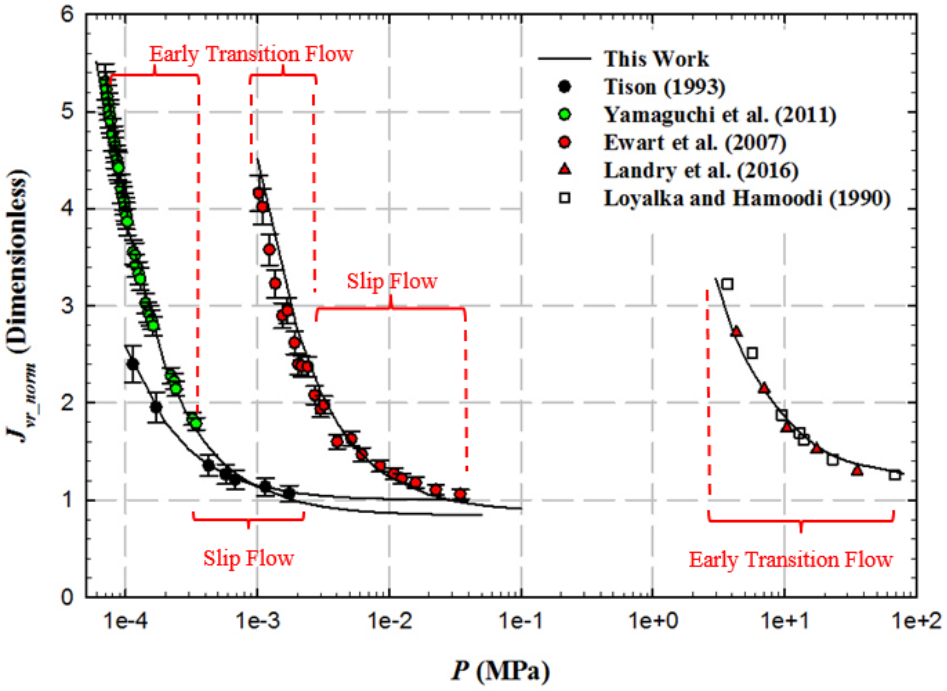

Figure 3.4: Calculated and collected normalized viscous flux versus mean pressure.

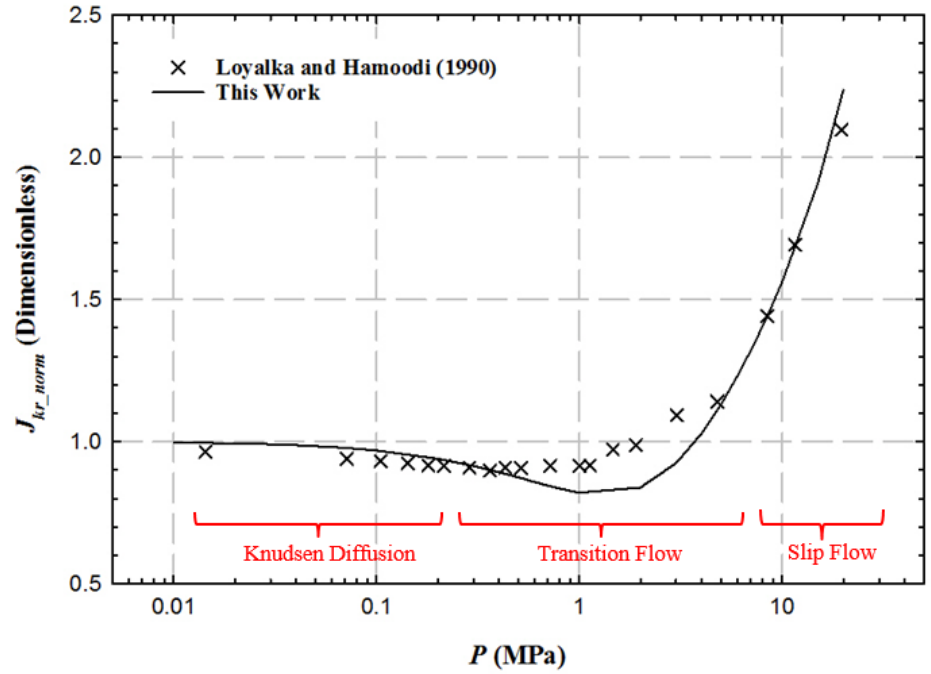

Figure 3.5: Calculated and collected normalized Knudsen diffusion flux versus mean pressure.

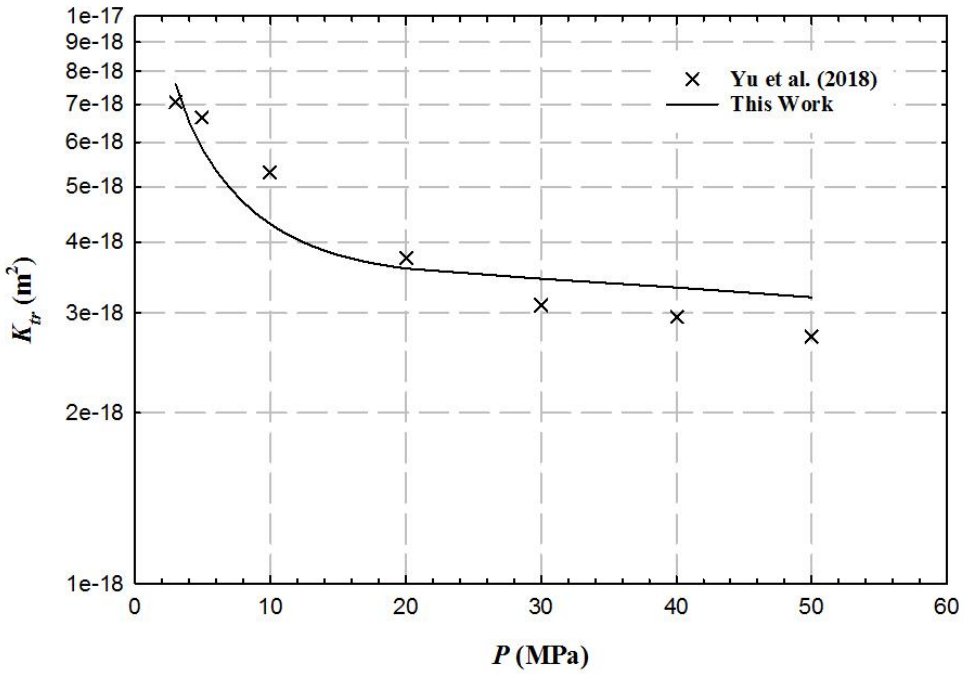

Figure 3.6: Calculated and collected normalized Knudsen diffusion flux versus mean pressure.

As aforementioned, w_v and w_k are assigned as weights for the viscous flow and Knudsen diffusion, respectively. According to Eqs. 3.36 and 3.37, Figure 3.7 plots the w_v and w_k against the Knudsen number. It can be seen that w_v keeps constant as 1.0 in continuum flow regime ($Kn \le 0.001$) and gradually increases in the slip flow regime ($0.001 \le Kn \le 0.1$) due to the slip flow mechanism, whereas $w_k = 0$ because no Knudsen diffusion should exist in the viscous flow region. Such observation is consistent with the characterizations of typical flow regimes in literatures (Javadpour, 2007; Civan, 2010; Akkutlu and Fathi, 2012) where only continuum flow mechanism is in presence in the continuum flow regime ($Kn \le 0.001$) and the continuum flow is enhanced (i.e., $w_v > 1$) in the slip flow resulting an increased flux. Figure 3.7 also shows that the weight of the viscous flow keeps increasing in the early transition regime ($0.1 < Kn < 0.35$) and then starts to decrease while the weight of the Knudsen diffusion progressively increases to the unity in transition flow ($0.10 \le Kn \le 10.00$) and Knudsen diffusion ($Kn > 10.00$) regimes. Note that the summation of two weights is not equal to the unity because weights derived from the kinetic model are completely controlled by the Knudsen number and mutually independent. The variation of two weights conditioned to the Knudsen number is rational and coincide with the widely-accepted classification of flow regimes (Schaaf and Chambre, 1961). It is also a superiority of this innovative work because such way allows the model to cover the full flow regime.

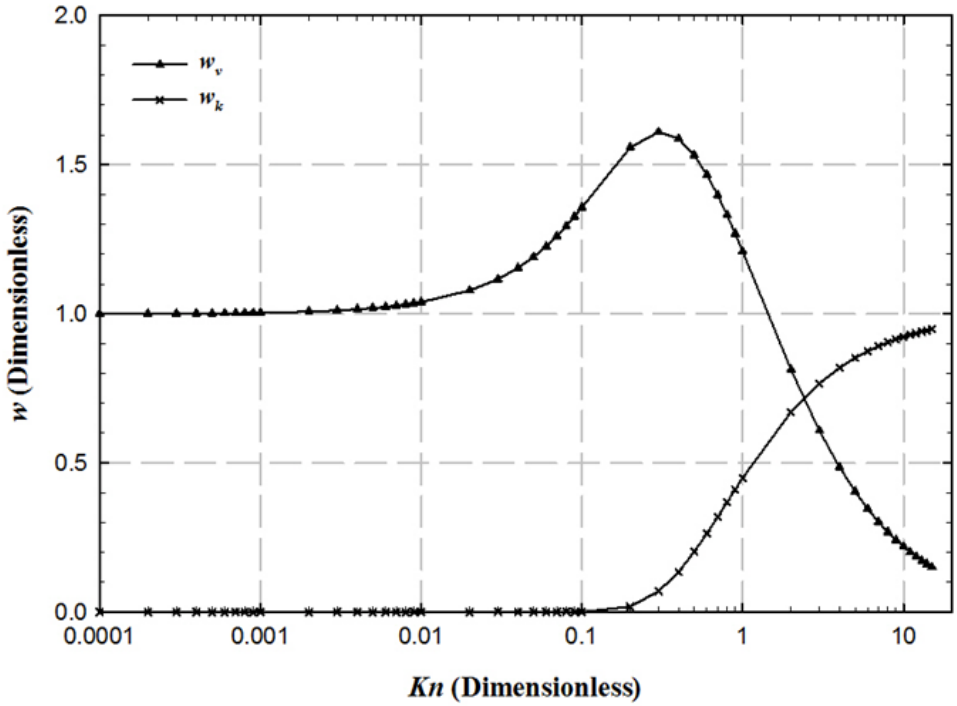

Figure 3.7: Calculated Weights of the viscous flux and Knudsen diffusion flux with respect to Knudsen number.

3.4.2 Model Comparisons

The newly developed model is also compared with five well-recognized analytical models (Ertekin et al., 1986; Liu et al., 2002; Bravo, 2007; Javadpour, 2009; and Veltzke and Thöming, 2012) to further demonstrate the performance of this work in terms of reproducing the normalized viscous flux and normalized Knudsen diffusion flux collected from Tison (1993) and Loyalka and Hamoodi (1990). As can be seen in Figure 3.8, Liu et al. (2002) and Bravo (2007) significantly underestimate the normalized viscous molar flux while other models overestimate it. In contrast, this work is capable to match the reference data with the minimum deviation. Figure 3.9 presents the comparisons of the normalized Knudsen diffusion. Although most of the analytical models can follow the tendency of reference data, the model of Liu et al. (2002) has an erroneous trend when the flow reaches the transition flow regime ($Kn \geq 0.10$). This is attributed to the fact that the weight

for Knudsen diffusion is negative, implying there is no Knudsen diffusion when Knudsen number is larger than or equal to 1 in Liu's model. In addition, Ertekin et al. (1986), Bravo (2007), Javadpour (2009), and Veltzke and Thöming (2012) overestimate the data in the transition flow regime ($1.00 \le Kn \le 10.00$). Comparatively, this work can more accurately match the tendency of the reference data. Moreover, only Bravo (2007), Veltzke and Thöming (2012), and the new unified gas transport model generally converge to 1.0, which is reasonable according to the theoretical Knudsen diffusion limit. Given that the mean pressure is reduced, Knudsen (1909) has stated that the gaseous mass flux through capillaries decreases due to the decreased gas density but reaches a minimum value when the Knudsen number is about unity. Such a minimum point is called Knudsen's minimum which is resulted from the appearance of transition flow. It can be found from Figure 3.9 that only the newly proposed model is capable to accurately present Knudsen's minimum in comparison to other models. In other words, the newly developed model can reproduce both viscous and Knudsen diffusion fluxes with Kn widely ranging from 0.01 to 100. Furthermore, model comparisons have demonstrated that this work has superior accuracy in both slip and transition flow regimes compared to Bravo's model. The inferior accuracy of Bravo's model in transition flow regime may result from the linear velocity profile assumption which is against the reality.

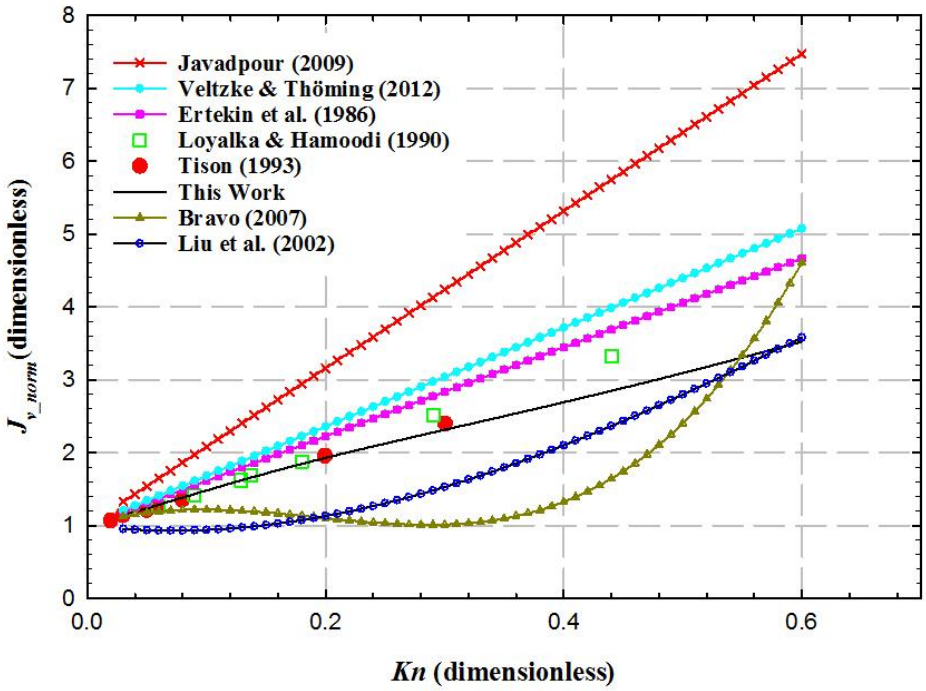

Figure 3.8: Comparison of the normalized viscous molar flux between the newly proposed model and other analytical models.

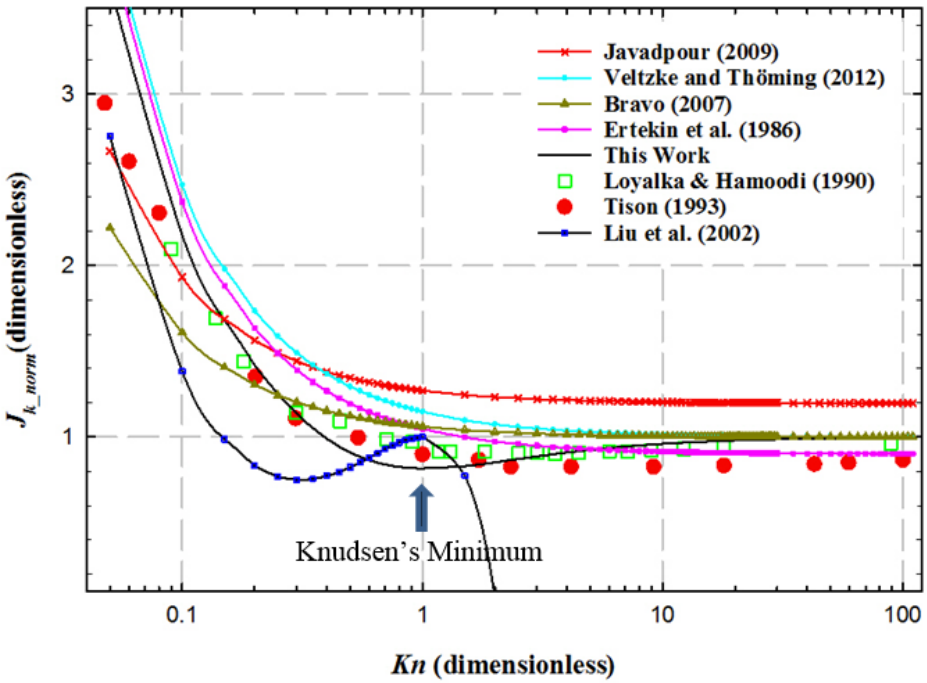

Figure 3.9: Comparison of the normalized Knudsen diffusion between the newly proposed model and analytical models.

3.4.3 Real Gas and Ideal Gas Deviation Analysis

Viscosity of real gas changes with pressure rather than a constant for the ideal gas analytical models. Figure 3.10 expresses the real gas viscosity (i.e., η_r) of methane at reservoir temperatures of 323 K, 373 K, and 423 K with the mean pressure, where the ideal gas viscosity (i.e., η) is also plotted for comparison. It shows that the real gas viscosity can increase distinctly from 1.18×10^{-5} to 3.70×10^{-5} Pa·s when the mean pressure increases from 5.0 to 50.0 MPa at temperature of 323 K while the ideal gas viscosity is 1.18×10^{-5} Pa·s. In addition, it is shown that gas viscosity increases with the temperature at relatively low pressures below 18 MPa while the viscosity decreases with the temperature at high pressures above 18 MPa. Figure 3.11 presents the real gas compressibility factor of methane versus the mean pressure at reservoir temperatures of 323 K, 373 K, and 423 K. It is seen that there are substantial changes in compressibility factor for methane in the low-temperature and high-pressure region. Furthermore, the compressibility factor follows a non-monotonic trend with the pressure.

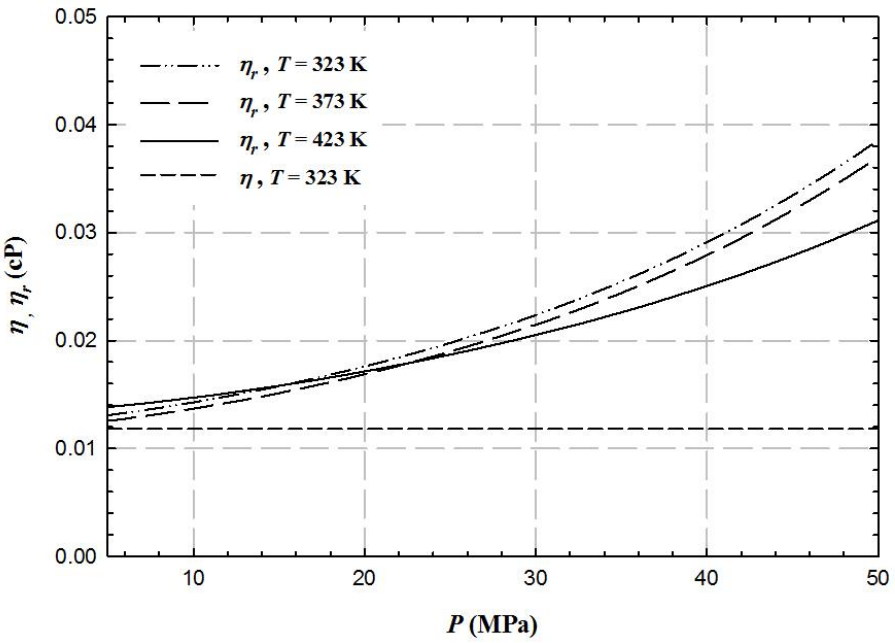

Figure 3.10: Comparison of methane viscosity between ideal and real gas using Sutton's model (2007).

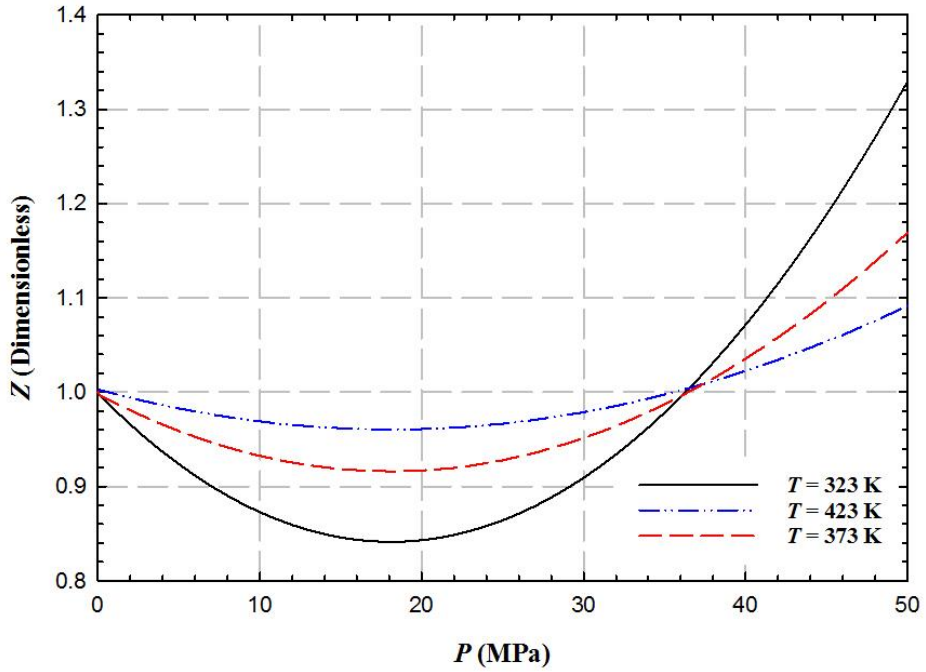

Figure 3: Compressibility factor of methane versus mean reservoir pressure.

Figure 3.12 exhibits the Knudsen number evolution with pressure in various pore sizes for ideal and real methane gas under reservoir conditions (e.g., $5 \le P \le 50$ MPa, $T = 323$ K), respectively. It is seen that the Knudsen number at same pressures decreases as the pore size increases. The Knudsen number of methane keeps decreasing with the pressure. The real gas Knudsen number starts distinctly deviating from the ideal gas Knudsen number at the pressure of 20.0 MPa and the deviation degree is gradually increasing. This is because the real gas effect at high pressures (>20.0 MPa) increases the viscosity which dominantly increases molecular mean free path. According to the definition of the Knudsen number (i.e., $Kn = \lambda / R_0$), the increasing mean free path leads to the increment of Knudsen number. In addition, it is observed that the transition flow becomes more significant compared with that of the viscous flow under a relatively low-pressure condition (≤ 20.0 MPa), provided that the pore diameter is less than 5 nm.

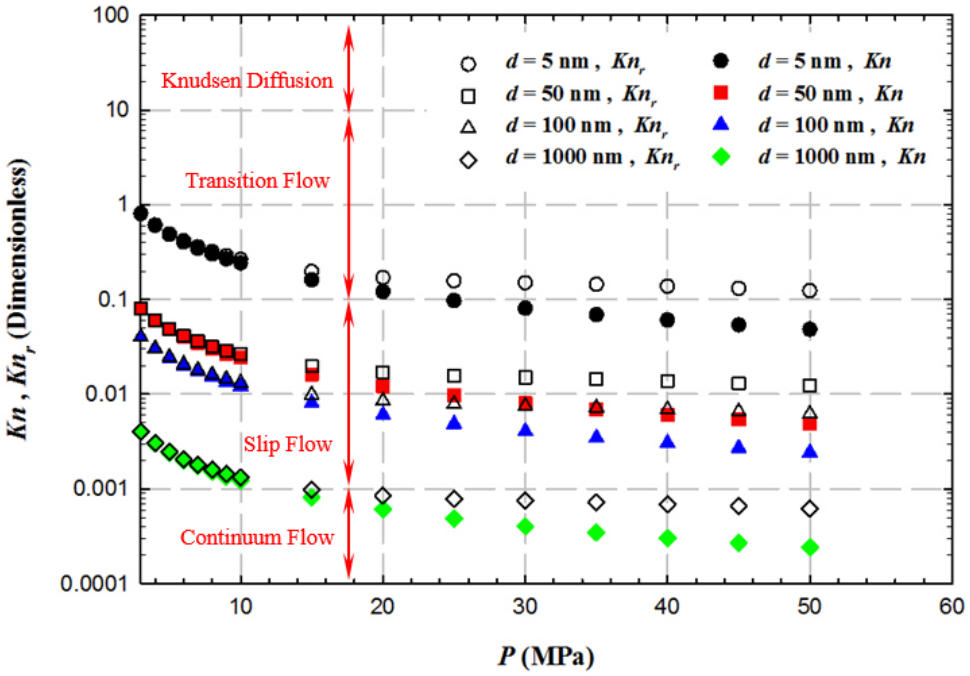

Figure 3.12: Knudsen number evolution with mean reservoir pressure (empty symbols: real gas; solid symbols: ideal gas).

Figure 3.13(*a*) shows the deviation of total molar flux in inorganic pores (i.e., without surface diffusion) between real gas and ideal gas at different diameters as pressure changes from 0.1 to 50.0 MPa (see Eq. 3.39). It can be found that the real gas effect exerts limited influences on the flux calculated by ideal gas model under low-pressure conditions ($\lesssim$15.0 MPa), yielding the deviation within 10.0%. This is mainly because the gas viscosity at low pressures is close to that under ideal gas condition. It is worthwhile noting that a peak can be found on the curve at low pressures for all pore sizes mainly due to the effect of compressibility factor on molar fluxes. However, the real gas effect can reduce the molar flux calculated from the ideal gas model up to 66.0% at 50.0 MPa in the pore size of 200 nm. It is mainly due to the fact that the increased viscosity at high pressures dominantly counteracts the flux. Furthermore, the deviation is aggravated as pore size increases at high pressures because the larger pores are commonly

dominated by the viscous flow regime, in which the viscosity has more impact over the flux. Figure 3.13(*b*) shows the deviation of total molar flux in organic pores (i.e., with surface diffusion) between real gas and ideal gas at different diameters as pressure changes from 0.1 to 50.0 MPa. In general, the deviation has the similar performance as that in the inorganic pores. The difference between organic and inorganic pores is insignificant ($\leq$5.0%) and can be ignored.

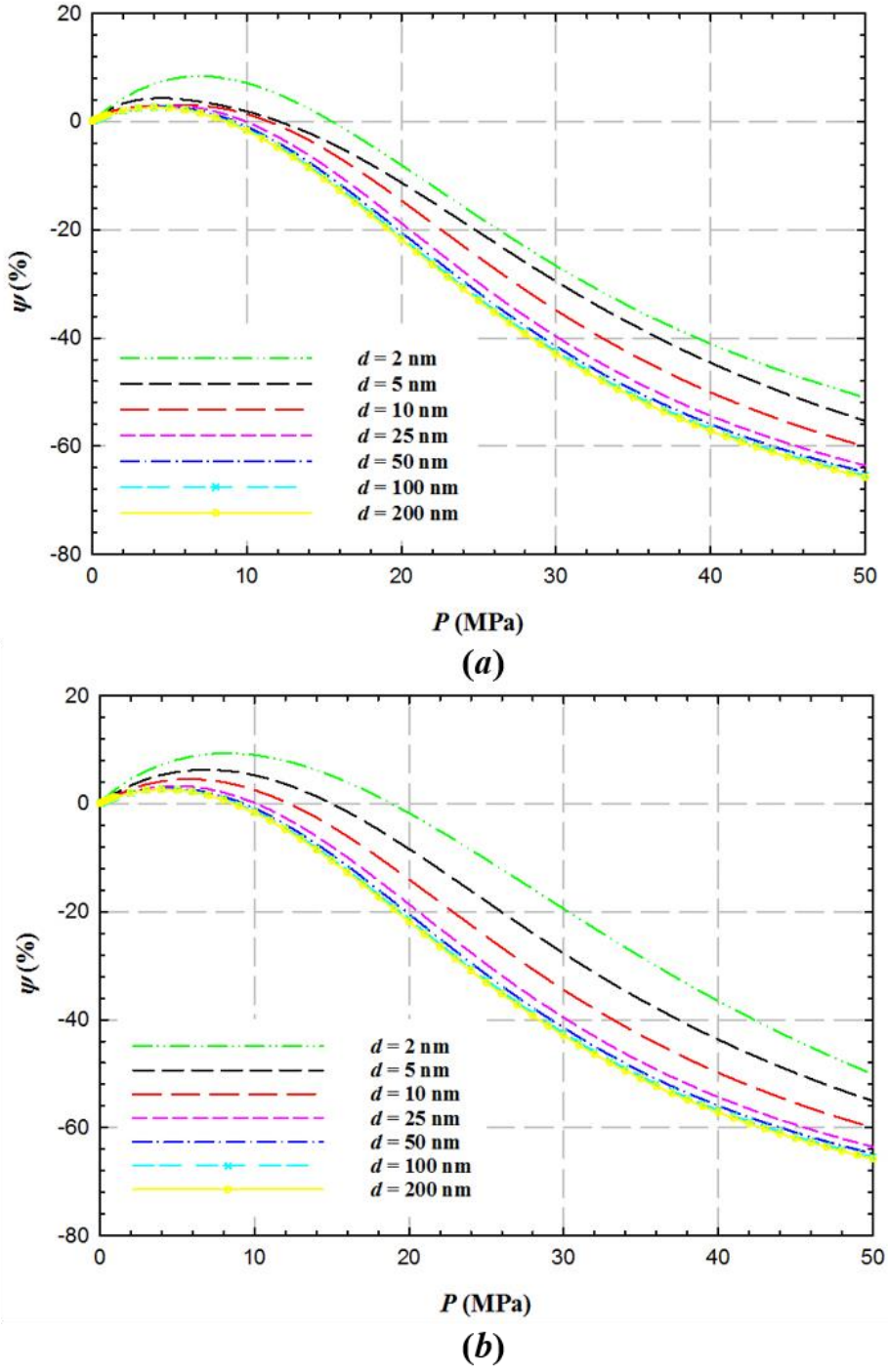

Figure 3.13: Deviation between real gas and ideal gas total fluxes in inorganic nanopores (*a*) and organic nanopores (*b*) under reservoir pressures.

3.4.4 Sensitivity Analyses of Apparent Permeability

The sensitivity of effective apparent permeability to various parameters has been analyzed for methane in details in this section. The parameters used in the sensitivity analyses have been listed in Table 3.4.

Table 3.4: Summary of parameters used in sensitivity analyses

Parameters	Symbol	Unit	Values
Fitting parameter	α_1	dimensionless	4.0
Fitting parameter	β	dimensionless	0.4
Chemical confinement parameter	ξ	dimensionless	0.46
Velocity direction heterogeneity parameter	κ	dimensionless	0.91
Slip coefficient	s	dimensionless	-1
Reservoir temperature	T	K	323
Fractal dimension of the pore surface	D_f	dimensionless	2.0
Universal gas constant	R	J/(mol·K)	8.314
Nominal methane molecule size	d_m	nm	0.38
Methane molar mass	M	kg/mol	0.016
Methane critical pressure	P_c	Pa	4.60×10^6
Methane critical temperature	T_c	K	190.6
Average porosity	ϕ	dimensionless	0.05
Average tortuosity	τ	dimensionless	4.3
Langmuir Pressure	P_L	Pa	13.8×10^6
Langmuir Volume	V_L	m^3/kg	0.00312
Surface diffusivity coefficient	D_s	m^2/s	8.8×10^{-6}
Ratio of organic grain to the total grain volume	ε_k	dimensionless	0.676
Shale grain density	ρ_{grain}	kg/m^3	2659.065
Methane density at standard condition	ρ_{STG}	kg/m3	0.641

(1) Pore Size and Roughness

Figure 3.14 plots the effective apparent permeability versus pressure in both inorganic and organic pores with pore sizes of 2, 5, 10, 25, 50, and 100 nm. In general, the apparent permeability decreases with pressure in the pore size smaller than 100 nm and such a decline is more distinct as

pore size shrinks, particularly in organic pores. At a given pore size of 2 nm, the apparent permeability can be significantly reduced from 1.44×10^{-2} to 1.03×10^{-3} μD in the inorganic pore and from 4.21×10^{-2} to 9.76×10^{-4} μD in the organic pore when the pressure increases from 3.0 to 50.0 MPa. Moreover, it is seen that the apparent permeability varies in different pore sizes. However, the apparent permeability rarely changes with pressure in the pore size larger than 100 nm. This is mainly because the flow regime has shifted to the continuum flow where the apparent permeability is approaching the intrinsic permeability of the porous media. In addition, the apparent permeability in organic pores is higher than that in inorganic pores up to 2.77×10^{-2} μD in pore size of 2 nm, which is contributed by the surface diffusion. However, when the pore size is larger than 10 nm, the contribution of surface diffusion can be ignored. In Figure 3.15, the effective apparent permeability in organic nanopores with pore sizes of 2, 10, and 25 nm is plotted at three fractal dimensions of 2.0, 2.2, and 2.5. The roughness coefficient (i.e., $\delta^{(D_f-2)}$) increases with the fractal dimension (i.e., D_f). It can be found that the apparent permeability decreases from 6.60×10^{-2} to 5.59×10^{-2} μD when the fractal dimension increases from 2.0 to 2.5 at 3.0 MPa in the pore size of 2 nm. Such a difference reduces as pore size increases. Also, as can be seen in the inset graph in Figure 3.15, the apparent permeability is independent with the fractal dimension in the pore size larger than 10 nm when the pressure is greater than 15.0 MPa.

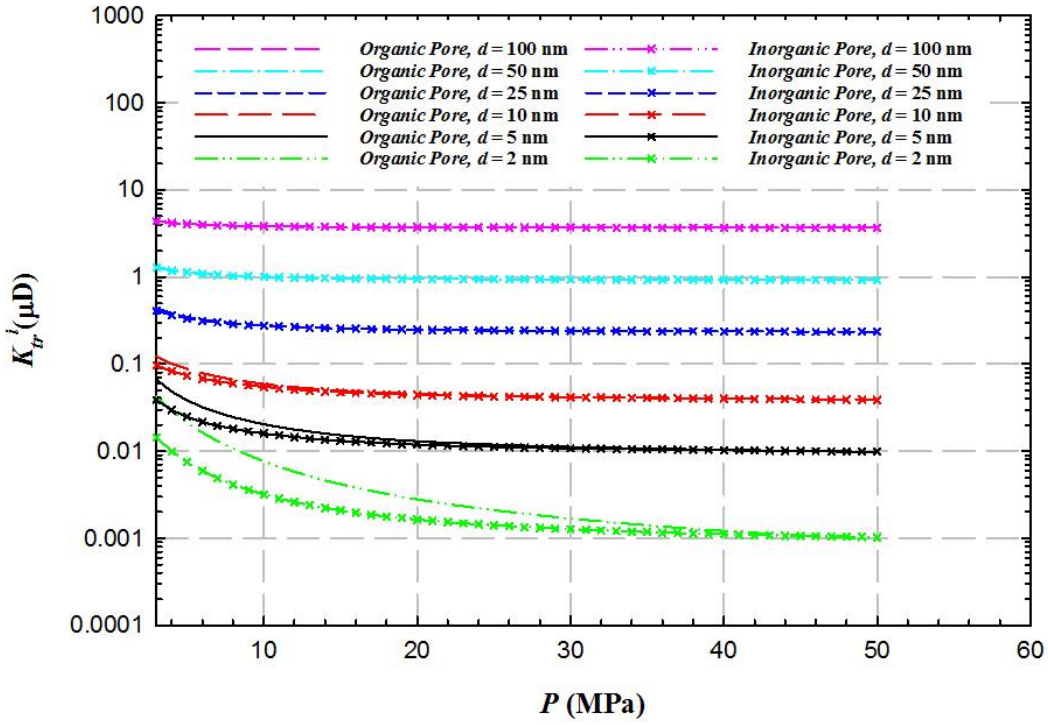

Figure 3.14: Effective apparent permeability under reservoir pressures in inorganic and organic pores with different sizes.

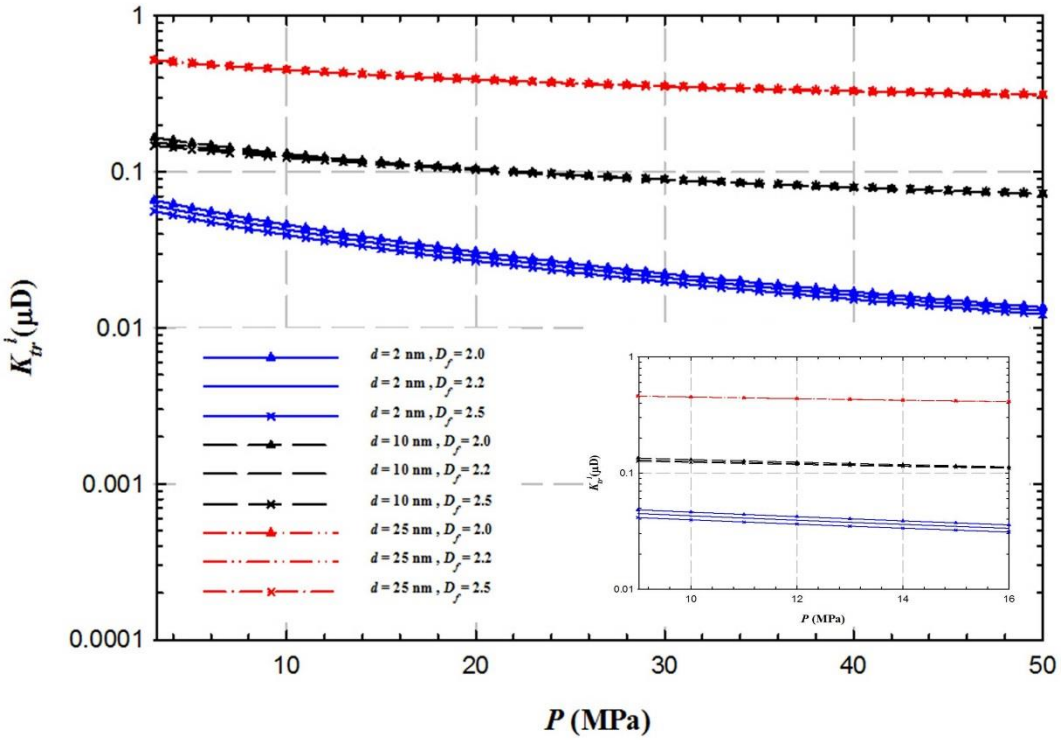

Figure 3.15: Comparison of the effective apparent permeability under reservoir pressures with different fractal dimensions.

(2) Contributions of Flow Mechanisms

Figures 3.16-3.19 present the contributions of viscous flow, Knudsen diffusion, and surface diffusion to the apparent permeability in 2, 5, 10, and 25 nm under typical shale reservoir conditions, respectively. It is found that as pressure and pore size increases, the contribution of viscous flow increases and accordingly the contribution of the Knudsen diffusion decreases. This is mainly because the flow regime shifts toward the viscous flow regime as pressure and pore size increase (see Figure 3.12). As seen in Figure 3.16, when pore size is 2 nm and pressure is above 5 MPa, the viscous flow contributes from 14.49% up to 99.95%. Meanwhile, the contribution of Knudsen diffusion drops from 20.97% at the pressure of 3.0 MPa to 4.63% at the pressure of 35.0 MPa. As seen in Figure 3.19, when pore size is 25 nm, the viscous flow completely dominates the

apparent permeability across entire reservoir pressure ranges. In contrast, as seen in Figure 3.17, the contribution of Knudsen diffusion in pore size of 5 nm is below 6.00% when the pressure is above 6.0 MPa. Hence, the viscous flow cannot be neglected at any pore sizes under reservoir conditions while the Knudsen diffusion is only important in the pore size below 2 nm and pressure less than 35.0 MPa.

In addition, the gas apparent permeability of surface diffusion decreases as pressure and pore size increases. This is attributed to the fact that the specific surface area decreases with the pore size resulting in less adsorption and surface diffusion in the pore. As can be seen in Figures 3.16 and 3.17, the surface diffusion greatly contributes to apparent permeability accounting for 64.54% to 50.09% in 2 nm and 35.54% to 13.68% in 10 nm from 5.0 to 15.0 MPa, respectively. However, the surface diffusion contribution is below 4.23% in 10 nm pores when the pressure is above 15 MPa (see Figure 3.18) and lower than 3.90% in 25 nm pores across entire reservoir pressure range (see Figure 3.19), which can be neglected. Hence, when the pore size is below 10 nm and the pressure less than 15 MPa, the contribution of surface diffusion cannot be ignored.

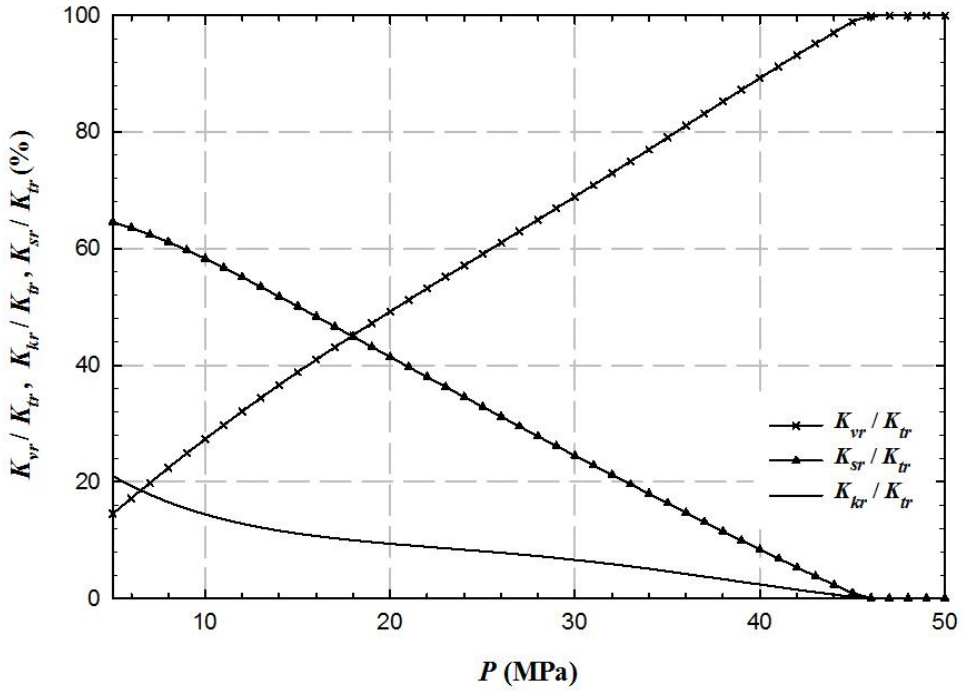

Figure 3.16: Apparent permeability contributions from viscous flow, Knudsen diffusion and surface diffusion with respect to reservoir pressures in 2 nm organic nanopores.

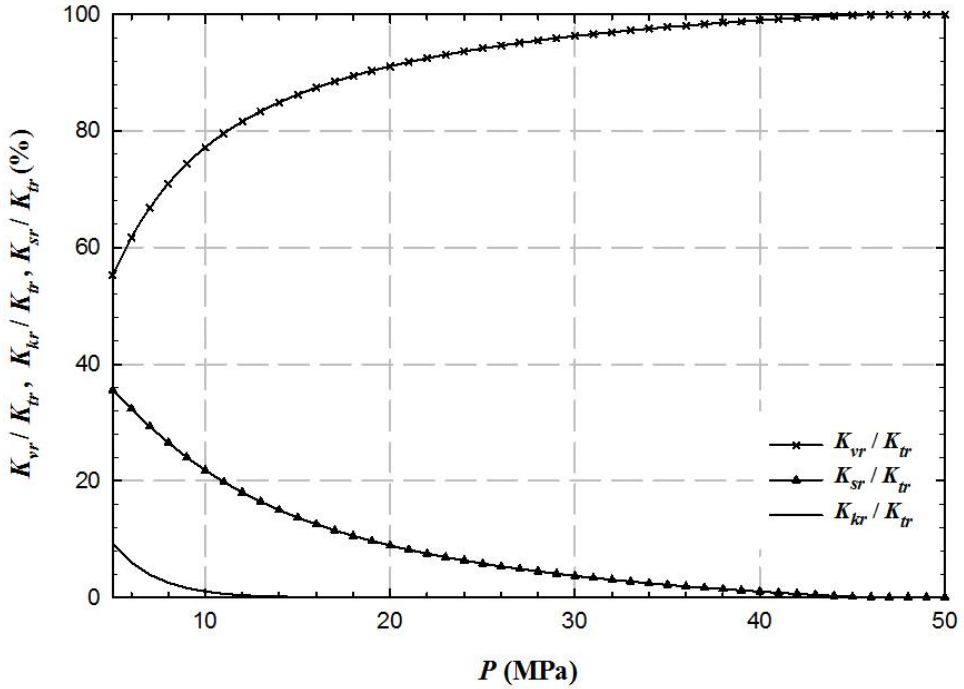

Figure 3.17: Apparent permeability contributions from viscous flow, Knudsen diffusion and surface diffusion with respect to reservoir pressures in 5 nm organic nanopores.

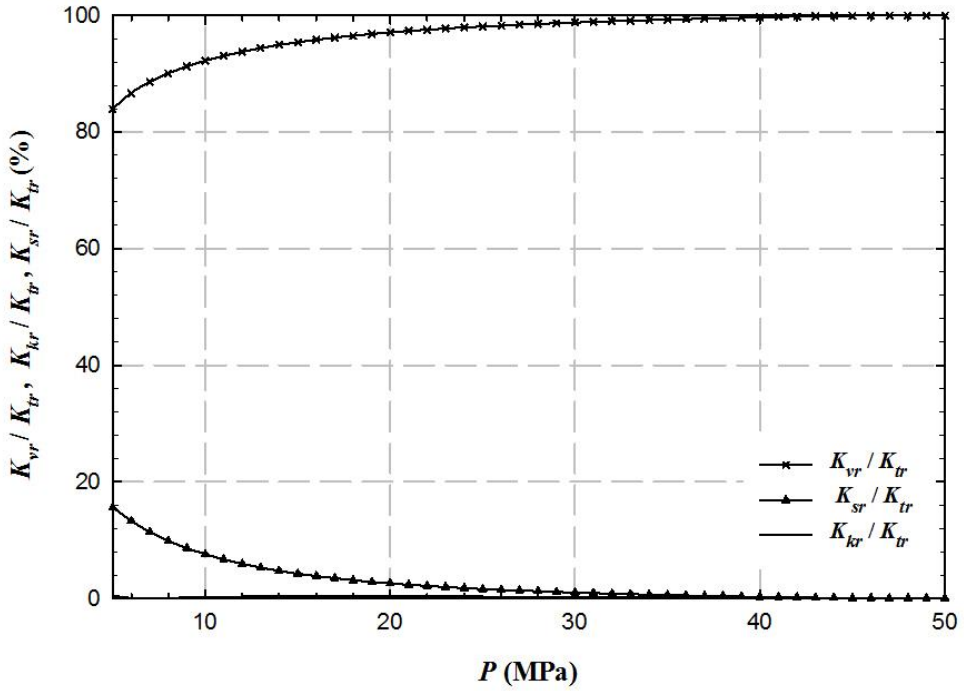

Figure 3.18: Apparent permeability contributions from viscous flow, Knudsen diffusion and surface diffusion with respect to reservoir pressures in 10 nm organic nanopores.

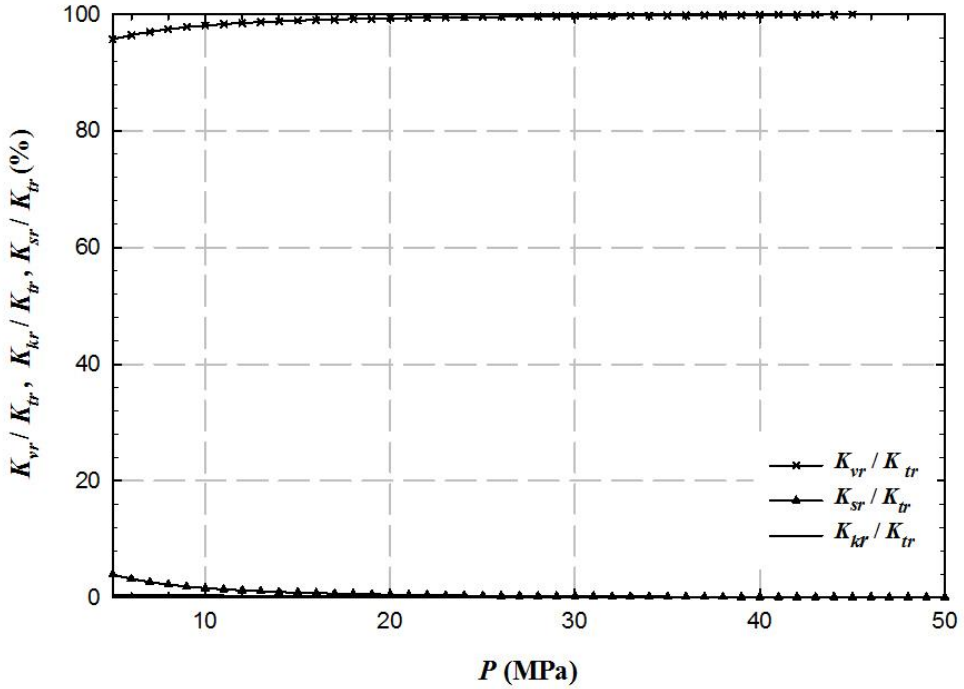

Figure 3.19: Apparent permeability contributions from viscous flow, Knudsen diffusion and surface diffusion with respect to reservoir pressures in 25 nm organic nanopores.

3.5 Summary

The new analytical model considering viscous flow, Knudsen diffusion, and surface diffusion has been successfully developed to compute the gas transport over the full flow regime in both organic and inorganic pores where the virtual boundary between the viscous flow and Knudsen diffusion zones is firstly determined based on an analytical molecular kinetics approach. The Knudsen number of real gas flow increasingly deviates from that of ideal gas flow due to the impact of real gas effect at high pressures (≥ 20.0 MPa). Moreover, the increasing viscosity due to the real gas effect can reduce the total molar flux in the inorganic pores up to 66.0% under typical shale gas reservoir condition. The apparent permeability decreases with pressure in the pore size smaller than 100 nm and such a decline is more distinct as pore size shrinks. The sensitivity analyses have demonstrated that the pore size has the greatest impact on the apparent permeability. It is also found that the viscous flow mechanism cannot be neglected at any pore sizes under reservoir conditions while the Knudsen diffusion is important in the pore size below 2 nm and pressure less than 35.0 MPa. The contribution of surface diffusion cannot be ignored when the pore size is below 10 nm and the pressure less than 15 MPa.

CHAPTER 4: GAS TRANSPORT IN SHALE MATRIX COUPLING MULTILAYER ADSORPTION AND PORE-CONFINEMENT EFFECT

4.1 Introduction

Accurate prediction of gas transport in shale formations mainly consisting of micro- and nano-scale pores is a great challenge since most existing models only consider monolayer adsorption and the underlying multi-physics are either partially or completely overlooked. In this work, we have proposed a comprehensive gas transport model integrating multiple physical mechanisms in nanopores, especially the multilayer adsorption and pore confinement effect. The new analytical model is developed based on Bravo layer-sequence-model and then upscaled using an Effective Medium Approximation (EMA) method, where the generalized Brunauer-Emmett-Teller (BET) model, the modified Peng-Robinson EoS model, and the Sutton's model are innovatively incorporated. The newly developed model has been successfully validated against simulation and experimental results with the assistance of an efficient iterative ensemble smoother (ES) algorithm. It is observed that the pore confinement effect is of importance when the pore size is smaller than 50 nm. The increase of gas viscosity due to the real gas effect is significant under reservoir conditions. The apparent permeability is found to increase greatly as the adsorption layer number increases, implying that the application of Langmuir model in existing gas transport models may substantially underestimate it. Given inorganic nanopores, the viscous flow is important at any pore sizes and the Knudsen diffusion plays a role in the pores that are less than 5 nm under reservoir conditions. As for organic nanopores, the contribution of surface diffusion is tangible when the pore size is below 150 nm and the Knudsen diffusion is negligible under high pressures.

4.2 Mathematical Formulation

4.2.1 Conceptual Model and Discrete Density Profile

A conceptual model is developed as illustrated in Figure 4.1. The space in the single straight nanocapillary can be separated by the effective radius R_e into two flow zones, which are a free gas flow zone in the central space (i.e., the space within the red cylindrical capillary) and a surface diffusion zone in the outer annular space (i.e., the space constrained by the effective radius R_e and capillary radius R_0). Note that the volume in the outer annular zone is occupied by multilayer adsorbed gas, of which the amount is significantly underestimated in analytical calculations with the existing models due to the monolayer adsorption assumption. Moreover, the monolayer-adsorption assumption in current models has typically limited the discussion of density fluctuations near the wall arising from abundant adsorption which is shown in Figure 4.2 (Didar and Akkutlu, 2013). Figure 4.2 presents the discrete density profile of methane simulated by molecular dynamics in nanopores with two different pore sizes (Ambrose et al., 2012). As can be seen in Figure 4.2, there are (a) four adsorption layers and (b) two adsorption layers in two density profiles, respectively. The density distribution in each surface diffusion zone is non-uniform where the density decreases from a high value on the wall to a low value near the pore-center. The density of uppermost adsorption layers gradually approaches to the density of free gas flow until the equilibrium is reached.

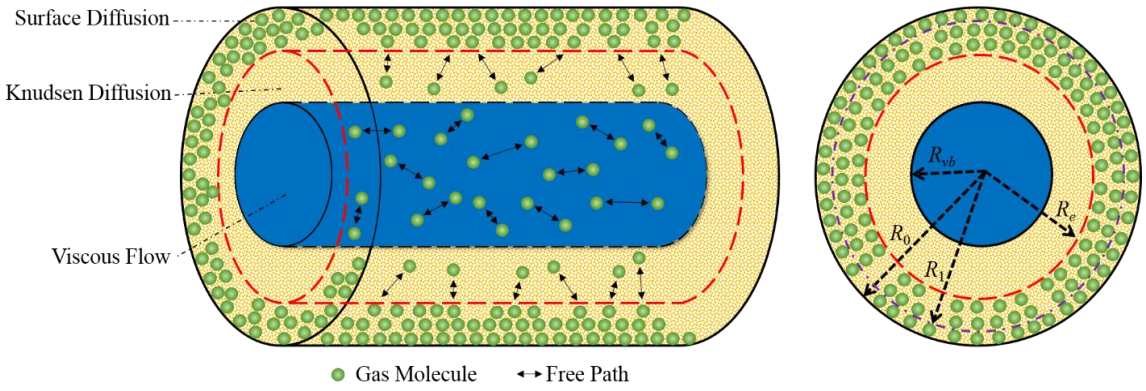

Figure 4.1: Schematic diagram of the sequence-layer model of a straight capillary (Blue central zone – viscous flow; Yellow middle annular zone – Knudsen diffusion; Outer annular zone –multi-layer adsorption and surface diffusion; – Capillary radius; – Radius corresponding to the first layer adsorption on the wall; – Effective radius corresponding to the last layer in multi-layer adsorption; – Radius of virtual boundary).

As illustrated in Figure 4.2, the uniform density distribution in free gas flow zone is hardly affected by the density fluctuations in the surface diffusion zone (Ambrose et al., 2012). The free gas flow zone in the central space can be further divided by the virtual boundary R_{vb} into viscous flow zone highlighted by blue color and Knudsen diffusion zone which is highlighted by yellow color and constrained by virtual boundary R_{vb} and effective radius R_e (See Figure 4.1). Such layer-sequence structure is developed based on the molecule-collision-probability assumption that viscous flow is represented by intermolecular collisions which are dominant in the central space while Knudsen diffusion is represented by molecule-wall collisions which are dominant in the middle annular space (Chai and Li, 2017; Chai et al, 2018; Zheng et al., 2019). In addition, the description of density distribution in the layer-sequence model is consistent with the result of molecular dynamics (Ambrose et al., 2012) which shows that the density distribution is uniform in the free gas flow zone (i.e., central and middle annular zones), whereas the density distribution in adsorption layer is non-uniform (see Figure 4.2). Chai et al. (2019a) have indicated that the virtual boundary, R_{vb}, can be determined as

$$R_{vb} = \frac{1}{\sqrt{\kappa}} R_e \sqrt{1 - \exp\left(-\xi \frac{1}{Kn}\right)} \tag{4.1}$$

where κ is an empirical coefficient indicating the heterogeneity of velocity directions, ξ is an empirical coefficient describing the chemical confinement effect due to interactions between molecules and pore-wall, Kn is local Knudsen number defined as the ratio of molecular mean free path over local characteristic length (i.e., λ / R_e) (Bird, 1994). Note that R_e is equal to R_0 in nanopores where there is adsorption scarcity such as inorganic pores. It has been shown that the determination of virtual boundary is crucial in assigning the contribution of viscous flow and Knudsen diffusion in the layer-sequence model.

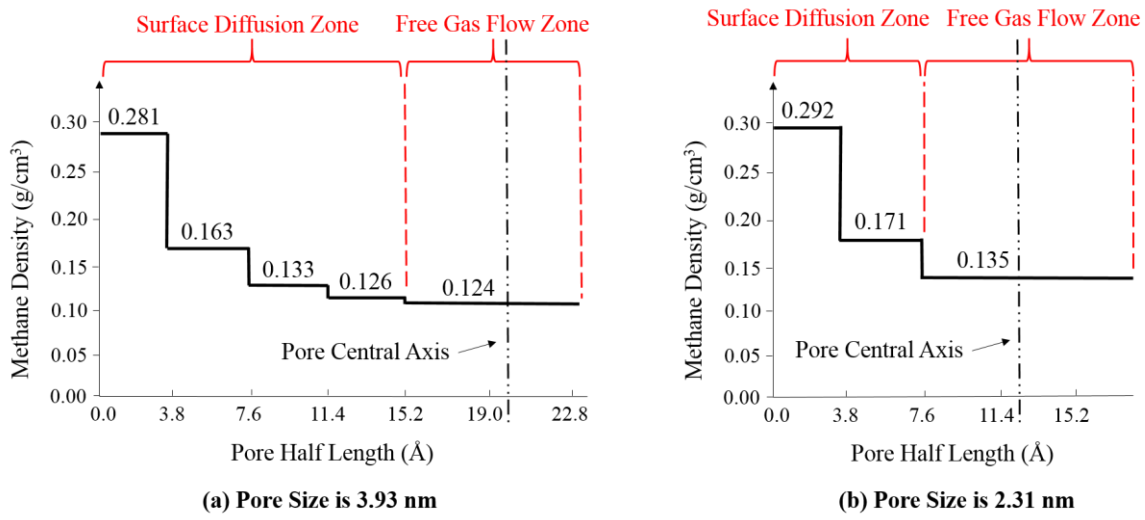

Figure 4.2: Discrete-density profiles for methane at 176 ºF in nanopores with size of (a) 3.93 nm and (b) 2.31 nm are identified under the pressure of 3043 psi from molecular dynamics simulation (Ambrose et al., 2012). Discrete density corresponds to adsorption-layer density across the pore.

Wasaki and Akkutlu (2015) have considered the multilayer adsorption and mathematically simplified the multilayer adsorption to monolayer adsorption so that Langmuir isotherm model can be applied accordingly. Nonetheless, such treatment is valid only if the pore size is much larger

than the multilayer thickness. In the case of small pore size (e.g., <10 nm), the available space and molar flux for free gas flow will be overestimated if the multilayer adsorption is simplified to monolayer adsorption. In contrast to the Langmuir isotherm model, the BET isotherm model is adopted in this work because it is a generalization of the Langmuir model to multiple adsorbed layers (Yu et al., 2016). As shown in Figure 4.1, the thickness of multiple layers is constrained by capillary radius R_0 and the effective radius R_e which corresponds to the last layer from the wall in multilayer adsorption. Brunauer et al. (1938) has pointed out that it is not required for a layer to be completely covered by adsorbents before an upper layer starts to form (See Figure 4.3a). Hence, some upper adsorption layers which contains few adsorbed molecules may not contribute to the surface diffusion in adsorption zone. On the contrary, these upper layers interact with free gas molecules and contribute to the free gas flow. Therefore, the actual adsorption layers (See Figure 4.3a) can be transformed to hypothetical adsorption layers (See Figure 4.3b) for the easiness of theoretical calculations. Effective radius, R_e, can be determined as follows.

$$R_e = R_1 - \beta\left(N-1\right)d_m \tag{4.2}$$

where R_1 is radius corresponding to the first-layer adsorption on the wall, β is defined as equivalent fraction of adsorption layers which only contributes to the surface diffusion in adsorption zone, N is actual number of adsorbed layers in nanopores, d_m is molecular kinetic diameter. Wang and Marongiu-Porcu (2015) have claimed that the thickness of first layer adsorption may be different from the molecule diameter of adsorbed gas due to substantial influences of total organic content, clay minerals, maturity, and the specific surface. Accordingly, R_1 changes with the thickness of first layer. Thus, the radius corresponding to the first layer

adsorption, R_1, is determined as $R_1 = R_0 - \zeta d_m$ where ζ is an empirical thickness correction coefficient (Yu et al., 2016).

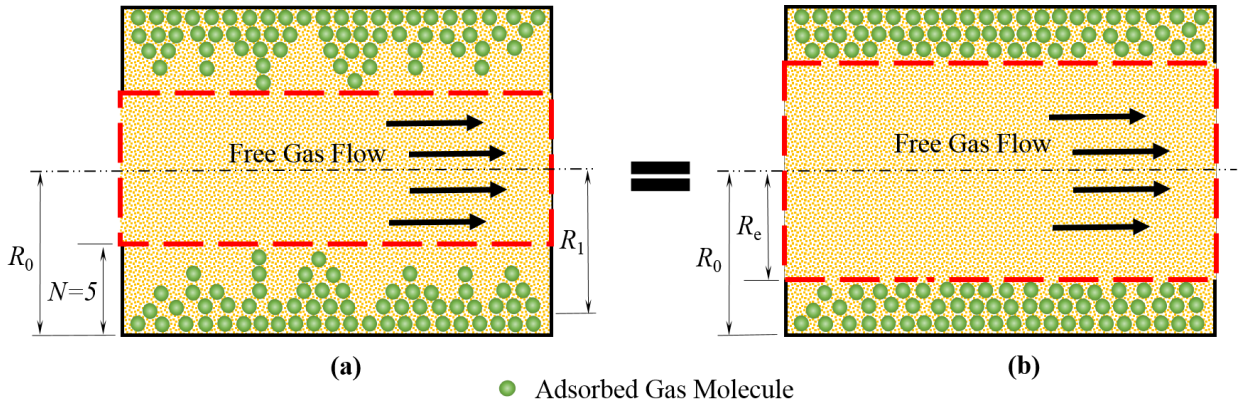

Figure 4.3: Schematic diagram of adsorption layers in nanopores. (a) shows five adsorption layers are in presence (i.e., *N*=5) where upper partially adsorbed layers are prone to interact with free gas molecues and contribute to free gas flow zone rather than adsorption zone. Hence, (a) can be simplified to (b) where adsorption layers are three hypothetical layers (i.e., *N*=3) only contributing to adsorption zone and is defined as effective radius from pore central axis to uppermost hypothetical adsorption layer.

4.2.2 Modeling of Ideal Gas Flow in Straight Capillary

(1) Adsorption/Desorption and Surface diffusion Characterization

The multilayer adsorption is typically characterized by BET isotherm model which assumes infinite number of adsorption layers. Nonetheless, Alnoaimi and Kovscek (2013) have indicated that number of adsorption layers in nanopores should be finite and a generalized BET isotherm model in terms of N adsorption layers is given as

$$V_{ad} = \frac{V_{\max} C_{BET} \dfrac{\bar{P}}{\bar{P}_0}}{1 - \dfrac{\bar{P}}{\bar{P}_0}} \left[\frac{1 - (N+1)\left(\dfrac{\bar{P}}{\bar{P}_0}\right)^N + N\left(\dfrac{\bar{P}}{\bar{P}_0}\right)^{(N+1)}}{1 + (C_{BET} - 1)\dfrac{\bar{P}}{\bar{P}_0} - C_{BET}\left(\dfrac{\bar{P}}{\bar{P}_0}\right)^{(N+1)}} \right] \tag{4.3}$$

where V_{ad} is volume of adsorbents per unit mass, $V_{\max}$ is BET maximum volume of first-layer adsorbents per unit mass when the wall is entirely covered by the first-layer adsorption, $\bar{P}$ is average pressure across the nanocapillary, $\bar{P}_0$ is gas saturation pressure, C_{BET} is equilibrium constant related to the net heat of adsorption (Yu et al., 2016). Note that Eq. 4.3 can be reduced to the Langmuir isotherm model and $V_{\max}$ is equivalent to the Langmuir volume when $N=1$, which implies that the generalized BET model is appropriate than the Langmuir isotherm model to characterize complicated adsorption/desorption process including monolayer and multilayer adsorption in nanopores. In addition, it is worth noting that the saturation pressure (i.e., $\bar{P}_0$) is unavailable because methane is in super-critical state in shale reservoir condition and saturation pressure loses its physical validity for super-critical gas. To overcome this difficulty, the saturation pressure is regarded as pseudo-saturation pressure for methane gas (Clarkson et al., 1997), and is calculated using the Antoine equation as follows (Hao et al., 2014).

$$\bar{P}_0 = \exp\left(7.7437 - \frac{1306.5485}{19.4362 + T}\right) \tag{4.4}$$

Fick's model has been widely accepted to characterize the surface diffusion due to its mathematical simplicity and physical validity (Xiong et al., 2012; Wasaki and Akkutlu, 2015; Song et al., 2016; Wu et al., 2016). It is also presumed that adsorption/desorption process can reach the equilibrium instantly to satisfy the requirement of BET isotherm model (Yu et al., 2016). Do et al. (2001) have indicated that the surface molar flux of adsorbed phases, J_s, can be expressed as

$$J_s = -D_s \nabla C_a \tag{4.5}$$

where D_s is surface diffusion coefficient, ∇C_a is concentration gradient of adsorbed gas. The concentration of adsorbed gas, C_a, can be calculated by the equation $C_a = \rho_m V_{ad} \rho_{sc} / M$, where ρ_m is shale matrix density, ρ_{sc} is gas density at standard condition, M is gas molar mass. Subsequently, the molar flux of apparent surface diffusion, J_s^A, can be rearranged by integrating Eqs. 4.3 and 4.5 as

$$J_s^A = \frac{J_s \pi \left(R_0^2 - R_e^2\right)}{\pi R_0^2} = -D_s \frac{\rho_m V_{\max} \rho_{sc}}{M} \frac{d\chi}{dP} \frac{\pi \left(R_0^2 - R_e^2\right)}{\pi R_0^2} \nabla P \tag{4.6}$$

where ∇P is pressure gradient along the nanocapillary, χ is defined as

$$\chi = \frac{V_{ad}}{V_{\max}} = \frac{C_{BET} \dfrac{\bar{P}}{\bar{P}_0}}{1 - \dfrac{\bar{P}}{\bar{P}_0}} \left[\frac{1 - (N+1)\left(\dfrac{\bar{P}}{\bar{P}_0}\right)^N + N\left(\dfrac{\bar{P}}{\bar{P}_0}\right)^{N+1}}{1 + (C_{BET} - 1)\dfrac{\bar{P}}{\bar{P}_0} - C_{BET}\left(\dfrac{\bar{P}}{\bar{P}_0}\right)^{N+1}} \right] \tag{4.7}$$

(2) Viscous Flow Characterization

Beskok and Karniadakis (1999) have proposed a local viscous flow velocity by replacing the no-slip boundary of Poiseuille velocity profile with a second-order slip velocity which is parameterized with local Knudsen number. The local viscous flow velocity is given by

$$U_v = -\frac{R_e^2}{4\mu} \left[1 - \left(\frac{r}{R_e}\right)^2 + \frac{2 - \sigma_v}{\sigma_v} \frac{2Kn}{1 - bKn} \right] \nabla P \tag{4.8}$$

where U_v is local viscous flow velocity, R_e is effective radius, μ is gas viscosity at standard condition, r is radius with respect to the central axis, Kn is local Knudsen number written as $Kn = \mu \sqrt{\pi RT/(2M)} \Big/ \left(\bar{P} R_e\right)$, b is slip coefficient. σ_v is tangential momentum accommodation

coefficient (TMAC). The TMAC is the parameter to quantify momentum exchange of gas molecules impinging on the wall and ranges from 0.2 to 1.2 (Beskok and Karniadakis, 1999). Furthermore, it is validated by the solutions of linearized Boltzmann equation that $b=-1$ provides the best fitting of the slip velocity (Beskok and Karniadakis, 1999). Furthermore, Beskok and Karniadakis (1999) have analyzed the influence of rarefaction on the dynamic gas viscosity, and proposed a correction term to characterize the degree of rarefaction effect in nanopores. As is designated in the conceptual model (see Figure 4.1), the viscous flow is constrained in the central zone by the virtual boundary (i.e., R_{vb}). Therefore, the molar flux of apparent viscous flow, J_v^A, is derived by the integration with respect to axial radius,

$$J_v^A = \frac{Q_v}{\pi R_0^2} = \frac{\bar{P}}{\pi R_0^2 RT}\left(1+\alpha Kn\right)\int_0^{R_{vb}} U_v \cdot 2\pi r dr \tag{4.9}$$

where Q_v is viscous flow molar rate, R_0 is nanocapillary radius, R is universal gas constant, T is temperature, $\bar{P}$ is average pressure across the nanocapillary. $\left(1+\alpha Kn\right)$ is the correction term to characterize rarefaction effect. α is dimensionless rarefaction coefficient expressed as $\alpha = 2\alpha_0 \tan^{-1}\left(4Kn^{0.4}\right)/\pi$, and α_0 is given as $\alpha_0 = 64/\left[3\pi\left(1-4/a\right)\right]$ where a is equal to -1 (Beskok and Karniadakis, 1999).

(3) Knudsen Diffusion Characterization

As illustrated in Figure 4.1, Knudsen diffusion exists in the middle annular zone. Roth (1982) has claimed that the molar rate of Knudsen diffusion, Q_k , can be characterized by

$$Q_k = -\frac{4}{3}\frac{\bar{v}}{RT}\frac{A_k^2}{S}\nabla P \tag{4.10}$$

where A_k is cross-section area of Knudsen diffusion flux and S is perimeter of the cross-section. $\bar{v}$ is apparent molecular velocity written as $\bar{v}=\sqrt{(8RT)/(\pi M)}$ where M is molar mass (Bird, 1994). In addition, Darabi et al. (2012) have indicated the impact of roughness on Knudsen diffusion in nanopores and introduced a correction factor, $\delta^{(D_f-2)}$, to Eq. 4.10. Hence, the apparent Knudsen diffusion molar flux, J_k^A, in the middle annular zone can be written as

$$J_k^A=\frac{\delta^{(D_f-2)}Q_k}{\pi R_0^2}=-\delta^{(D_f-2)}\frac{4}{3}\frac{\bar{v}}{\pi R_0^2 RT}\frac{\left(\pi R_e^2-\pi R_{vb}^2\right)^2}{2\pi R_e}\nabla P \tag{4.11}$$

where δ is the ratio of normalized molecule diameter to local effective pore diameter, i.e., $d_m/(2R_e)$. D_f is fractal dimension factor which ranges from 2.0 to 2.5 (Darabi et al., 2012).

Given the explicitly defined virtual boundary by Eq. 4.1, effective radius by Eq. 4.2, surface diffusion molar flux by Eqs. 4.6, molar flux of apparent viscous flow by Eq. 4.9, and molar flux of apparent Knudsen diffusion by Eq. 4.11, the total molar flux for ideal gas in the nanopore, J_t, can be characterized by

$$\begin{aligned}J_t&=J_v^A+J_k^A+J_s^A=w_vJ_v+w_kJ_k+w_sJ_s\\&=-w_v\left(1+\alpha Kn\right)\frac{R_e^4}{R_0^2}\frac{\bar{P}}{8\mu RT}\nabla P-w_k\frac{2}{3}\frac{R_e^3}{R_0^2}\delta^{(D_f-2)}\sqrt{\frac{8}{\pi RTM}}\nabla P\\&-w_sD_s\frac{\rho_m V_{\max}\rho_{sc}}{M}\frac{d\chi}{dP}\nabla P\end{aligned} \tag{4.12}$$

$$w_v=\frac{1}{\kappa}\left[1-\exp\left(-\xi\frac{1}{Kn}\right)\right]\left\{2-\frac{1}{\kappa}\left[1-\exp\left(-\xi\frac{1}{Kn}\right)\right]+\frac{2-\sigma_v}{\sigma_v}\frac{4Kn}{1-bKn}\right\} \tag{4.13}$$

$$w_k = \left\{1 - \frac{1}{\kappa}\left[1 - \exp\left(-\xi \frac{1}{Kn}\right)\right]\right\}^2 \tag{4.14}$$

$$w_s = 1 - \frac{R_e^2}{R_0^2} \tag{4.15}$$

$$\frac{d\chi}{dP} = \frac{1}{\overline{P_0}}\left\{\begin{array}{l} \dfrac{C_{BET}\left[1-(N+1)\tilde{P}^N + N\tilde{P}^{N+1}\right]}{(1-\tilde{P})^2\left[1+(C_{BET}-1)\tilde{P} - C_{BET}\tilde{P}^{N+1}\right]} - \dfrac{C_{BET}N(N+1)\tilde{P}^N}{1+(C_{BET}-1)\tilde{P} - C_{BET}\tilde{P}^{N+1}} \\ -\dfrac{C_{BET}\tilde{P}\left[1-(N+1)\tilde{P}^N + N\tilde{P}^{N+1}\right]\left[(C_{BET}-1) - C_{BET}(N+1)\tilde{P}^N\right]}{(1-\tilde{P})\left[1+(C_{BET}-1)\tilde{P} - C_{BET}\tilde{P}^{N+1}\right]^2} \end{array}\right\} \tag{4.16}$$

where w_v, w_k, and w_s are the weight coefficient of viscous flow molar flux, Knudsen diffusion molar flux, and surface diffusion molar flux, respectively. And weight coefficients play key roles in rationing the contribution of three flow mechanisms. $\tilde{P}$ is non-dimensionalized pressure expressed as $\tilde{P} = \overline{P}/\overline{P_0}$. Note that Eq. 4.12 is also capable to characterize the total molar flux in inorganic nanopores by setting $N = 0$ in Eq. 4.16 which leads to $R_e = R_0$. In this case, adsorption/desorption and surface diffusion are negligible in inorganic pores which meets the characterization in other literatures (Akkutlu and Fathi, 2012).

4.2.3 Modeling of Real Gas Flow in Porous Media

(1) Pore Confinement and Real Gas Effect Characterization

It has been reported that the phase behavior of fluids in nanopore differentiates from that of bulk fluids due to the pore confinement effect (Thommes and Findenegg, 1994). Peng and Robinson (1976) proposed a widely accepted equation of state (PR EOS) to describe the phase behavior of bulk fluid. Nonetheless, it cannot be applied in nanopores because massive molecules-wall

interactions in nanopores may undermine the intermolecular interaction and result in unexpected critical property shift (Singh et al., 2009). Yang et al. (2019c) have proposed a modified PR EOS by considering both critical property shift and the non-negligible capillary pressure to accommodate the nanoscale pore-confinement, which is written as

$$\overline{P} = \frac{RT}{V-B} - \frac{A-C}{V(V+B)+B(V-B)} \tag{4.17}$$

where V is molar volume, B is a coefficient representing the repulsive force between molecules and can be written as $B = 0.07780RT_c/P_c$, A is a coefficient representing the attractive force between molecules, and A can be defined as $A = 0.45724\varphi R^2T_c^2/P_c$, where T_c is critical temperature, P_c is critical pressure. Furthermore, φ is a dimensionless coefficient and can be expressed by

$$\varphi = \left[1+\left(0.37464+1.54226\varepsilon-0.26992\varepsilon^2\right)\left(1-\sqrt{T_r}\right)\right]^2 \tag{4.18}$$

where T_r denotes reduced temperature described as $T_r = T/T_c$, ε is acentric factor. C denotes a coefficient to modify the internal pressure caused by intermolecular interactions. Moreover, C can be expressed as $C = 3.374A\left(R_e/d_m\right)^{-1.637}$. The critical point can be achieved by locating the inflection point of Eq. 4.17 (i.e., first and second derivatives of pore pressure with respect to molar volume at critical temperature):

$$P_{cc} = 0.01324\frac{A-C}{B^2} \tag{4.19}$$

$$T_{cc} = 0.17015\frac{A-C}{RB} \tag{4.20}$$

where P_{cc} and T_{cc} are the confined critical pressure and temperature in nanopores, respectively. Various works have incorporated the Z-factor into the gas transport model to characterize the real gas effect (Ali and Malik, 2016; Song et al. 2016). Nonetheless, the correlations of Z-factor used in existing models is only valid for bulk fluids which may significantly affect the prediction of transport model. Yang et al. (2019c) have derived a Z-factor equation which considers the phase behavior in nano-confinement:

$$Z^3+(b-1)Z^2-(3b^2+2b-a+c)Z+(b^3+b^2-ab+bc)=0 \tag{4.21}$$

where $a=AP/(RT)^2$, $b=BP/(RT)$, $c=CP/(RT)^2$. It has been claimed that the largest one of three roots in Eq. 4.21 can be used as the Z-factor of equilibrium gas (McCain, 1990; Yang et al., 2019c). In addition, the gas viscosity in nanopores under the reservoir condition significantly differentiates from the constant value under the ideal gas condition. Sutton (2007) introduced a reliable dynamic viscosity correlation for free gas. Then, we modify the correlation considering confinement effect which is shown as

$$\mu_r=10^{-7}\mu\exp\left[X\left(\frac{\rho}{1000}\right)^Y\right] \tag{4.22}$$

$$\mu\vartheta=0.807T_{rc}^{\ 0.618}-0.357\exp(-0.449T_{rc})+0.340\exp(-4.058T_{rc})+0.018 \tag{4.23}$$

$$\vartheta=\frac{0.949(1.8T_{cc})^{(1/6)}}{(0.145\times10^{-3}P_{cc})^{(2/3)}\sqrt{1000M}} \tag{4.24}$$

where μ_r is real gas viscosity, ρ is real gas density expressed as $\rho=(\bar{P}M)/(ZRT)$. Y can be written as $Y=1.66378-0.04679X$ where $X=3.47+1588/(1.8T)+0.9M$. T_{rc} is reduced temperature for confined fluids which is defined as $T_{rc}=T/T_{cc}$.

(2) Equations Assembly in Straight Nanocapillary

Given pore-confinement and real gas effect characterized by Eqs. 4.17-4.24, Eqs. 4.12-4.16 can be accordingly rearranged. The total molar flux for real gas in the nanocapillary, J_{tr}, can be determined as

$$\begin{aligned} J_{tr} &= J_{vr}^{A} + J_{kr}^{A} + J_{sr}^{A} = w_{vr} J_{vr} + w_{kr} J_{kr} + w_{sr} J_{sr} \\ &= -w_{vr}\left(1+\alpha_r Kn_r\right)\frac{R_e^4}{R_0^2}\frac{\bar{P}}{8Z\mu_r RT}\nabla P - w_{kr}\frac{2}{3}\frac{R_e^3}{R_0^2}\delta^{(D_f-2)}\bar{P}C_g\sqrt{\frac{8}{\pi ZRTM}}\nabla P \\ &\quad -w_{sr}D_s\frac{\rho_m V_{\max}\rho_{sc}}{M}\frac{d\chi_r}{dP}\nabla P \end{aligned} \tag{4.25}$$

$$w_{vr} = \frac{1}{\kappa}\left[1-\exp\left(-\xi\frac{1}{Kn_r}\right)\right]\left\{2-\frac{1}{\kappa}\left[1-\exp\left(-\xi\frac{1}{Kn_r}\right)\right]+\frac{2-\sigma_v}{\sigma_v}\frac{4Kn_r}{1-bKn_r}\right\} \tag{4.26}$$

$$w_{kr} = \left\{1-\frac{1}{\kappa}\left[1-\exp\left(-\xi\frac{1}{Kn_r}\right)\right]\right\}^2 \tag{4.27}$$

$$w_{sr} = 1-\frac{R_e^2}{R_0^2} \tag{4.28}$$

$$\frac{d\chi_r}{dP} = \tilde{P}_r C_g\left\{\begin{aligned} &\frac{C_{BET}\left[1-\left(N+1\right)\tilde{P}_r^{\,N}+N\tilde{P}_r^{\,N+1}\right]}{\left(1-\tilde{P}_r\right)^2\left[1+\left(C_{BET}-1\right)\tilde{P}_r-C_{BET}\tilde{P}_r^{\,N+1}\right]}-\frac{C_{BET}N\left(N+1\right)\tilde{P}_r^{\,N}}{1+\left(C_{BET}-1\right)\tilde{P}_r-C_{BET}\tilde{P}_r^{\,N+1}} \\ &-\frac{C_{BET}\tilde{P}_r\left[1-\left(N+1\right)\tilde{P}_r^{\,N}+N\tilde{P}_r^{\,N+1}\right]\left[\left(C_{BET}-1\right)-C_{BET}\left(N+1\right)\tilde{P}_r^{\,N}\right]}{\left(1-\tilde{P}_r\right)\left[1+\left(C_{BET}-1\right)\tilde{P}_r-C_{BET}\tilde{P}_r^{\,N+1}\right]^2} \end{aligned}\right\} \tag{4.29}$$

where w_{vr}, w_{kr}, and w_{sr} are the weight coefficient of viscous flow molar flux, Knudsen diffusion molar flux, and surface diffusion molar flux for real gas, respectively. Kn_r is local Knudsen number for real gas which can be derived as $Kn_r = \mu_r\sqrt{\pi ZRT/(2M)}\big/\left(\bar{P}R_e\right)$. α_r is

rarefaction coefficient for real gas expressed as $\alpha_r = 2\alpha_0 \tan^{-1}\left(4Kn_r^{0.4}\right)/\pi$. $\tilde{P}_r$ is non-dimensionalized pressure for real gas which is expressed as $\tilde{P}_r = \overline{P}/\left(Z\overline{P_0}\right)$. C_g indicates real gas volume compressibility written as $C_g = 1/\overline{P} - 1/Z \cdot \left(dZ/dP\right)$ where dZ/dP can be further expressed as

$$\frac{dZ}{dP} = \frac{\left(Z-b\right)\left(\frac{C-A}{R^2T^2}\right) - \frac{B}{RT}\left[Z^2 - 2Z\left(3b+1\right) + \left(3b^2+2b-a+c\right)\right]}{3Z^2 + 2Z\left(b-1\right) - \left(3b^2+2b-a+c\right)} \tag{4.30}$$

Subsequently, the total apparent permeability for real gas in the nanocapillary, K_{tr} , can be determined as

$$\begin{aligned} K_{tr} &= K_{vr} + K_{kr} + K_{sr} \\ &= w_{vr}\left(1+\alpha_r Kn_r\right)\frac{R_e^4}{8R_0^2} + w_{kr}\frac{8R_e^4}{3\pi R_0^2}\delta^{\left(D_f-2\right)}C_g\overline{P}Kn_r \\ &+ w_{sr}D_s\frac{\rho_m V_{\max}\rho_{sc}}{M}\mu_r\frac{d\chi_r}{dP} \end{aligned} \tag{4.31}$$

where K_{vr} , K_{kr} , and K_{sr} is the apparent permeability of viscous flow, Knudsen diffusion and surface diffusion for real gas in organic nanocapillary, respectively.

(3) Upscaling Using Effective Medium Approximation

Various upscaling techniques have been applied in shale gas transport models to characterize the overall flow performance in shale matrix. Wu et al. (2016) adopted bundles-of-capillaries method to represent the shale strata. Nonetheless, such simple averaging method can only describe the homogeneous porous media with narrow pore size distribution and neglect the necessity of pore connectivity (Kirkpatrick, 1973). In contrast, the Effective Medium Approximation (EMA)

upscaling technique stems from statistical physics is competent to work in arbitrary disorganized system. Particularly, EMA provides an analytical approximation that transforms the heterogeneous system into a hypothetically homogeneous system with equivalent permeability where the spatial heterogeneity with respect to the pore size distribution are smoothed out and properties of original heterogeneous system are replaced with the representative properties (Landauer, 1978; Sahimi, 2003).

As is illustrated in Figure 4.4, various pore radii in non-uniform distribution (see Figure 4.4a) are replaced with the representative radius in a uniform distribution (see Figure 4.4b). Note that the representative radius is not simply an average pore size as is commonly used in bundles-of-capillaries method but a value reflecting the connectivity (i.e., coordination number) and pore size distribution of porous media (Doyen, 1988; Ghanbarian and Javadpour, 2017). The formulation to calculate the representative pore radius of the equivalent homogeneous system (i.e., R_a) is written as

$$\int_{R_{0\_\min}}^{R_{0\_\max}} \frac{R_a^4 - R_0^4}{R_0^4 + \left(n/2-1\right) R_a^4} f\left(R_0\right) dR_0 = 0 \tag{4.32}$$

where R_0 is nanocapillary pore radius, R_a is representative radius estimated by EMA, n is coordination number, $R_{0\_\max}$ and $R_{0\_\min}$ are the maximum and minimum pore radii in original heterogeneous medium, respectively. Ghanbarian and Javadpour (2017) provided a simple technique to estimate the pore coordination number of shale matrix by replacing n with $2/S_c$ where S_c denotes the critical mercury saturation on the mercury intrusion porosimetry curve obtained from the lab. S_c represents the percolation threshold which is a function of shale's pore connectivity.

It has been found that shale pore size in Eagle Ford, Pierre, Barnett, and Marcellus Formations follows either a lognormal or bimodal distribution (Milliken et al., 2013; Chen et al., 2015; Landry et al., 2016). Given the assumption of lognormal pore-size distribution in shale matrix, $f\left(R_0\right)$ can be determined based on a truncated lognormal probability density function as follows (Joekar-Niasar and Hassanizadeh, 2012).

$$f\left(R_0\right)=\frac{\sqrt{2}\exp\left[-\frac{1}{2\sigma^2}\left(\ln\frac{R_0}{R_m}\right)^2\right]}{\sqrt{\pi\sigma^2}R_0\left\{erf\left[\left(\ln\frac{R_{0\_\max}}{R_m}\right)\Big/\sqrt{2\sigma^2}\right]-erf\left[\left(\ln\frac{R_{0\_\min}}{R_m}\right)\Big/\sqrt{2\sigma^2}\right]\right\}} \tag{4.33}$$

where R_{m} is arithmetic mean pore radius, σ is standard deviation of log-normal distribution. Combining Eqs. 4.31 and 4.32, the total apparent permeability for real gas in the shale matrix, i.e., K_{tr_T}, is given as

$$\begin{aligned}K_{tr\_T}&=K_{vr\_T}+K_{kr\_T}+K_{sr\_T}\\&=\frac{\phi}{\tau}w_{vr\_T}\left(1+\alpha_{r\_T}Kn_{r\_T}\right)\frac{R_{e\_T}^4}{8R_a^2}+\frac{\phi}{\tau}w_{kr\_T}\frac{8R_{e\_T}^4}{3\pi R_a^2}\delta_T^{\left(D_f-2\right)}C_{g\_T}\bar{P}Kn_{r\_T}\\&+\frac{\phi}{\tau}w_{sr\_T}D_s\frac{\rho_m V_{\max}\rho_{sc}}{M}\mu_{r\_T}\frac{d\chi_{r\_T}}{dP}\end{aligned} \tag{4.34}$$

where K_{vr_T}, K_{kr_T}, and K_{sr_T} is the up-scaled permeability of viscous flow, Knudsen diffusion and surface diffusion for real gas, respectively. ϕ and τ is average porosity and tortuosity, respectively. R_a is representative radius estimated by EMA. Other parameters which are denoted with subscript sign ***T*** in Eq. 4.34 indicates that corresponding parameters in Eq. 4.31 are upscaled by replacing R_0 (i.e., nanocapillary radius) with R_a (representative pore radius calculated by Eq. 4.32).

4.3 Validation

In this work, we have made our validation for methane transport from two scales: a single straight organic nanocapillary (pore-scale) and a shale rock core sample (core-scale). In general, the molecular dynamics (MD) is capable to simulate the gas transport in nanocapillary with high accuracy in a limited time scale (Gad-el-Hak, 1999). Since experimental data considering adsorption and surface diffusion in the nanocapillary (e.g. <10 nm) are sparse, the MD simulation data from Yu et al. (2018) are collected to validate the methane apparent permeability in organic nanocapillary under shale reservoir pressures from 5 to 50 MPa. Yu et al. (2018) simulated the methane apparent permeability considering adsorption and surface diffusion by the non-equilibrium MD simulation. The pairwise interactions between particles were characterized by the consistent valence force field potential (CVFF) which included both long- and short-range force potential due to the acknowledged effectiveness of CVFF in methane flow and adsorption simulation (Wang et al., 2016). The detailed parameters in MD simulation are tabulated in Table 4.1.

Table 4.1: Summary of parameters used in MD simulation and EMA upscaling method

Scale		Organic Nanocapillary	Eagle Ford Shale Core
Data Sources		MD Simulation	Pulse Decay Experiment
Parameters	Symbol	Values	Values
Nanocapillary radius	R_0	6.00 nm	/
Arithmetic mean pore radius	R_m	/	6.96 nm
Maximum pore radius	R_{0_max}	/	39.64 nm
Minimum pore radius	R_{0_min}	/	1.46 nm
Standard deviation	σ	/	7.91 nm
Temperature	T	298.00 K	294.65 K
Average porosity	ϕ	/	0.062
Critical mercury saturation	S_c	/	0.13
Representative radius from EMA	R_a	/	16.79 nm

As for the shale core data, a pulse decay experiment on an Eagle Ford shale core sample has been conducted with the experimental error of 5% and a lognormal pore size distribution using nonlocal density functional theory (NLDFT) has been obtained (Alnoaimi and Kovscek, 2013). Their data are collected to validate the methane apparent permeability in up-scaled porous media. Since the pore coordination number of shale matrix is unavailable (Alnoaimi and Kovscek, 2013), the critical mercury saturation (i.e., S_c) of Eagle Ford shale core provided by Ghanbarian and Javadpour (2017) is adopted to estimate the coordination number. The detailed parameters in pulse decay test and representative radius estimated by EMA are tabulated in Table 4.1.

4.3.1 Validation Methodology

The calculation of apparent permeability requires estimations of eleven empirical parameters including ζ, C_{BET}, D_f, ξ, V_{max}, D_s, σ_v, τ, κ, β, and N, which are obtained using optimization techniques. Based on the physical significance of these parameters, specific constraints are assigned to them in the optimization process as follows: $0 < \zeta \le 1$ (Xiong et al., 2012), $1.00 \le C_{BET} \le 24.43$ (Wang et al., 2017), $2.0 \le D_f \le 2.5$ (Darabi et al., 2012), $0 < \xi \le \sqrt{R_0^2 + L^2} \,/ R_0$ (Chai et al., 2019a), $3.596\times10^{-3} \le V_{\max} \le 9.466\times10^{-3}$ (Santos and Akkutlu, 2013), $1.0\times10^{-9} \le D_s \le 8.8\times10^{-6}$ (Akkutlu and Fathi, 2012), $0.2 \le \sigma_v \le 1.2$ (Beskok and Karniadaiks, 1999), $1.26 \le \tau \le 12.20$ (Chen et al., 2015), $\kappa \ge 1 - \exp\left(-\xi / Kn_r\right)$, $0 \le \beta \le 1$, and $1 \le N \le R_0 / d_m - \zeta + 1$. Note that the constraints of κ, β, and N are derived from the radius inequalities in the conceptual model, i.e., $R_{vb} \le R_e$, $R_1 - (N-1)d_m \le R_e$, $R_1 - (N-1)d_m \ge 0$, respectively.

Considering the high nonlinearity of the apparent permeability formulation, an iterative ensemble smoother (ES) algorithm proposed by Chen and Oliver (2012) is adopted to estimate the eleven independent and continuous empirical parameters by assimilating all measured data simultaneously. Particularly, it is robust and pragmatic to handle multiple-parameter estimation problems when the relationship between the measured data and the model parameters is strongly nonlinear (Fan et al., 2018). Chen and Oliver (2012) have introduced the updating equation of the iterative ES algorithm for model parameters as follows.

$$\begin{aligned} m^{l+1} &= \beta_l m_{pr} + (1-\beta_l) m^l - \beta_l C_M G_l^T \left(C_P + G_l C_M G_l^T \right)^{-1} \\ &\times \left[g\left(m^l\right) - d_{obs} - G_l \left(m^l - m_{pr} \right) \right] \end{aligned} \tag{4.35}$$

where m^l and m^{l+1} denote the ensemble of to-be-tuned model parameters at the lth and (l+1)th iteration, respectively. β_l is damping factor which is the step length parameter that can be determined by standard line search, m_{pr} denotes the prior distribution of model parameters, C_M denotes covariance matrix of model parameters, Cp is covariance matrix of collected permeability data, $g(\cdot)$ denotes proposed apparent permeability formulation in this work, G_l denotes sensitivity matrix which is a linearization of $g(\cdot)$ at the lth iteration, d_{obs} denotes collected permeability data, T denotes the transpose sign of a matrix. In the initialization of the optimization, the ensemble size is set as 50. The prior distribution of model parameters is set as Gaussian distribution whose mean and standard deviation (e.g. < 0.1) are within the previously defined physical constraints. It takes 24 to 35 mins for running the optimization process.

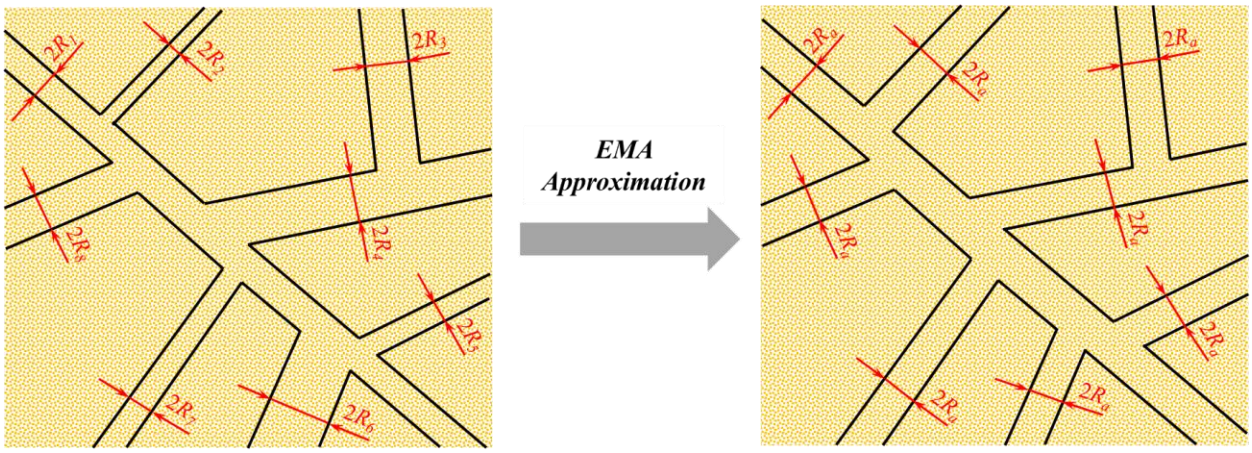

Figure 4.4: EMA schematic diagram: (a) shale matrix with various pore radii in non-uniform distribution can be replaced with (b) a hypothetically equivalent shale matrix with representative radius (i.e., R_a) in a uniform distribution by the use of Effective Medium Approximation (EMA).

4.3.2 Validation Results

Figure 4.5 shows the calculated and realistic apparent permeability versus mean pressure in a nanocapillary. Grey lines in Figure 4.5a illustrate 50 initial realizations of apparent permeability generated by the iterative ES algorithm while the green square dots are the realistic data (i.e., collected permeability data from Yu et al. (2018)). The ensemble in Figure 4.5a presents simulated apparent permeability, which exhibits a similar trend with the realistic data because the prior distribution of model parameters is set as Gaussian distribution. Figure 4.5b presents the optimal realization in the ensemble (i.e., black line) obtained by the iterative ES algorithm. It is seen that the developed model (i.e., Eq.4.31) is capable to accurately reproduce the realistic data from Yu et al. (2018) with an average error of 4.85%. Therefore, the validation demonstrates that the proposed model can yield a satisfactory prediction with optimized model parameters.

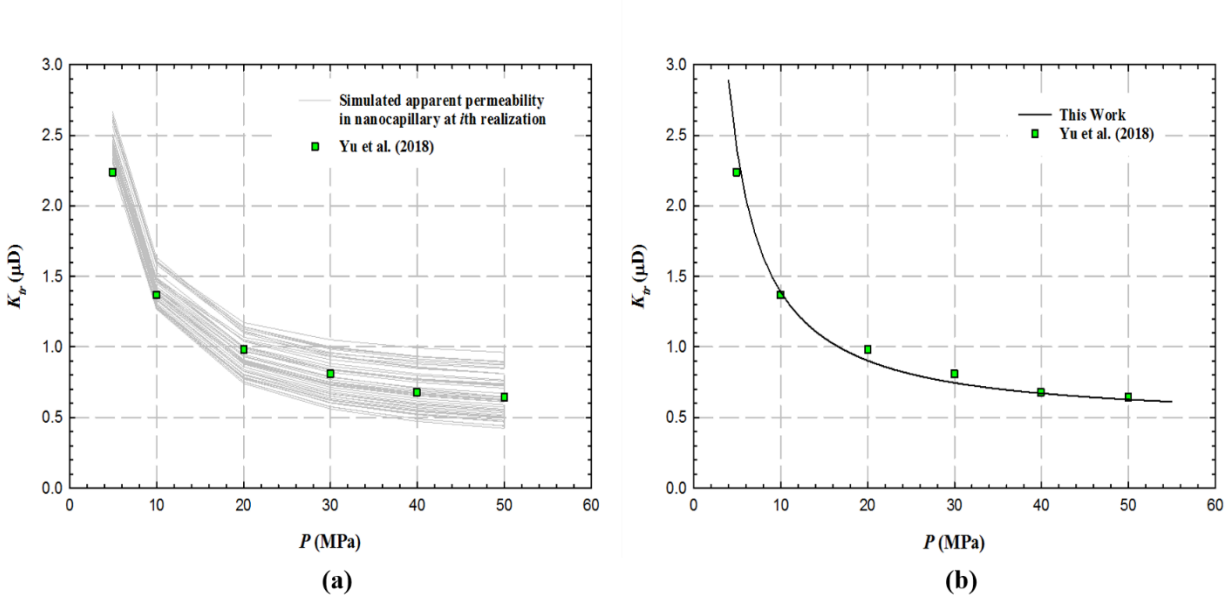

Figure 4.5: Calculated and realistic apparent permeability versus mean pressure in a nanocapillary: (a) grey lines show 50 initial realizations of apparent permeability generated by iterative ES algorithm and green square dots are realistic apparent permeability from the MD simulation. (b) black line shows the optimal realization obtained by the iterative ES algorithm.

Figure 4.6 shows the calculated and realistic apparent permeability versus mean pressure in the Eagle Ford shale core. Similarly, grey lines in Figure 4.6a illustrate 50 initial realizations of apparent permeability and the red circular dots with 5% error bars are the realistic data (i.e., collected permeability data from Alnoaimi and Kovscek (2013)). Figure 4.6b shows the optimal realization determined by the iterative ES algorithm. It is seen in Figure 4.6b that the upscaled model (i.e., Eq. 3.34) is able to accurately reproduce the observation data from Alnoaimi and Kovscek (2013) with an average error of 4.29%. Therefore, the newly proposed model is further validated by the experimental data in addition to the numerical data. The optimized parameters by the iterative ES algorithm in the validation process have been respectively tabulated in Table 4.2.

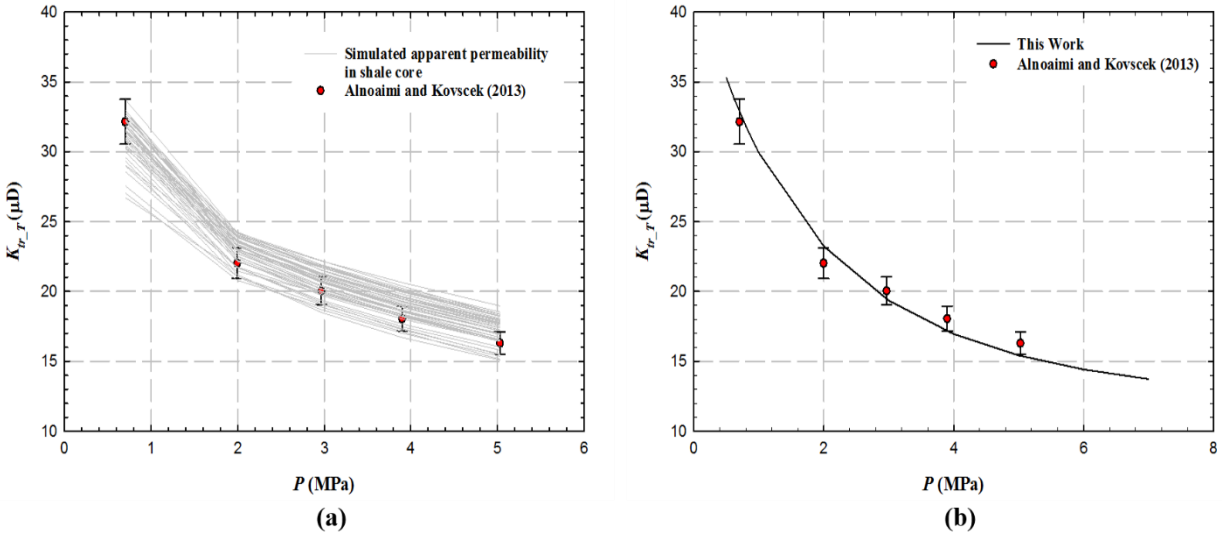

Figure 4.6: Calculated and realistic apparent permeability versus mean pressure in Eagle Ford shale core: (a) grey lines show 50 initial realizations of apparent permeability generated by iterative ES algorithm and red circular dots with 5% error bars are realistic apparent permeability from the pulse decay experiment. (b) black line shows the optimal realization obtained by the iterative ES algorithm.

Table 4.2: Summary of parameters in validation

Parameters in nanocapillary	Data Sources	Unit	Values
ζ	Given in literature	dimensionless	1.00
C^*_{BET}	Optimized	dimensionless	9.88
D_f	Given in literature	dimensionless	2.00
ξ^*	Optimized	dimensionless	0.02
V^*_{max}	Optimized	m^3/kg	3.99×10^{-3}
D^*_s	Optimized	m^2/s	1.45×10^{-9}
σ^*_v	Optimized	dimensionless	0.35
τ	Given in literature	dimensionless	1.00
κ^*	Optimized	dimensionless	1.30
β	Given in literature	dimensionless	1.00
N	Given in literature	dimensionless	1.00
Parameters in shale core	Data Sources	Unit	Values
ζ^*	Optimized	dimensionless	0.79
C^*_{BET}	Optimized	dimensionless	10.32
D^*_f	Optimized	dimensionless	2.39
ξ^*	Optimized	dimensionless	0.09
V^*_{max}	Optimized	m^3/kg	7.42×10^{-3}
D^*_s	Optimized	m^2/s	8.61×10^{-6}
σ^*_v	Optimized	dimensionless	0.82
τ^*	Optimized	dimensionless	3.71
κ^*	Optimized	dimensionless	0.99
β^*	Optimized	dimensionless	0.92
N^*	Optimized	dimensionless	3.00

4.4 Results and Discussion

The validated model for the Eagle Ford shale core is applied to analyze involved mechanisms for methane in this section. The key parameters used in the simulation as listed in Table 4.3 are consistent with that in core validation.

Table 4.3: Summary of parameters used in the simulation

Parameters	Symbol	Unit	Values
Chemical confinement parameter	ξ	dimensionless	0.09
Velocity direction heterogeneity parameter	κ	dimensionless	0.99
Reservoir temperature	T	K	323
Fractal dimension of the pore surface	D_f	dimensionless	2.39
Universal gas constant	R	J/mol/K	8.314
Nominal methane molecule size	d_m	nm	0.38
Methane molar mass	M	kg/mol	0.016
Methane critical pressure	P_c	Pa	4.60×10^{6}
Methane critical temperature	T_c	K	190.55
Average porosity	ϕ	dimensionless	0.062
Average tortuosity	τ	dimensionless	3.71
Equivalent fraction of adsorption layers	β	dimensionless	0.92
Actual number of adsorbed layers	N	dimensionless	3
Surface diffusivity coefficient	D_s	m^2/s	8.61×10^{-6}
Shale grain density	ρ_m	kg/m^3	2659.06
Methane density at standard condition	ρ_{sc}	kg/m^3	0.64
Thickness correction coefficient	ζ	dimensionless	0.79
BET Equilibrium constant	C_{BET}	dimensionless	10.32
First-layer maximum adsorption volume per unit	V_{max}	m^3/ kg	7.42×10^{-3}
Tangential momentum accommodation coefficient	σ_v	dimensionless	0.82
Representative radius estimated by EMA	R_a	nm	16.79
Methane acentric factor	ε	dimensionless	0.01

4.4.1 Sensitivity Analyses

Fitting empirical parameters in the proposed model (i.e., Eq. 3.34) are firstly analyzed for the sensitivity on methane gas apparent permeability in shale matrix. The optimized values of empirical parameters in validation are set up as the reference inputs to calculate the baseline of the apparent permeability under gas-shale reservoir pressures from 3.0 to 50.0 MPa. Subsequently, the reference dataset is disturbed by 10% positively and negatively to generate inputs for the sensitivity analysis. Next, the minimum and maximum relative errors of the calculated apparent

permeability with respect to the baseline are determined as presented in the tornado plot (see Figure 4.7). It can be seen that the actual number of adsorbed layers (i.e., N) has the most significant impact on the apparent permeability, of which the relative error changes from -23.40% to 28.31%. In contrast, the fractal dimension has the least impact, which only changes from -0.08% to 0.20%. Furthermore, empirical parameters in the proposed model can be categorized into three groups: i) multilayer adsorption and surface diffusion related parameters including N, D_s, V_{max}, β, ζ, and C_{BET}; ii) free gas kinetic parameters including κ, σ_v, and ξ; and iii) shale matrix structural parameters including τ and D_f. It is observed that multilayer adsorption and surface diffusion related parameters basically make most of contributions to the apparent permeability except structural parameter τ. The impact from free gas kinetics and pore-wall roughness which is represented by the fractal dimension of the pore surface (i.e., D_f) are significantly weakened when the multilayer adsorption is in presence.

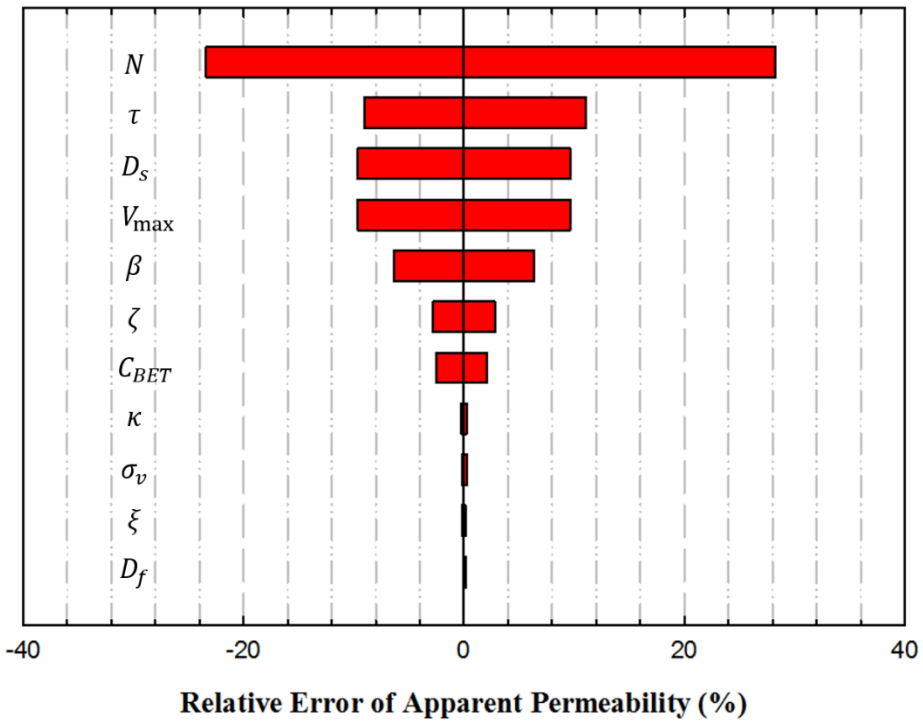

Figure 4.7: Sensitivity analyses on various empirical parameters.

4.4.2 Analyses of Pore Confinement, Real Gas Effect, and Multilayer Adsorption Effect

Figure 4.8 presents the influence of pore size and adsorption layer number on the real gas compressibility factor of methane under pressures from 0.1 to 70.0 MPa at reservoir temperature of 323 K. It is seen in Figure 4.8a that the real gas compressibility factor of confined and bulk gas changes with pressure in inorganic nanopores with pore sizes from 3 to 50 nm. Since the gas adsorption in inorganic nanopores can be neglected (Wu et al., 2016), the real gas compressibility factor in inorganic nanopores is only affected by the pore size, pressure and temperature. It is shown that real gas compressibility factors in all pore sizes behave non-monotonically in the low-pressure region below 18.0 MPa, and then increase with the pressure. Given specific pressure, it is found the compressibility factor decreases to the value of bulk fluid as the pore size increases from 3 to 50 nm. And the compressibility factor at pore size of 50 nm is exactly the same as that

of bulk fluid. Given specific pressure, it is also observed that the difference between compressibility factor curve and bulk fluid curve declines rapidly with the increase of pore size, especially when the pore size is larger than 6 nm. Therefore, it indicates that the pore confinement effect is only in presence below the pore size of 50 nm, and the pore confinement effect declines significantly as the pore size approaches 50 nm. This observation also demonstrates the validity of our model validation in nanocapillary using the 6 nm nanopore, which incorporates the strong pore confinement effect. Figure 4.8b presents that the real gas compressibility factor of confined and bulk gas changes with pressure in organic nanopores with pore size of 6 nm. It is seen that multilayer adsorption has strong impact on the real gas compressibility factor, and the real gas compressibility factor declines with the decreasing adsorption layer number at given pressure. In addition, the difference between the compressibility factor curve with adsorption and the compressibility factor curve without adsorption diminishes rapidly with the decrease of adsorption layer number at given pressure, especially when the adsorption layer number is less than 3. This indicates that the increase of adsorption layers can decrease the pore space for free gas transport, which can result in the similar pore confinement impact on the methane compressibility factor as in illustrated in Figure 4.8a.

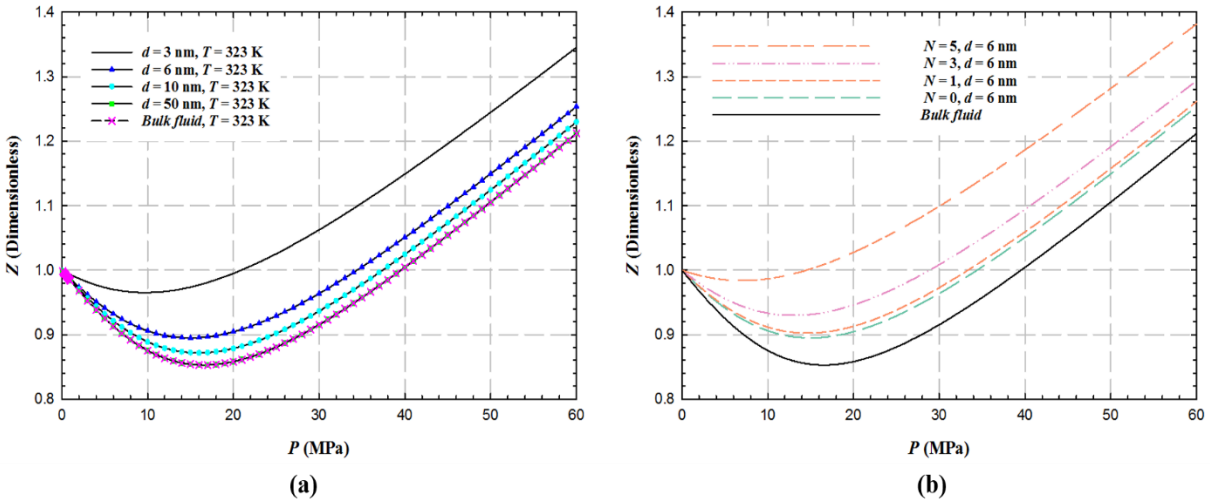

Figure 4.8: Real gas compressibility factor of confined and bulk methane gas versus mean reservoir pressure in inorganic and organic nanopores: (a) shows real gas compressibility factor changes with pressures in various nanopore sizes and in bulk fluid state under isothermal condition. Note the curve with green dots (i.e., d = 50 nm) coincides with the curve with pink crosses (i.e., Bulk fluid). (b) shows real gas compressibility factor changes with pressures in various adsorption conditions and in bulk fluid state in fixed nanopore size.

Figure 4.9 exhibits the influence of pore size and adsorption layer number on the viscosity of confined real and ideal methane gas under pressures from 0.1 to 70.0 MPa at reservoir temperature of 323 K. It is shown in Figure 4.9a that viscosity of real gas (i.e., μ_r) changes with pressure rather than a constant for the ideal gas (i.e., μ) as defined in aforementioned analytical models (Xiong et al., 2012; Wasaki and Akkutlu, 2015; Wu et al., 2016; Ghanbarian and Javadpour, 2017). The real gas viscosity increases significantly from 0.013 to 0.037 cP when the pressure increases from 5.0 to 60.0 MPa, which indicates that real gas effect cannot be ignored under shale reservoir conditions (e.g. P = 5.0-50.0 MPa, T = 323K). Given specific pressure, it is also found the real gas viscosity decreases with the increase of pore size below 35.0 MPa, whereas the viscosity increases with the increase of pore size above 35.0 MPa. This implies the coupling effect from pore-confinement and real gas effect exerts opposite impacts on methane viscosity at high and relatively low pressures. Moreover, the real gas viscosity is equal to the ideal gas viscosity at pressure of 0.1

MPa and pore size of 50 nm, which reveals that the confined gas has become the bulk gas because the pore confinement effect disappears at pore size of 50 nm, and the viscosity of real and ideal bulk gas is much close at low pressures. Figure 4.9b illustrates that the viscosity of confined real gas changes with pressure in organic nanopores with pore size of 6 nm. It is found that the real gas viscosity decreases with the decrease of adsorption layer number below 38.0 MPa, whereas the viscosity increases with the increase of pore size above 35.0 MPa. Similarly, the change of multilayer adsorption thickness is inversely related to the change of pore size as in Figure 4.9a.

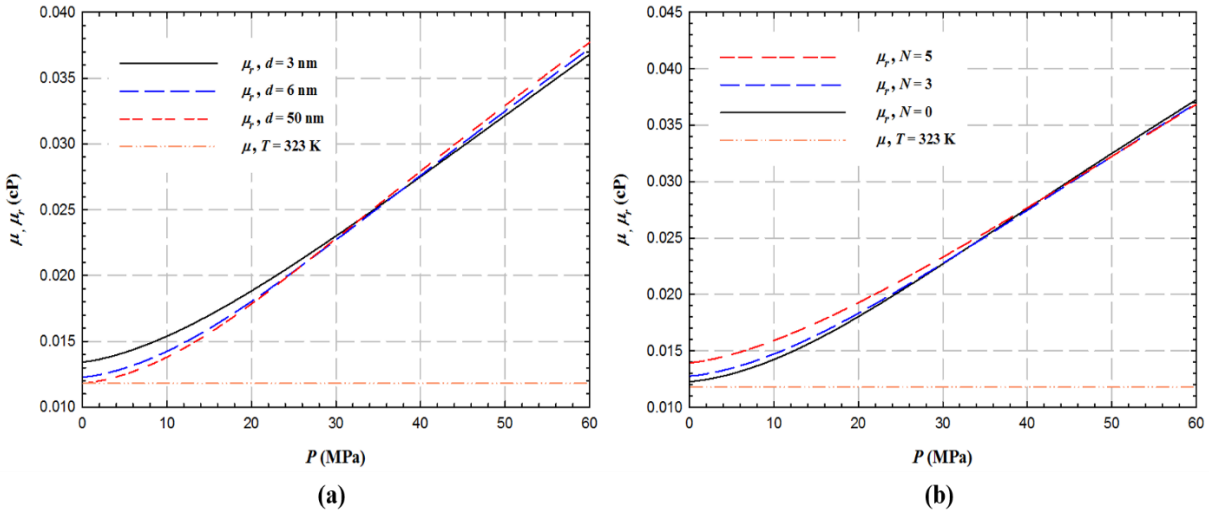

Figure 4.9: Comparison of methane viscosity between ideal and real gas in different pore sizes and adsorption conditions: (a) shows ideal and real gas viscosity changes with pressures in various nanopore sizes. Note both ideal and real gas viscosity are under the temperature of 323 K. (b) shows ideal and real gas viscosity changes with pressures in various adsorption conditions. Note both ideal and real gas viscosity are under the temperature of 323 K.

Figure 4.10 shows the apparent permeability for real gas in 6 nm pore changes with mean pressures from 5.0 to 50.0 MPa at reservoir temperature of 323 K in three scenarios: inorganic nanopores (i.e., without adsorption and surface diffusion, $N=0$), organic nanopores with monolayer adsorption which is calculated based on Langmuir model (i.e., $N=1$), and organic nanopores with multilayer adsorption which is calculated based on BET model (e.g., $N=3$). Figure 4.10b is an enlarged view of the curve for inorganic nanopores in Figure 4.10a. It can be found that apparent

permeability in all three scenarios decline with the pressure. The apparent permeability in inorganic nanopores exhibits the least decline from 0.76 to 0.68 cP, while the organic nanopore with multilayer adsorption shows the largest decline from 13.91 to 4.12 cP. Moreover, it is seen that the apparent permeability increases significantly as the adsorption layer number increases. This is mainly because increasing adsorption layers can result in considerable increment of surface diffusion flux which contributes to the apparent permeability. Although increasing adsorption layers can weaken the contribution of free gas due to decreasing flow space, the negative effect can be completely offset by the increment of surface diffusion. In addition, the large difference between the apparent permeability calculated from Langmuir model and BET model implies that the application of Langmuir model in existing gas transport models may extensively underestimate the apparent permeability.

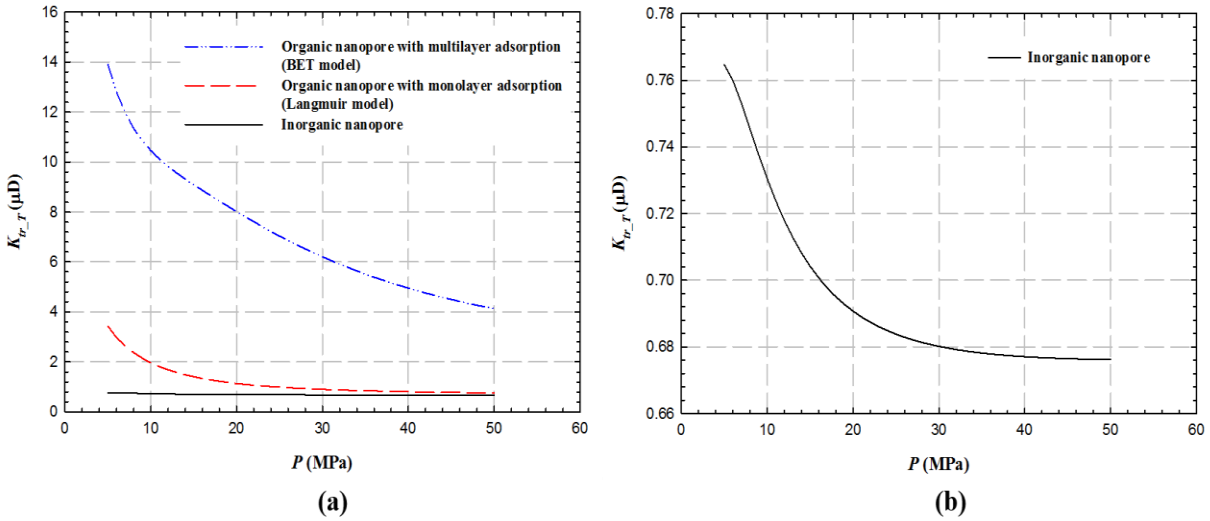

Figure 4.10: Apparent permeability for real gas under reservoir pressures in inorganic and organic pores with different adsorption conditions: (a) shows total apparent permeability for real gas in shale matrix changes with pressures in three different adsorption conditions. (b) shows an enlarged view of the curve for inorganic nanopores in subplot (a).

4.4.3 Contributions of Flow Mechanisms

Figure 4.11 presents the contributions of viscous flow and Knudsen diffusion to the apparent permeability in inorganic nanopores with pore size of 2, 5, 10, and 20 nm from 3.0 to 50.0 MPa at temperature of 323 K. It is found that as pressure and pore size decreases, the contribution of Knudsen diffusion increases, whereas the contribution of the viscous flow declines. This is attributed to the fact that the free-gas flow pattern approaches high-Knudsen flow in nanopores as pressure and pore size decrease. Moreover, it can be observed in Figure 4.11a that the viscous flow in 2 nm pore contributes from 11.23% up to 56.64% when pressure is more than 5.0 MPa. Meanwhile, the contribution of Knudsen diffusion declines from 93.11% to 43.36% ranging from 3.0 to 50.0 MPa. As shown in Figure 4.11d, the viscous flow in 20 nm pore is completely dominant when the pressure is above 5.0 MPa. As can be seen in Figure 4.11b, Knudsen diffusion in 5 nm pore still keeps slight contribution above 5.80% across the entire pressure range. In contrast, it is found in Figure 4.11c that the contribution of Knudsen diffusion in 10 nm pore is negligible when the pressure is more than 12.0 MPa. Therefore, it can be concluded that given inorganic nanopores, the viscous flow is important at any pore sizes under reservoir conditions (i.e., 5.0-50.0 MPa) and completely dominant when the pore size is larger than 20 nm; meanwhile, the Knudsen diffusion cannot be neglected in the pore size below 5 nm under reservoir conditions (i.e., 5.0-50.0 MPa) and in the pore size below 10 nm when pressure is from 5.0 to 12.0 MPa, respectively.

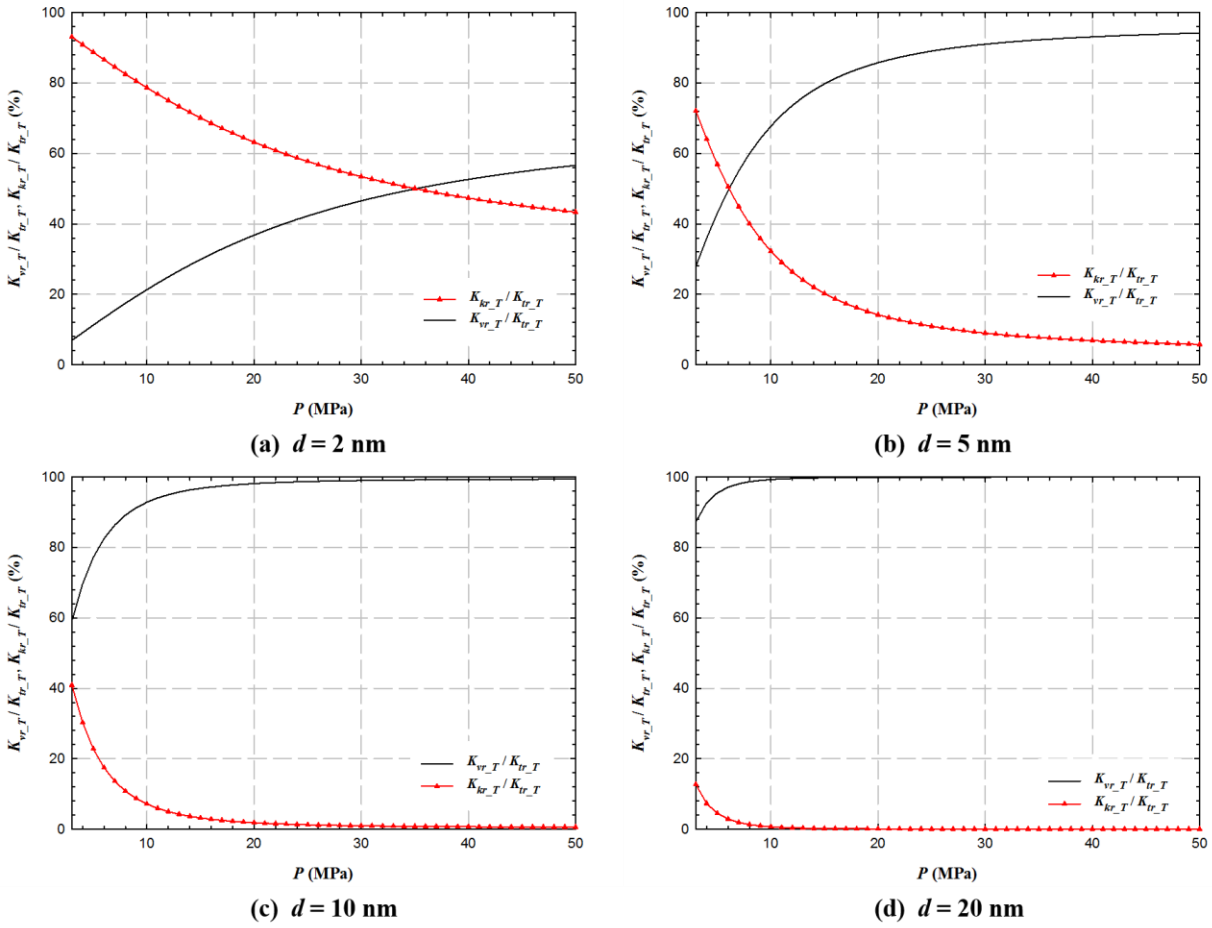

Figure 4.11: Apparent permeability contributions from viscous flow and Knudsen diffusion with respect to reservoir pressures in inorganic nanopores with four various pore sizes. Note there are no adsorption layers in all four figures.

The situation is quite different in organic nanopores considering multilayer adsorption and surface diffusion. Figures 4.12 exhibits the contributions of viscous flow, Knudsen diffusion, and surface diffusion to the apparent permeability in inorganic nanopores with pore size of 20, 80, 150, and 270 nm from 3.0 to 50.0 MPa at temperature of 323 K. As is seen in Figure 4.12, the apparent permeability of surface diffusion increases as pressure and pore size decreases. This is mainly because that the specific surface area increases with the shrinking pore size which leads to more adsorption and surface diffusion. In addition, it is observed in Figures 4.12a and 4.12b, the surface diffusion greatly contributes to apparent permeability accounting for 99.35% to 97.21% in 20 nm

and 65.27% to 32.10% in 80 nm from 3.0 to 50.0 MPa, respectively. Nonetheless, as is seen in Figures 4.12c and 4.12d, the contribution of surface diffusion is not significant that it drops to 6.59% in 150 nm pore in Figure 4.12c and below 4.52% in 270 nm pore across entire reservoir pressure range in Figure 4.12d. In contrast, the contribution of viscous flow can be neglected in 20 nm pore (<2.79%), but it turns to be important when the pore size is larger than 80 nm across entire reservoir conditions (>34.69%). In addition, it should be noted that the contribution of Knudsen diffusion is completely negligible when the pore size is larger than 20 nm under reservoir conditions. Furthermore, the Knudsen diffusion contribution in Figure 4.12a is much lower than that in Figure 4.11d. This implies that the multilayer adsorption and surface diffusion on the pore-wall occupy much space of Knudsen diffusion zone (see Figure 4.1) and highly affect the Knudsen diffusion flux near the pore-wall. Overall, the conclusion can be drawn that given organic nanopores, the contribution of surface diffusion plays a dominant role when the pore size is below 20 nm and cannot be neglected when the pore size is below 150 nm. Meanwhile, the viscous flow is important when the pore size is larger than 80 nm and is completely dominant when the pore size is larger than 270 nm. And the Knudsen diffusion can be ignored under reservoir conditions.

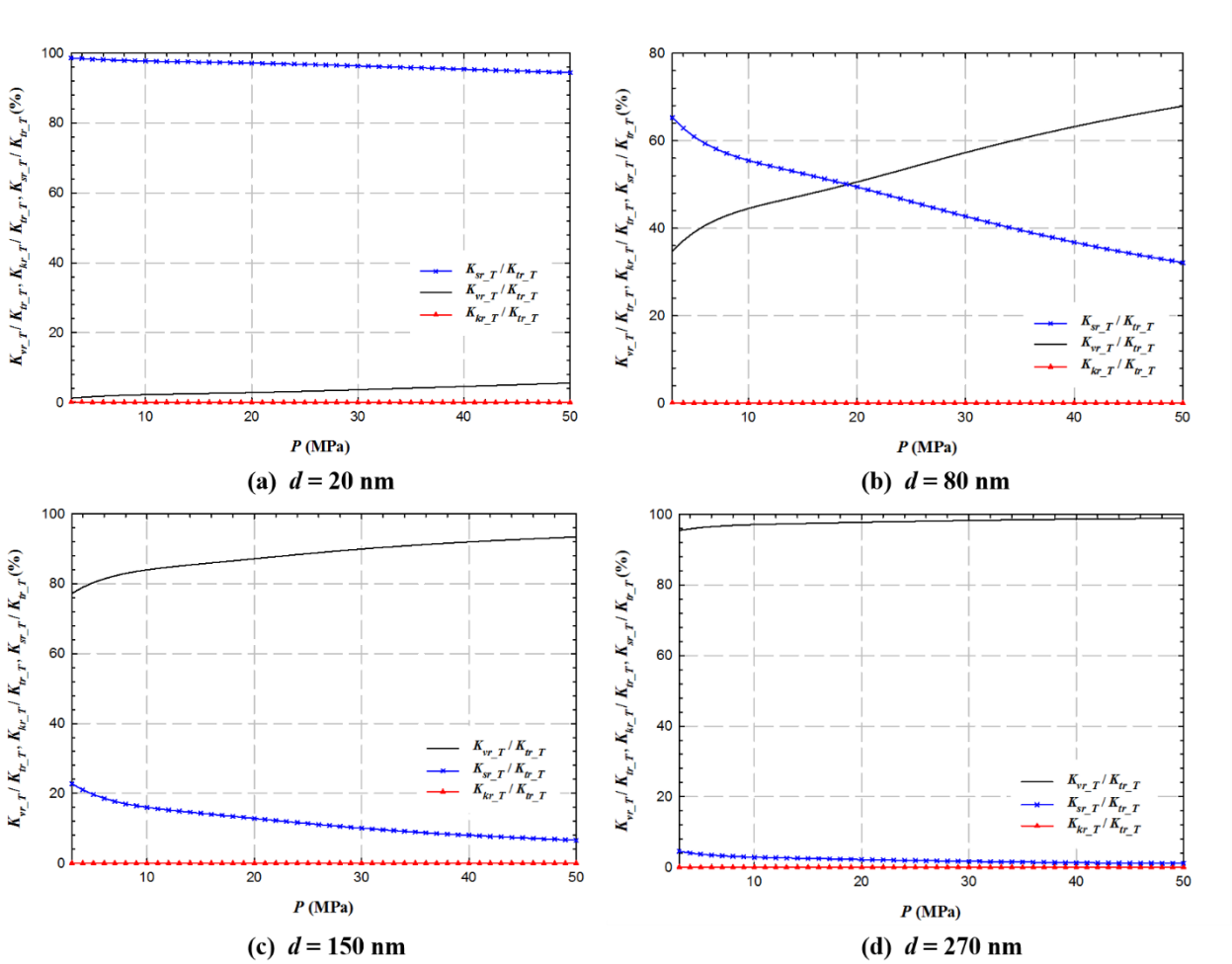

Figure 4.12: Apparent permeability contributions from viscous flow, Knudsen diffusion and surface diffusion with respect to reservoir pressures in organic nanopores with four various pore sizes. Note there are three adsorption layers in all four figures.

4.5 Summary

A novel comprehensive model is proposed which is capable to characterize the shale gas flow over the full flow regimes not only in inorganic and organic nanopores, but also in complicated shale matrix by the use of effective medium approximation under typical reservoir conditions. Meanwhile, the model has been first coupled with multilayer adsorption, surface diffusion, and pore-confinement effect, and has been successfully validated using the efficient Batch-EnRML optimization method. It is found the pore confinement effect is only in presence below the pore

size of 50 nm, and the pore confinement effect declines significantly as the pore size approaches 50 nm. Furthermore, the significant increase of gas viscosity due to real gas effect under reservoir conditions cannot be ignored. The enhancement of pore confinement effect and multilayer adsorption can increase the real gas compressibility factor. In contrast, the coupling effect from pore-confinement and real gas effect exerts opposite impacts on methane viscosity at high and relatively low pressures. The apparent permeability increases significantly as the adsorption layer number increases and the application of Langmuir model in existing gas transport models may extensively underestimate the apparent permeability. In addition, given inorganic nanopores, the viscous flow is important at any pore sizes under reservoir conditions and the Knudsen diffusion cannot be neglected in the pore size below 5 nm under reservoir conditions and in the pore size below 10 nm when pressure is from 5.0 to 12.0 MPa, respectively. Given organic nanopores, the contribution of surface diffusion plays a dominant role when the pore size is below 20 nm and cannot be neglected when the pore size is below 150 nm. Meanwhile, the viscous flow is important when the pore size is larger than 80 nm and the Knudsen diffusion can be ignored under reservoir conditions.

CHAPTER 5: MULTI-SCALE SIMULATIONS OF GAS FLOW IN SHALE CORES USING A PRACTICAL GAS APPARENT PERMEABILITY MODEL

5.1 Introduction

This work presents the simulations at both the pore-scale and shale core-scale. At the fine scale in nanopores, the previously developed analytical AP model (see Chapter 4) is adopted. Subsequently, the AP is numerically coupled in the diffusivity equation and simulated at core-scale by coupling various mechanisms in shale matrix for theoretical completeness. Meanwhile, physical terms in AP model are simplified with semi-empirical correlations for the practicability in large-scale field simulation. Compared with other gas transport models in nanopores, the newly-developed analytical model has been successfully validated against molecular dynamic (MD) simulation, direct simulation Monte Carlo (DSMC), Lattice Boltzmann (LB) simulation, and experimental flux results for five types of gases (i.e., methane, nitrogen, helium, argon, and oxygen) with the minimum deviation. This work provides an analytical model which not only considers non-negligible multi-physics in shale reservoirs (i.e., rarefaction effect, multilayer adsorption, surface diffusion and confinement effect) but also simplifies non-linear physical terms using semi-empirical linear correlations to facilitate AP calculations in large-scale simulations.

5.2 Mathematical Formulation

5.2.1 Modeling of Shale Gas Flow in Nanocapillary

The proposed analytical model in Chapter 4 is utilized to characterize the rarefied gas flow in nanopores. This is because the contributions of various flow mechanisms have been rigorously quantified based on collision probability between molecules and the pore-wall. Moreover, in the layer-sequence model, the mutually independent weight coefficients are explicitly parameterized

with Knudsen number (i.e., the ratio of molecular mean free path to characteristic length), which enables the model to calculate the gas molar flux in the full flow spectrum of nano-scale porous media.

(1) Modeling of Total Mass Flux

The mass flux of viscous flow in central zone, F_v^n, can be expressed as follows.

$$F_v^n = \vartheta \frac{\bar{P}M}{\pi r_o^2 RT} \int_0^{r_c} u_v \cdot 2\pi r dr \tag{5.1}$$

It should be pointed out the second-order Maxwell slip model is insufficient to predict the flux, though the velocity profile is valid in full flow regimes. Hence, Karniadakis et al. (2005) added the correction term $\vartheta = (1 + \alpha Kn)$ as shown in Eq. 5.1 to characterize the rarefaction impact on the gas dynamic viscosity. α denotes rarefaction coefficient which is defined as

$$\alpha = \alpha_0 \frac{2}{\pi} \arctan\left(\alpha_1 Kn^{\alpha_2}\right) \tag{5.2}$$

where α_1=4.0, α_2=0.4, and α_0 denotes an asymptotic upper limit value as $64/(15\pi)$. Since Knudsen diffusion occurs in the outer annular zone, the mass flux, F_k^n, can be calculated using a generalized Knudsen equation for arbitrary geometrical cross-section based on Eq. 2.8 (Roth, 1982).

$$F_k^n = -\frac{4}{3}\frac{S^2}{H}\sqrt{\frac{8M}{\pi RT}}\frac{\nabla P}{\pi r_o^2} = -\frac{4}{3}\frac{\left(\pi r_o^2 - \pi r_c^2\right)^2}{2\pi r_o}\sqrt{\frac{8M}{\pi RT}}\frac{\nabla P}{\pi r_o^2} \tag{5.3}$$

where S denotes cross-section area of outer annular zone and H is outer circumference of the cross-section. Consequently, the total mass flux of rarefied gas in nanocapillary, F_t, can be calculated as follows.

$$\begin{aligned} F_t &= F_v^n + F_k^n = w_v F_c + w_k F_k \\ &= -w_v \vartheta \frac{r_o^2}{8} \frac{\bar{P}M}{\mu RT} \nabla P - w_k \frac{2r_o}{3} \sqrt{\frac{8M}{\pi RT}} \nabla P \end{aligned} \tag{5.4}$$

$$w_v = \frac{1}{\hbar}\left[1 - \exp\left(-\frac{\theta}{Kn}\right)\right]\left\{2 - \frac{1}{\hbar}\left[1 - \exp\left(-\frac{\theta}{Kn}\right)\right] + \frac{4Kn}{1+Kn}\right\} \tag{5.5}$$

$$w_k = \left\{1 - \frac{1}{\hbar}\left[1 - \exp\left(-\frac{\theta}{Kn}\right)\right]\right\}^2 \tag{5.6}$$

To apply the model at different scales, the mass flux can be nondimensionalized in terms of Hagen-Poiseuille equation (i.e., Eq. 2.6) and Knudsen equation (i.e., Eq. 2.8) as F_{tv}^* and F_{tk}^*, respectively.

$$F_{tv}^* = \frac{F_t}{F_c} = w_v \vartheta + w_k \frac{64}{3\pi} Kn \tag{5.7}$$

$$F_{tk}^* = \frac{F_t}{F_k} = w_v \vartheta \frac{3\pi}{64Kn} + w_k \tag{5.8}$$

(2) Rarefaction Coefficient Simplification

As is noted in Eq. 5.2, the rarefaction coefficient is expressed in terms of trigonometric function and three empirical parameters which are mathematically complicated. Given the rarefaction coefficient coupling with the weight of viscous flow term, the mass flux formula (i.e., Eq. 5.4) turns out to be highly nonlinear, and the nonlinearity may increase the instability for large-scale

simulations. Therefore, a simple correlation with satisfying accuracy is desired to facilitate the computation of rarefaction correction term.

Based on the hypothesis of stratified model, the viscous flow term contributes to total flow performance in continuum, slip, and transition flow regime. Accordingly, the rarefaction coefficient (i.e., α) and rarefaction correction term (i.e., ϑ) are plotted against Knudsen number. Figure 5.1a shows that the analytical results of rarefaction coefficient (i.e., black dots) produced by Eq. 5.2 can be correlated by the new empirical correlation (i.e., blue curve) without any additional coefficients.

$$\alpha = 0.128\ln(Kn) + 1.120 \tag{5.9}$$

As indicated by the comparison with analytical results, the present equation yields an accurate correlation from Knudsen number 0.0002 to 6.0 with a regression R-squared value of 0.99 and an average relative error of 9.33%. Figure 5.1b shows that the rarefaction correction term using Eq. 5.9 (i.e., blue curve) can reproduce the analytical results with a regression R-squared value of 1.00 and an average relative error of 0.85%. Hence, the present expression is more suitable than the analytical equation given by Karniadakis et al. (2005) for the sake of simplicity.

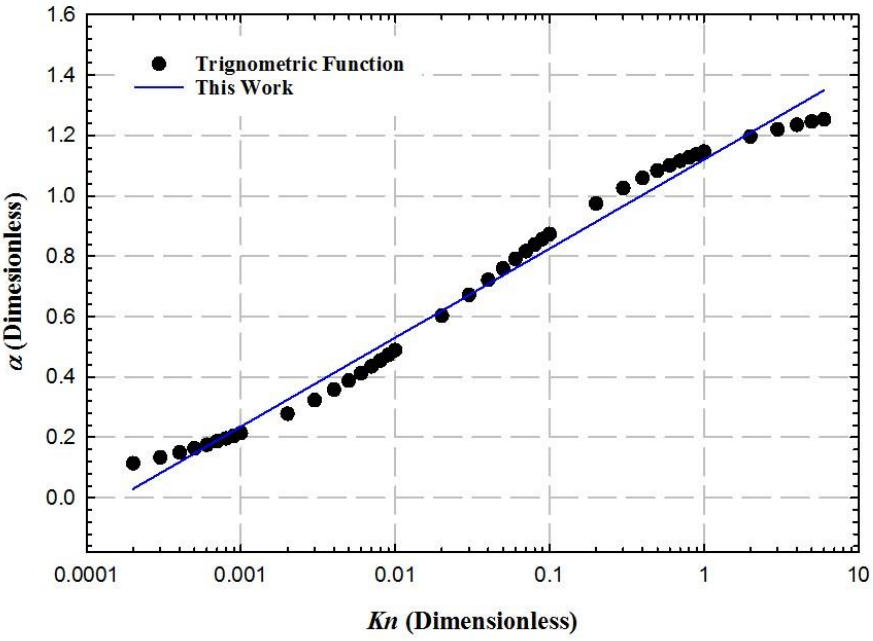

(*a*)

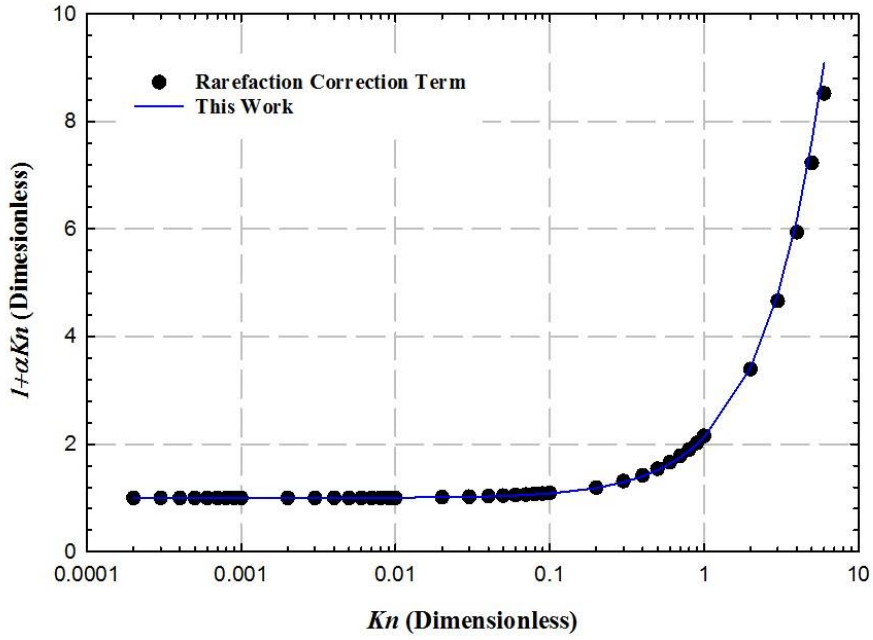

(*b*)

Figure 5.1: Empirical correlation of (a) rarefaction coefficient and (b) rarefaction correction term with Knudsen number. The black dots indicate the analytical results obtained by trigonometric function and rarefaction correction term, respectively. The blue curves indicate the empirical results obtained by regression.

(3) Multilayer Adsorption and Simplified Surface Diffusion Model

The rarefied gas model is insufficient to describe the shale gas flow because of multiple physical mechanisms under high reservoir pressures and limited transport space in shale matrix. Hence, a more realistic model is developed in this section considering multilayer adsorption, surface diffusion, and confinement effect. Various results from experiments and MD simulations have confirmed that the multilayer adsorption is formed in nanopores under high pressures and temperatures, which generate density fluctuations near the wall (Didar and Akkutlu, 2013; Yu et al., 2019). Furthermore, it is reported that adsorbed gas molecules can move along the wall due to concentration gradient (Riewchotisakul and Akkutlu, 2016). Such phenomenon is known as surface diffusion of which mass flux, F_s, can be formulated as (Xiong et al., 2012)

$$F_s = -D_s \nabla C_s \tag{5.10}$$

where D_s is surface diffusion coefficient, C_s is concentration gradient of adsorbents defined by $C_s = \rho_{sc} \rho_r V_s$. ρ_{sc} is gas density at standard condition, ρ_r is shale rock density, V_s is volume of adsorbents per unit rock mass.

It is imperative to improve the surface diffusion formula (i.e., Eq. 5.10) by coupling the density profile of multilayer adsorption. Results from the MD simulation in Figure 5.2a show that there are three methane adsorption layers (each layer has thickness of one methane molecule size) on each side of nanocapillary with pore size of 3.04 nm at 4,000 psi and 180°F (Didar and Akkutlu, 2013). The discrete profile exhibits damped oscillations from the highest value on the wall to the lowest one in the center where viscous flow and Knudsen diffusion are in presence. Hence, it is natural to simulate the surface diffusion incorporating BET isotherm model due to the distribution of multilayer adsorption (Alnoaimi and Kovscek, 2013). However, the application of BET model

involves significantly complicated calculations of the concentration gradient which makes the simulation highly impractical. To facilitate the computation of surface diffusion model, multilayer density profile can be transformed to the equivalent monolayer density profile as shown in Figure 5.2b (Wasaki and Akkutlu, 2015; Riewchotisakul and Akkutlu, 2016). Subsequently, the mass flux of surface diffusion can be determined by the monolayer Langmuir model expressed by $V_s = (\overline{P}V_L)/(\overline{P}+P_L)$, where V_L is Langmuir volume, P_L is Langmuir pressure. Nonetheless, Figure 5.2b demonstrates that such shift from multilayer to monolayer profile is inappropriate because the available volume for viscous flow and Knudsen diffusion is overestimated. Thus, a simplified surface diffusion model is proposed in Figure 5.2c, where the radius of flow zone of viscous flow and Knudsen diffusion, r_s, is unchanged while the multilayer adsorption is simplified to the monolayer adsorption by the method of Wasaki and Akkutlu (2015). Note that an effective radius (i.e., r_e) is defined to constrain the simplified surface diffusion zone, which is given as $r_e = r_o - d_m$. Then, the surface diffusion mass flux, F_s^n, can be calculated based on the simplified density structure and Langmuir model as follows.

$$F_s^n = -\frac{\pi\left(r_o^2 - r_e^2\right)}{\pi r_o^2} D_s \rho_{sc} \rho_r \nabla\left(\frac{\overline{P}V_L}{\overline{P}+P_L}\right) \tag{5.11}$$

In addition, the radius of flow zone of viscous flow and Knudsen diffusion in Figure 5.2c can be modified as $r_s = r_o - x\, d_m$ where d_m is molecular size and x is the number of adsorption layers.

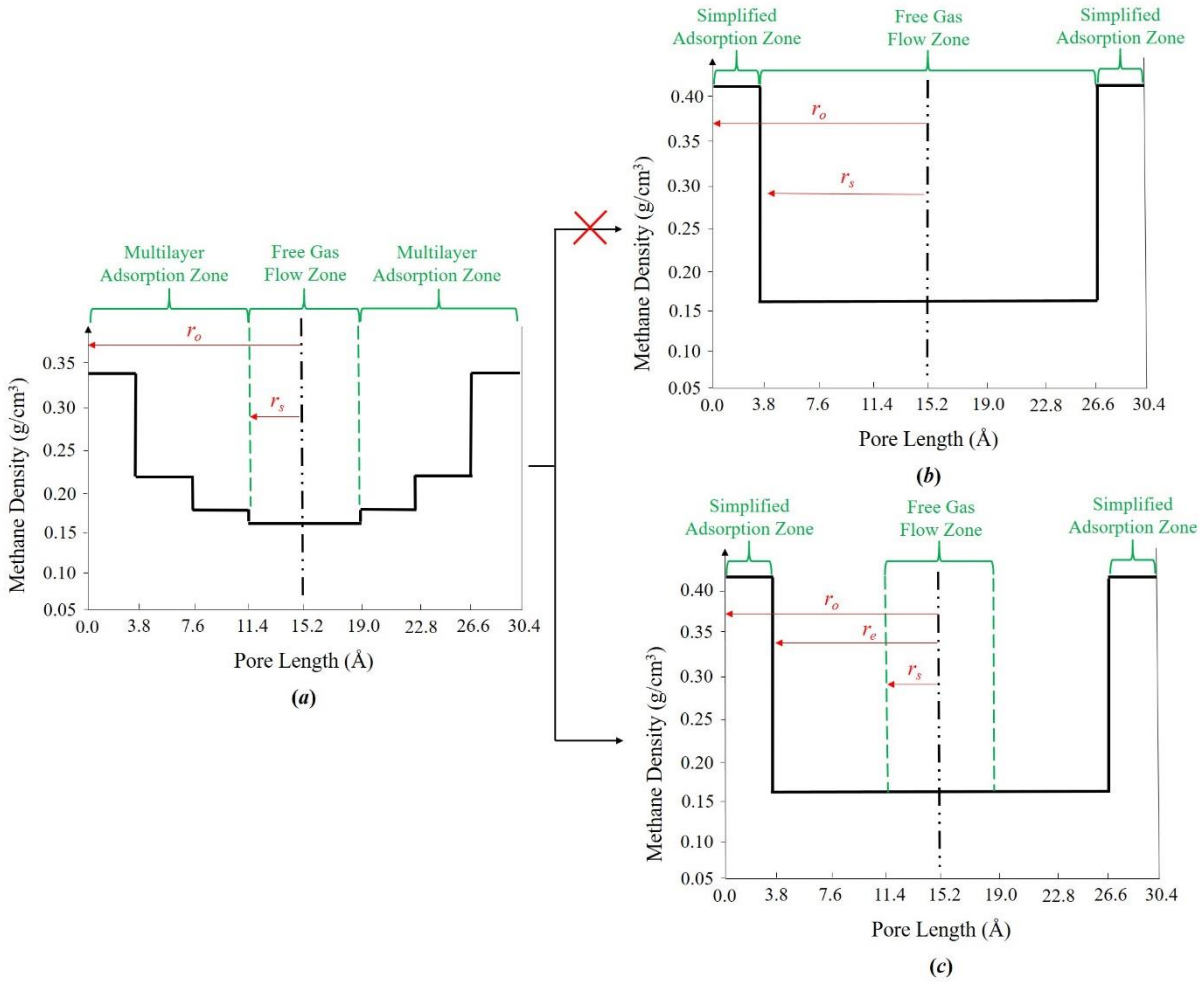

Figure 5.2: Shale gas discrete density profile in the nanopore with size of 3.04 nm at 4,000psi and 180°F: (a) discrete density profile with three adsorption layers; (b) inappropriate simplified density profile with monolayer adsorption; (c) appropriate simplified density profile with monolayer adsorption.

(4) Apparent Permeability of Shale Gas Flow

Due to the presence of multilayer adsorption, the critical radius is updated to the expression $r_c = r_s\sqrt{1-\exp\left(-\theta/Kn_r\right)}\Big/\sqrt{\hbar}$ where Kn_r is Knudsen number for real gas modified as $Kn_r = \mu_r\sqrt{\pi ZRT/\left(2M\right)}\Big/\bar{P}r_s$. Hence, the apparent permeability for shale gas in homogeneous matrix, i.e., k_{tr}, can be derived as,

$$
\begin{aligned}
k_{tr} &= k_{vr}^{n} + k_{kr}^{n} + k_{sr}^{n} \\
&= \frac{\phi}{\tau} w_{vr} \vartheta_r \frac{r_s^4}{8 r_o^2} + \frac{\phi}{\tau} w_{kr} \frac{2 r_s^3}{3 r_o^2} \mu_r \Omega \sqrt{\frac{8ZRT}{\pi M}} \\
&+ \frac{\phi}{\tau} w_{sr} D_s \mu_r \frac{\rho_{sc} \rho_r V_L P_L RT}{M} \Omega \left(\frac{Z}{\bar{P} + Z P_L} \right)^2
\end{aligned}
\tag{5.12}
$$

$$
w_{vr} = \frac{1}{\hbar}\left[1 - \exp\left(-\frac{\theta}{Kn_r}\right)\right]\left\{2 - \frac{1}{\hbar}\left[1 - \exp\left(-\frac{\theta}{Kn_r}\right)\right] + \frac{4Kn_r}{1+Kn_r}\right\} \tag{5.13}
$$

$$
w_{kr} = \left\{1 - \frac{1}{\hbar}\left[1 - \exp\left(-\frac{\theta}{Kn_r}\right)\right]\right\}^2 \tag{5.14}
$$

$$
w_{sr} = 1 - \frac{r_e^2}{r_o^2} \tag{5.15}
$$

where k_{vr}^{n}, k_{kr}^{n}, and k_{sr}^{n} is the real gas apparent permeability for viscous flow in central zone, Knudsen diffusion in middle annular zone and surface diffusion in outer annular zone, respectively. Ω is defined as $\Omega = 1/\bar{P} - \left(dZ/dP\right)/Z$, and ϑ_r is modified as $\vartheta_r = 1 + \alpha_r Kn_r$. Similarly, the flow rate for shale gas in nanocapillary, Q_{tr}, can be calculated by

$$
\begin{aligned}
Q_{tr} &= \frac{\phi}{\tau} w_{vr} \vartheta_r \frac{\pi r_s^4}{8\mu_r} \nabla P + \frac{\phi}{\tau} w_{kr} \frac{2}{3} \pi r_s^3 \Omega \sqrt{\frac{8ZRT}{\pi M}} \nabla P \\
&+ \frac{\phi}{\tau} w_{sr} \pi r_o^2 D_s \frac{\rho_{sc} \rho_r V_L P_L RT}{M} \Omega \left(\frac{Z}{P + Z P_L} \right)^2 \nabla P
\end{aligned}
\tag{5.16}
$$

Note that the real gas effect and confinement effect have been considered in the model using the Eqs. 4.17-4.24.

5.2.2 Numerical Simulation of Shale Gas Flow at Core Scale

It is widely accepted that the momentum conservation equation in matrix can be quantified incorporating the flow model in nanocapillary as follows.

$$\frac{\partial}{\partial t}(\rho\phi)+\frac{\partial}{\partial t}\left[(1-\phi)q\right]=-\nabla\cdot\left(\rho\vec{u}\right)+\rho Q \tag{5.17}$$

where ρ is gas density, q is adsorbate mass per rock volume which is defined as $q=\rho_{sc}\rho_r\overline{P}V_L/\left(\overline{P}+ZP_L\right)$. Q is sink/source term per unit volume. $\vec{u}$ denotes fluid velocity vector which can be expressed as

$$\vec{u}=-\frac{1}{\mu}\mathbf{K}\cdot\left(\nabla P-\rho g\nabla H\right) \tag{5.18}$$

where $\mathbf{K}$ is permeability tensor. H can be denoted as the elevation with direction of positive downward. Then, Eq. 5.17 can be rearranged as follows (see detailed expansions in Appendix D).

$$\frac{\partial}{\partial t}(\rho\phi)+\frac{\partial}{\partial t}\left[(1-\phi)q\right]=\nabla\cdot\left(\frac{\rho}{\mu}\mathbf{K}\right)\cdot\nabla P+\nabla\nabla P:\left(\frac{\rho}{\mu}\mathbf{K}\right)+\nabla\cdot\left[\frac{\rho^2 g}{\mu}\mathbf{K}\cdot(\nabla H)\right]+\rho Q \tag{5.19}$$

In this work, it is assumed that shale gas flows along the horizontal direction in the core, thus one-dimensional spatial-temporal formula can be applied to simulate the gas transport through the core at various locations. Moreover, the gravity term can be neglected and the permeability tensor can be regarded as the scalar because the vertical permeability is extremely low in shale matrix. Also, the source/sink term is omitted. Hence, Eq. 5.19 is further organized as the following expression.

$$\frac{\partial}{\partial t}(\rho\phi)+\frac{\partial}{\partial t}\left[(1-\phi)q\right]=\nabla\cdot\left(\frac{\rho}{\mu}k_{tr}\right)\cdot\nabla P+\nabla\nabla P:\left(\frac{\rho}{\mu}k_{tr}\right) \tag{5.20}$$

Eq. 5.20 can be simplified by coupling Eqs. 5.12-5.15 as follows.

$$\frac{\partial}{\partial t}(\rho\phi)+\frac{\partial}{\partial t}\left[(1-\phi)q\right]=\nabla\left(\frac{\rho}{\mu}k_{tr}\right)\cdot\nabla P+\left(\frac{\rho}{\mu}k_{tr}\right)\nabla^2 P \tag{5.21}$$

$$\left[\rho\phi c_1+(1-\phi)qc_2\right]\frac{\partial P}{\partial t}=\frac{\partial}{\partial x}\left(\frac{\rho}{\mu}k_{tr}\frac{\partial P}{\partial x}\right) \tag{5.22}$$

where c_1 can be expressed as $c_1=c_\rho+c_\phi$ where c_ρ and c_ϕ is the compressibility term for density and porosity as $c_\phi=(1/\phi)\partial P/\partial\phi$ and $c_\rho=(1/\rho)\partial P/\partial\rho$. c_2 is written as $c_2=ZP_Lc_\rho/(P+ZP_L)-\phi/(1-\phi)c_\phi$. Due to the stress effect in the shale formation, the porosity can be influenced which is characterized as the following correlation (Wu et al., 2016)

$$\phi=\phi_0\left(\frac{p_e}{p_0}\right)^{-cc} \tag{5.23}$$

$$p_e=p_c-\alpha\overline{P} \tag{5.24}$$

$$r_o=r_{ini}\left(\frac{p_e}{p_0}\right)^{0.5(cc-ss)} \tag{5.25}$$

where p_e is effective pressure, p_c is confining pressure, p_0 is standard pressure (i.e., 1 atm), *cc* is shale porosity coefficient ranging from 0.006 to 0.046. *ss* is shale intrinsic permeability coefficient ranging from 0.196 to 1.013. $\overline{P}$ is pore pressure, ϕ_0 is porosity under unloading condition, r_{ini} is radius under unloading condition, α is Biot coefficient ranging from 0.15 to 0.85. Hence, c_ϕ can be rearranged as follows.

$$c_\phi=\frac{cc\cdot\alpha}{p_c-\alpha\overline{P}} \tag{5.26}$$

According to Eqs. 5.12-5.15, the apparent permeability is incorporated in Eq. 5.22 for the simulation. Eq. 5.22 is discretized implicitly due to the stable performance while the central difference and the backward difference schemes are utilized for the spatial and temporal discretization, respectively (Appendix E). The initial condition is shown in Eq. 5.27 whereas the Dirichlet boundary conditions (pressure specified boundary) are given in Eq. 5.28.

$$I.C. \quad P_x|_{0\le x\le L, t=0} = P_{ini} \tag{5.27}$$

$$S.T. \quad P_x^t|_{x=0, t>0} = P_{in}, \; P_x^t|_{x=L, t>0} = P_{out} \tag{5.28}$$

where P_{in} and P_{out} are the specified pressures at inlet and outlet, respectively. P_{ini} is initial pressure across the core.

5.2.3 Application in Pulse-Decay Test

The pulse-decay test can be utilized to determine the petrophysical properties of the shale core by triggering a series of pressure pulses through the tight cores. As the gas flows through the core from the upstream to downstream pressure chamber, one-dimensional steady and unsteady-state simulation can be implemented based on the Eqs. 5.17-5.28. Since the inlet and outlet pressures change with time in the test, two empirical correlations for the inlet and outlet pressures are adopted, which are given as (Barral et al., 2010; Civan et al., 2011)

$$P_{in} = P_{in\_eq} + \left(P_{in\_ini} - P_{in\_eq}\right)\exp\left(-\psi_{in} t\right) \tag{5.29}$$

where P_{in_eq} denotes the inlet pressures under equilibrium condition. P_{in_ini} denotes the inlet pressures under the initial condition. ψ_{in} is the reciprocal-characteristic time for the inlet. Subsequently, the implicit finite difference scheme is used to solve the partial difference equations

for the methane transport through the core due to its unconditionally stable performance. More specifically, the block-center discretization and backward difference approximation are taken for the spatial and temporal term, respectively. The shale core with length of 5.0 cm is equally divided into 100 blocks and the simulation time increases 15 seconds per time step. Note that the outlet pressure remains constant in the simulation. The detailed simulation parameters are listed in Table 5.3.

5.3 Results and Discussion

In this work, the validations are made in straight capillaries. The rarefied gas model in a straight capillary (Eqs. 5.7-5.8) is tested with experimental and simulated dimensionless mass fluxes of five types of gases including argon, helium, methane, nitrogen, and oxygen collected from various literatures (Loyalka and Hamoodi, 1990; Tison, 1993; Ewart et al., 2007; Perrier et al., 2011; Yamaguchi et al., 2011). The shale gas model in straight nanocapillary (Eq. 5.16) is verified against the methane flow rate data from Yu et al. (2019). More particularly, Yu et al. (2019) adopted non-equilibrium MD simulation (NEMD) to simulate the gas flow considering monolayer adsorption and surface diffusion from 5.0 to 45.0 MPa under reservoir conditions. The detailed parameters in validations are tabulated in Table 5.1 and 5.2, respectively.

Table 5.1: Summary of parameters used in rarefied gas model validations

Gas Type	θ^*	$\hbar^*$	Literatures
Argon	1.62	0.67	Ewart et al., 2007 Perrier et al., 2011 Yamaguchi et al., 2011
Helium	1.54	0.91	Tison, 1993 Ewart et al., 2007 Perrier et al., 2011
Methane	1.20	2.17	Loyalka and Hamoodi, 1990
Nitrogen	1.54	0.69	Ewart et al., 2007 Perrier et al., 2011 Yamaguchi et al., 2011
Oxygen	1.54	0.67	Yamaguchi et al., 2011

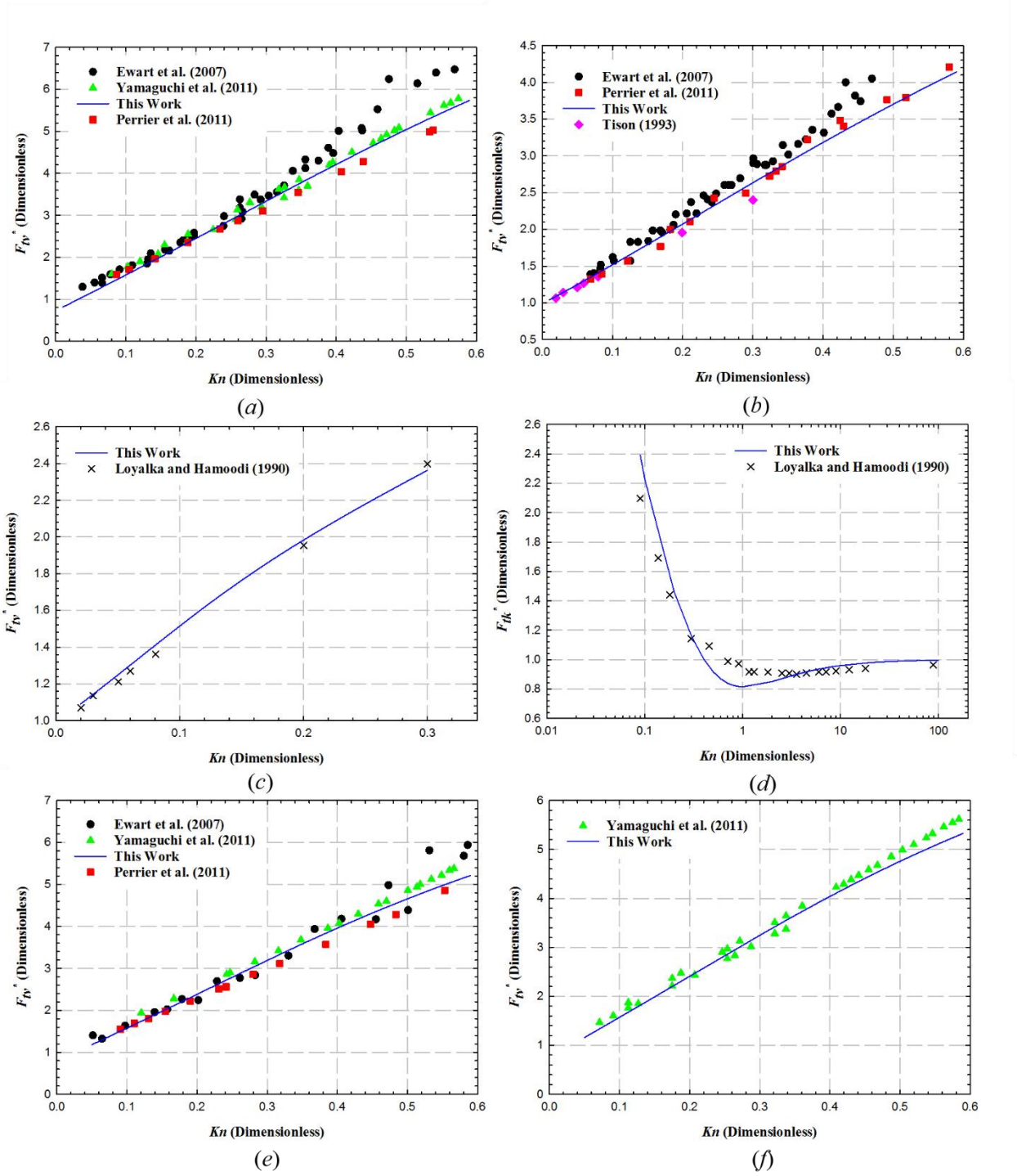

Figure 5.3: Collected and calculated dimensionless mass fluxes versus Knudsen number for the validation of rarefied gas model in straight capillary. Five types of gases are used for validation including (*a*) argon, (*b*) helium, (*c*) and (*d*) methane, (*e*) nitrogen, and (*f*) oxygen.

Table 5.2: Summary of parameters used in shale gas model validations

Validation in nanocapillary	Symbol	Unit	Values
Optimized chemical confinement parameter	θ^*	dimensionless	1.20
Optimized velocity direction heterogeneity parameter	$\hbar^*$	dimensionless	2.17
Optimized surface diffusivity coefficient	D_s^*	m^2/s	8.80×10^{-6}
Optimized Langmuir pressure	P_L^*	Pa	13.79×10^{6}
Optimized Langmuir volume	V_L^*	m^3/kg	3.12×10^{-3}
Reservoir temperature	T	K	298.00
Universal gas constant	R	J/mol/K	8.314
Nominal methane molecule size	d_m	nm	0.38
Methane molar mass	M	kg/mol	0.016
Methane critical pressure	P_c	Pa	1.00×10^{6}
Methane critical temperature	T_c	K	190.60
Number of adsorbed layers	x	dimensionless	1
Shale grain density	ρ_r	kg/m^3	2659.06
Methane density at standard condition	ρ_{sc}	kg/m^3	0.68
Capillary radius	r_o	nm	3/5/8
Methane acentric factor	ω	dimensionless	0.01

Figure 5.3 shows the calculated and collected dimensionless mass fluxes versus Knudsen number for five types of gases in a straight capillary. Note that the collected dimensionless mass flux in Figure 5.3d is validated by Eq. 5.8, which extends from late slip flow to free molecular flow ($0.09 \le Kn \le 89.08$). Meanwhile, other subfigures correspond to Eq. 5.7 which covers from early slip flow to early transition flow ($0.02 \le Kn \le 0.58$). It is seen that the rarefied gas model can accurately reproduce the reference data for each type of gases over entire flow regimes. The scattered data in other subfigures nearly exhibit the linear correlation with the Knudsen number, which implies the dominant performance of viscous flux in early slip flow and early transition flow regime. Furthermore, the calculation of dimensionless mass fluxes involves the estimation of empirical parameters $\hbar$ and Θ for each type of gases. Thus, the genetic algorithm (GA) optimization is

utilized to acquire the optimal $\hbar^*$ and θ^* with physical bounds $\hbar \geq 1-\exp\left(-\theta/Kn_r\right)$ and $0<\theta\leq\sqrt{r_o^2+l^2}\,/r_o$, respectively. Various groups of optimal $\hbar^*$ and θ^* are collected corresponding to different types of gases, thus the optimal parameters can be directly used for the complicated simulations based on the developed rarefied gas model. Figure 5.4 presents the collected versus calculated methane flow rate for the validation of shale gas model in straight nanocapillary with various sizes of 6 nm, 10 nm, and 16 nm. The diagonal line match each other with coefficient of determination $R^2=1$ indicating that the Eq. 5.16 satisfies the NEMD data. Furthermore, the optimal $\hbar^*$ and θ^* for methane gas in Table 5.2 are selected for the simulation of shale gas model, while D_s , P_L , V_L are optimized by GA with physical constraints $1.0\times10^{-9}\leq D_s\leq 8.8\times10^{-6}$ (Akkutlu and Fathi, 2012), $3.68\times10^{6}\leq P_L\leq 2.34\times10^{7}$, and $8.5\times10^{-4}\leq V_L\leq 5.0\times10^{-3}$ (Kang et al., 2011), respectively.

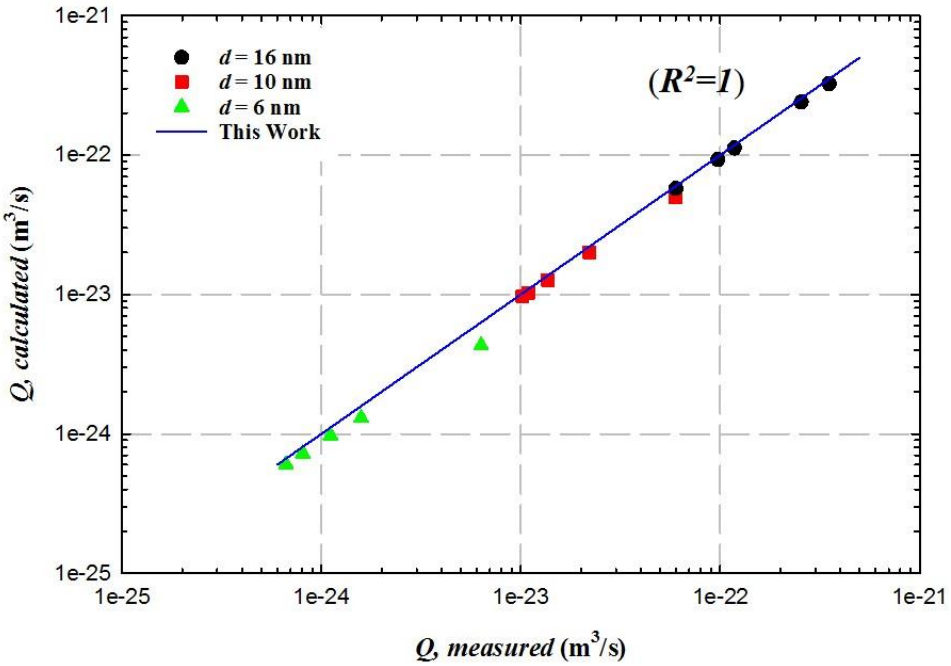

Figure 5.4: Collected versus calculated methane flow rate for the validation of shale gas model in straight nanocapillary with different sizes. The diagonal line indicates exact agreement.

Table 5.3: Summary of parameters used in shale core simulation

Parameters	Symbol	Unit	Values
Chemical confinement parameter	θ	dimensionless	0.46
Velocity direction heterogeneity parameter	h	dimensionless	0.9
Surface diffusivity coefficient	D_s	m^2/s	8.80×10^{-6}
Equilibrium pressure	P_{eq}	Pa	1.20×10^{5}
Initial pressure	P_{ini}	Pa	5.00×10^{5}
Reservoir temperature	T	K	298/314
Simulation duration	t	s	3000
Confining pressure	Pc	nm	0.38
Biot coefficient	α	dimensionless	0.5
Tortuosity	τ	dimensionless	2
Porosity	ϕ	dimensionless	0.1
Number of adsorbed layers	x	dimensionless	1
Porosity coefficient	cc	dimensionless	0.03
Permeability coefficient	ss	dimensionless	0.5
Capillary radius	r_o	nm	100
Reciprocal-characteristic time	ψ_{in}	dimensionless	0.001

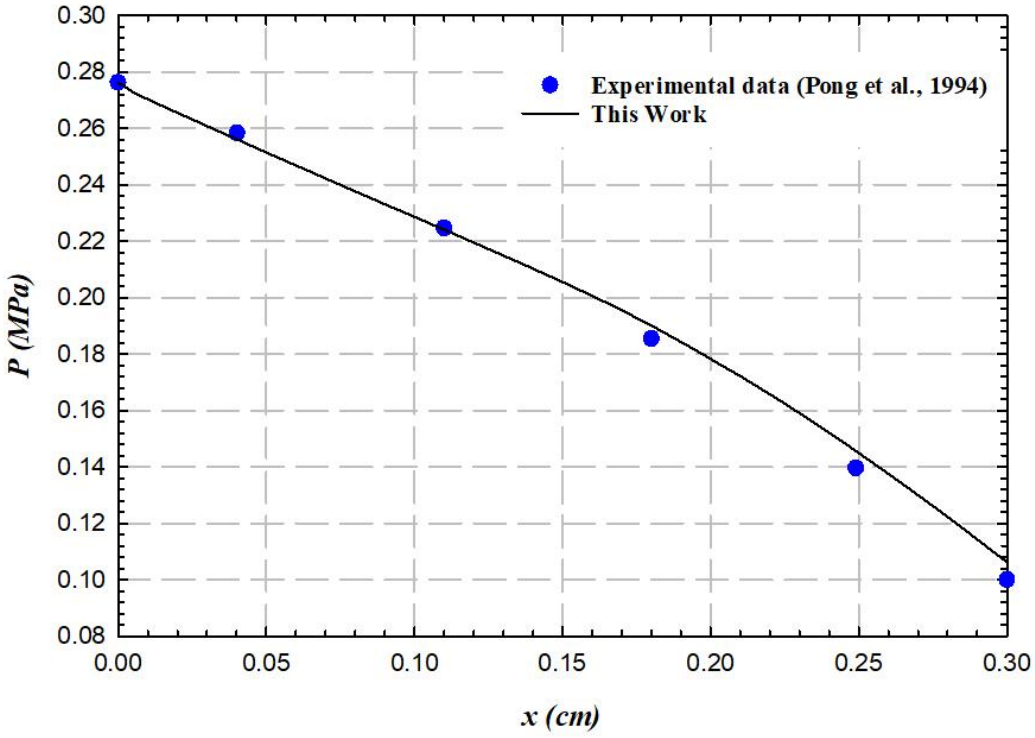

Figure 5.5: Collected and simulated pressures for the validation of shale gas steady-state flow in the core.

Figure 5.5 shows the validation result of steady-state analysis based on Eqs. 5.17-5.28. Pong et al. (1994) provided the pressure profile across the micro-channel under equilibrium conditions. The blue dots indicate the simulated pressures at six different spots in the micro-channel with inlet pressure of 0.275 MPa, outlet pressure of 0.101 MPa, and temperature of 314K. It is seen that the simulated results fit the experimental data satisfactorily. Figure 5.6 illustrates the unsteady-state pressure variations along the core with different simulation durations from 1 to 50 minutes. It is seen that the pressure declines with the increase of distance for each curve while the inlet pressure drops from 0.48 to 0.14 MPa with the increase of the simulation duration. Moreover, the decline rate gradually decreases with the time until the steady state is reached.

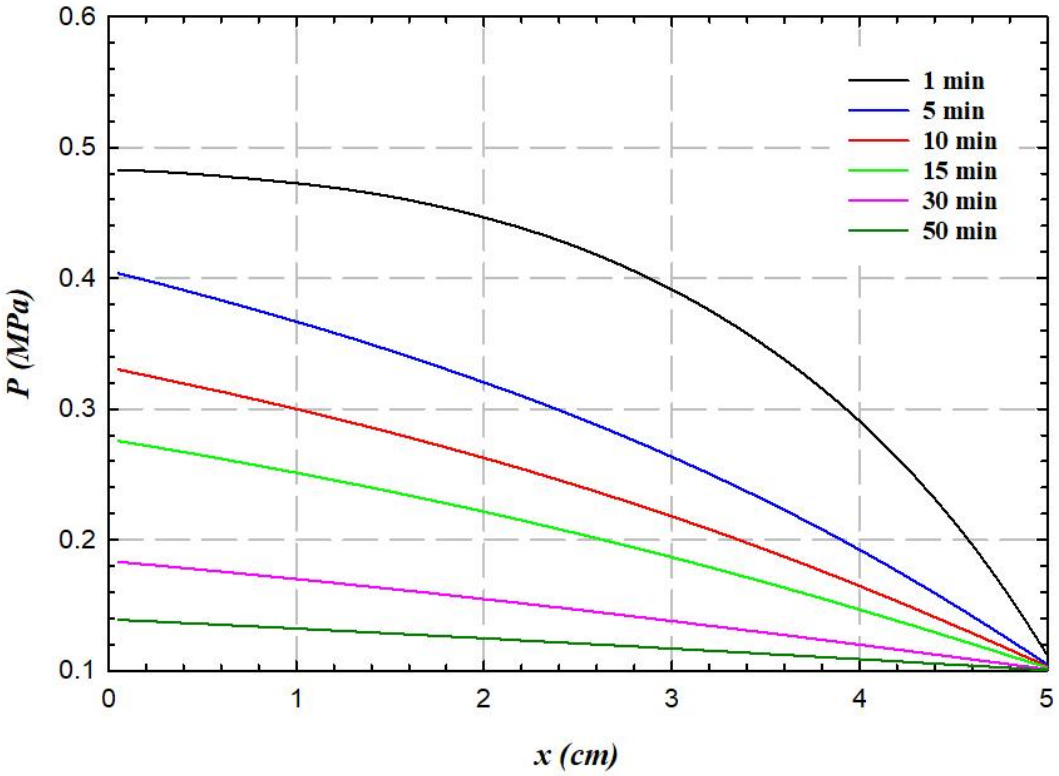

Figure 5.6: Simulated pressures across the shale core with different durations.

5.4 Summary

This work has improved the shale gas apparent permeability model and upscaled the model from nanopores to the shale core scale by the numerical method. Moreover, multiple mechanisms are incorporated and simplified to facilitate the simulation. It is found that the rarefaction in nanopores is justified to be represented by the weighted Knudsen diffusion and slip flow. Also, the weights in proposed model are parameterized with Knudsen numbers which are flexible to describe the flow behavior in different flow regimes. Moreover, the numerical method can be applied for the pulse-decay test to calculate the petrophysical properties. In addition, the unknown shale properties can be estimated by the optimization method based on the numerical scheme.

CHAPTER 6: GAS TRANSPORT IN HETEROGENEOUS SHALE MATRIX BASED ON FRACTAL THEORY AND FUZZY STATISTICAL METHOD

6.1 Introduction

The organic-rich shale matrix is featured with multiscale pore sizes ranging from nanometers to micrometers, which leads to strong heterogeneities in the prediction of gas apparent permeability (AP) and production. A better quantification of such flows in complex pore network has been hampered by the scarcity of relevant studies. Most of existing studies focusing on the gas flow in heterogeneous coal and shale matrix, unfortunately, have not comprehensively discussed the heterogeneity impact on gas flow in micro/nano-scale matrix (Smith and Williams, 1984; Weida et al., 2005; Fathi and Akkutlu, 2009; Akkutlu and Fathi, 2012; Akkutlu, et al., 2015; Ghanbarian and Javadpour, 2017). It results in limited, incomplete, and even contradictive conclusions.

The fractal theory has been widely used to quantify the heterogeneity degree in porous medium due to the fractal characteristics of structural parameters (Wang, et al. 2018; Sheng et al., 2019). Geng et al. (2016) adopted the fractal model to characterize the real gas transport in heterogeneous matrix due to the changing pore sizes and tortuosity. Furthermore, it is found that naturally fractured reservoirs present the patterns of fractal distribution (Flamenco-Lopez and Camacho-Velazquez, 2001). You et al. (2019) applied the fractal model to the hydraulic fracture networks based on the observation that fracture network resembles the characteristics of fractal distribution. Fuzzy theory is initially proposed by Zadeh (1965) to replace the conventional binary logic sets. Also, the fuzzy statistical method is an effective tool for modeling complex mathematical problems with uncertain parameters such as seismic analyses, artificial neural networks, and lithology identifications (Nikravesh and Aminzadeh, 2001; Long et al., 2016; Katz et al. 2019). You et al.

(2019) first employed the fuzzy nearness and the fuzzy statistical method to quantify the hydraulic fracture heterogeneity. However, it is challenging to evaluate the uncertainties introduced by structural parameters in fractal theory.

In this work, an analytical AP model is first developed to describe the shale gas rarefied flow in a single nanocapillary coupling various flow mechanisms such as real gas effect, adsorption, and surface diffusion. According to the fractal theory, the nanocapillary is upscaled to the unit matrix block where total AP is integrated by those of various nanocapillaries characterized by structural parameters (i.e., pore-size and fractal dimensions) with normal distributions. Then, the dual-porosity system is utilized to couple the shale matrix and hydraulic fracture for the gas production rate simulation where the governing diffusivity equation is used in each unit matrix block. Subsequently, the fuzzy statistical method is adopted to evaluate the uncertainty induced by the fractal structural parameters: the optimization is first applied to acquire the satisfactory structural parameters for the homogeneous model, then the normal distribution is generated for each structural parameter. The Monte Carlo simulation is utilized to calculate the approximate fuzzy membership grade. Finally, the obtained production rate from the fuzzy statistical method is compared with that calculated by the homogeneous model.

6.2 Mathematical Formulation

6.2.1 Shale Gas Flow in Fractal Shale Matrix Blocks

Singh et al. (2014) have indicated that the gas rarefaction in nanopores can be characterized by the linear superposition of the convective flow and Knudsen diffusion. The convective flow is represented by the Hagen-Poiseuille equation as follows.

$$M_c = \frac{\bar{P}M}{ZRT}\frac{\pi r_o^4}{8\mu}\frac{\Delta P}{L} \tag{6.1}$$

where R is universal gas constant, T is temperature, $\bar{P}$ is pressure, M is molar mass, r_o is pore radius, μ is viscosity, ΔP is pressure difference along the capillary, M_c is convective mass flux. Accordingly, the Knudsen diffusion mass flux can be expressed by

$$M_k = \frac{2\pi r_o^3}{3} P\Omega\sqrt{\frac{8M}{\pi ZRT}}\frac{\Delta P}{L} \tag{6.2}$$

where Ω denotes the gas compressibility factor as $\Omega = 1/\bar{P} - (dZ/dP)/Z$, M_k is Knudsen diffusion mass flux. The monolayer surface diffusion equation can be written as

$$M_s = \pi r_o^2 D_s C_{a\max}\frac{PMZP_L\Omega}{\left(\bar{P}+ZP_L\right)^2}\frac{\Delta P}{L} \tag{6.3}$$

where D_s denotes surface diffusion coefficient, P_L is Langmuir pressure, $C_{a\max}$ is maximum adsorption capacity. $C_{a\max}$ can be expressed by $C_{a\max} = \left(V_L\rho_{STG}\rho_{rock}\right)/M$, where V_L is Langmuir volume indicating the maximum adsorbed phase volume per unit total grain mass, ρ_{STG} is gas density at standard condition, ρ_{rock} is shale rock density (Wasaki and Akkutlu, 2015). Moreover, the real gas effect is significant under the condition of high pressures and temperatures. Hence, the real gas effect can be quantified by the Z-factor and real gas viscosity correlation. Mahmoud (2013) developed a novel correlation for the high-pressure condition as follows.

$$Z = 0.702e^{-2.5T_r}P_r^2 - 5.524e^{-2.5T_r}P_r + 0.044T_r^2 - 0.164T_r + 1.15 \tag{6.4}$$

where P_r denotes reduced pressure expressed by $P_r = \bar{P}/P_c$, P_c denotes critical pressure, T_r denotes reduced temperature as $T_r = T/T_c$, and T_c denotes critical temperature. In addition, the real

gas viscosity can be established by the Sutton's model by the following expression (Sutton, 2007; Jia et al., 2018b),

$$\mu_r = 10^{-7}\mu \exp\left[X\left(\frac{\rho}{1000}\right)^{Y}\right] \tag{6.5}$$

$$\mu\vartheta = 0.807T_r^{0.618} - 0.357\exp\left(-0.449T_r\right) + 0.340\exp\left(-4.058T_r\right) + 0.018 \tag{6.6}$$

$$\vartheta = \frac{0.949\left(1.8T_c\right)^{(1/6)}}{\left(0.145\times10^{-3}P_c\right)^{(2/3)}\sqrt{1000M}} \tag{6.7}$$

where μ_r denotes real gas viscosity, ρ is density written as $\rho=\left(\bar{P}M\right)/\left(ZRT\right)$. Y can be written as $Y=1.66378-0.04679X$ where X is equal to $X=3.47+1588/\left(1.8T\right)+0.9M$. The fractal theory is applied to upscale each flow mechanism from the capillary to the unit matrix block. As is known that the fractal scaling law can be written as (Wang et al., 2017; Chai and Li, 2020)

$$N(size \geq r) = \left(\frac{r_{\max}}{r}\right)^{D_f} \tag{6.8}$$

where *N* denotes the cumulative pore size distribution, $r_{\max}$ is the largest pore size, D_f is the fractal dimension for the pore size distribution. Furthermore, the realistic length of a tortuous capillary in the unit matrix block, *L*, can be expressed by the fractal scaling law as (Geng et al., 2016)

$$L = L_o^{D_T} r^{(1-D_T)} \tag{6.9}$$

where L_o denotes straight length of the unit matrix block, D_T is fractal dimension for the tortuosity in unit matrix block. Subsequently, total mass flux for the unit matrix block can be quantified as

$$M^T = -\int_{r_{\min}}^{r_{\max}} \left(M_c + M_k + M_s\right) dN \tag{6.10}$$

The apparent permeability including the convective flow, the Knudsen diffusion, and the surface diffusion can be developed based on Eqs. 6.1-6.10, which is shown as follows.

$$\begin{aligned} k_{app} = & \frac{\pi D_f r_{\max}^{(3+D_T)}}{8L_o^{(D_T-1)}\left(3+D_T-D_f\right)S}\left[1-\left(\frac{r_{\min}}{r_{\max}}\right)^{\left(3+D_T-D_f\right)}\right] \\ & + \frac{2\pi\mu_r D_f r_{\max}^{(2+D_T)}}{3\phi L_o^{(D_T-1)}\left(2+D_T-D_f\right)S}\sqrt{\frac{8ZRT}{\pi M}}\left[1-\left(\frac{r_{\min}}{r_{\max}}\right)^{\left(2+D_T-D_f\right)}\right] \\ & + \frac{\pi\mu_r D_f D_s r_{\max}^{(1+D_T)}}{L_o^{(D_T-1)}\left(1+D_T-D_f\right)S} C_{a\max}\frac{Z^2 P_L \Omega RT}{\left(\bar{P}+ZP_L\right)^2}\left[1-\left(\frac{r_{\min}}{r_{\max}}\right)^{\left(1+D_T-D_f\right)}\right] \end{aligned} \tag{6.11}$$

where k_{app} denotes total apparent permeability for the unit matrix block, S is cross-section area which can be written as $\pi D_f r_{\max}^2 (1-\phi)/\left[\phi\left(2-D_f\right)\right]$.

6.2.2 Shale Gas Flow in Fractured Formation

The dual-porosity system is applied to represent the hydraulic-fractured shale matrix. To simplify the complex matrix-fracture system and ease the expensive computations, the two-dimensional sector model is utilized based on the work of Wasaki and Akkutlu (2015). Figure 6.1 shows the schematic configuration for the sector model. It is seen that the sector model is comprised of two parts: the rightmost square blocks from the top to bottom represent one wing of the hydraulic fracture where the dominant flow mechanism is viscous flow; the other square blocks represent

the shale matrix where the flow mechanisms are viscous flow, Knudsen diffusion, and surface diffusion. Note that it is assumed there is only one layer along the z-direction. In addition, one sink is set up in the right bottom block which is one of the hydraulic fracture blocks as well. The sink is designed to connect to the horizontal well in field production.

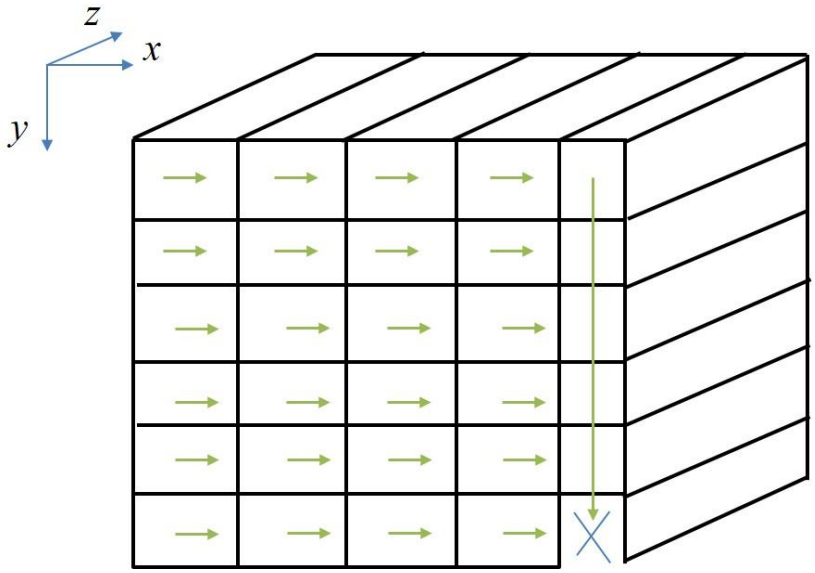

Figure 6.1: Schematic diagram of sector model including the shale matrix and the hydraulic fracture. The short green arrow indicates the flow direction from unit matrix block to the fracture. The long green arrow indicates the flow direction from the fracture to the well location.

Subsequently, the macroscale simulation is implemented based on the following diffusivity equation which has been described in Chapter 5.

$$\frac{\partial}{\partial t}(\rho\phi)+\frac{\partial}{\partial t}\left[(1-\phi)q\right]=\nabla\left(\frac{\rho}{\mu}k_{app}\right)\cdot\nabla P+\left(\frac{\rho}{\mu}k_{app}\right)\nabla^2 P \tag{6.12}$$

Note that Eq. 6.12 denotes the governing equation for the shale gas flow in each unit matrix block. For the hydraulic fracture, the second term on the left-hand side is neglected due to the absence of adsorption in the fracture (Wasaki and Akkutlu, 2015). Moreover, the porosity and the apparent permeability are replaced with the corresponding parameters for the hydraulic fracture on both

sides of Eq. 6.12. It is noted that the hydraulic fracture permeability is assumed as the constant value which is much larger than the permeability in the shale matrix, and only single-phase flow is considered in the matrix and fracture blocks. Eq. 6.12 can be further simplified in the two-dimensional flow regime as

$$\frac{\partial p}{\partial t}\left[\rho\phi C_1+(1-\phi)qC_2\right]=\frac{\partial}{\partial x}\left(\frac{\rho}{\mu}k_{app}\frac{\partial p}{\partial x}\right)+\frac{\partial}{\partial y}\left(\frac{\rho}{\mu}k_{app}\frac{\partial p}{\partial y}\right)+Q_{\sin k} \tag{6.13}$$

where C_1 can be expressed as $C_1=1/\bar{P}-\left(dZ/dP\right)/Z$, C_2 can be written as $C_2=P_L ZC_1/\left(\bar{P}+ZP_L\right)$, $Q_{\sin k}$ is the sink which is represented by

$$Q_{\sin k}=\frac{J_w\left(P_{i,j}-P_{wf}\right)}{\Delta V_b} \tag{6.14}$$

where P_{wf} is the bottom-flow pressure, ΔV_b is the bulk volume of the unit matrix block. J_w is the productivity index which is approximately characterized by the model of Aronofsky and Jenkins (1954) as the following expression.

$$J_w=-\frac{\pi k_{app}\rho h_w}{\mu_r\left[\ln\left(\frac{r_e}{r_w}\right)+s\right]} \tag{6.15}$$

$$r_e=\sqrt{0.5\mathbf{e}^{-\pi}\left(\Delta y^2+\Delta z^2\right)} \tag{6.16}$$

where h_w is the fracture width, s is skin factor, r_e and r_w is the effective well radius and true well radius, respectively. Next, Eq. 6.13 is discretized implicitly due to the stable performance, and the central difference scheme and the backward difference scheme are utilized for the spatial and temporal discretization, respectively. In addition, the no-flow barriers are assumed as the boundary condition. Subsequently, the pressures and the flow rate are calculated iteratively using the generalized minimal residual method which is an iterative method for solving the nonsymmetric

positive definite system of linear equations. Note that the harmonic average is used to calculate the fluid properties between the neighboring blocks whereas the cross flows between the shale matrix and hydraulic fracture are not considered in this work. The parameters are shown in the following Table 6.1.

Table 6.1: Summary of parameters used in macroscale simulation

Parameters	Symbol	Unit	Values
Porosity	ϕ	dimensionless	0.1/0.3
Molar mass	M	kg/mol	0.016
Surface diffusivity coefficient	D_s	m^2/s	1×10^{-9}
Langmuir pressure	P_L	Pa	2.98×10^{6}
Langmuir volume	V_L	m^3/kg	3.12×10^{-3}
Reservoir temperature	T	K	400.00
Universal gas constant	R	J/mol/K	8.314
Maximum pore radius	r_{max}	nm	250
Minimum pore radius	r_{min}	nm	2
Fractal dimension for tortuosity	D_T	dimensionless	1.3
Fractal dimension for pore size distribution	D_f	dimensionless	1.0
Straight length of the unit matrix block	L_o	m	0.15
Shale density	ρ_{rock}	kg/m^3	2659.06
Standard gas density	ρ_{STG}	kg/m^3	0.68
Well radius	r_w	m	0.01
Fracture width	h_w	m	0.015

6.2.3 Heterogeneity Characterization Using Fuzzy Statistical Method

Fuzzy statistical method is an effective tool for modeling complex mathematical problems with uncertain parameters such as seismic analyses, artificial neural networks, and lithology identifications (Nikravesh and Aminzadeh, 2001; Saggaf and Nebrija, 2003; Long et al., 2016). You et al. (2019) first employed the fuzzy nearness and the probability distribution of evaluation function in fuzzy statistical method to quantify the fracture heterogeneity. In this work, the fuzzy statistical method is applied to evaluate the impact of structural parameters (r_{max}, D_f, D_T) on the

flow rate due to reservoir heterogeneity based on the Eqs. 6.11-6.16. Firstly, the optimal structural parameters are acquired with the help of the optimization methods such as the genetic algorithm and the ensemble smoother algorithm (Fan et al., 2019). Meanwhile, the root mean square error is used as the objective function (i.e., Eq. 6.17) to evaluate the deviation between the simulated gas flow rate and the real production rate.

$$\arg\min f(r_{\max}, D_T, D_f) = \sqrt{\sum_{i=1}^{I}\left(Q_{sim}^{\boldsymbol{m}} - Q_{real}^{\boldsymbol{m}}\right)^2 / I} \tag{6.17}$$

The optimal structural parameters obtained by Eq. 6.17 are set as the base parameters for the homogeneous model. To represent the heterogeneity based on the homogeneous model, structural parameters are parameterized with prior distributions. r_{max}, D_f, and D_T are quantified as normal distribution following $N(\bar{r}_{\max}, \sigma)$, $N(\bar{D}_T, \sigma)$, and $N(\bar{D}_f, \sigma)$, respectively. Since the mean values of distributions are determined, the uncertainty of structural parameters is only reflected by the unknown standard deviations of distributions. In other words, the impact of shale matrix structures on gas flow rate can be analyzed by evaluating the consequences of standard deviation variability. Such a process is carried out in the frame of Monte Carlo (MC) simulation because unknown prior distributions of structural parameters prevent from obtaining analytical solutions, but the MC simulation is capable to acquire estimates by means of sampling numerous random numbers from unknown distributions (Gascard and Simeu-Abazi. 2018). Then, at each standard deviation, a large amount of gas flow rate which correspond to different groups of structural parameters can be calculated. To further evaluate the accuracy of heterogeneous model, the distribution of evaluation function which characterizes the superiority of accuracy between the homogeneous and heterogeneous model is calculated by a Boolean type membership function, PD_σ, as follows (You et al., 2019).

$$PD_{\sigma} = \frac{\alpha}{W}\sum_{i=1}^{W}\delta_i; \quad \delta_i = \begin{cases} 0 & RMSE_{HM} > RMSE_{HE} \\ 1 & RMSE_{HM} \le RMSE_{HE} \end{cases} \tag{6.18}$$

where W is sample size, α is fitting parameter to adjust the membership degree within the [0,1] range. $RMSE_{HM}$ and $RMSE_{HE}$ are the root mean squared error between the simulated and realistic gas flow rates for the homogeneous and heterogeneous model, respectively. The process to evaluate the heterogeneity model is illustrated in Figure 6.2.

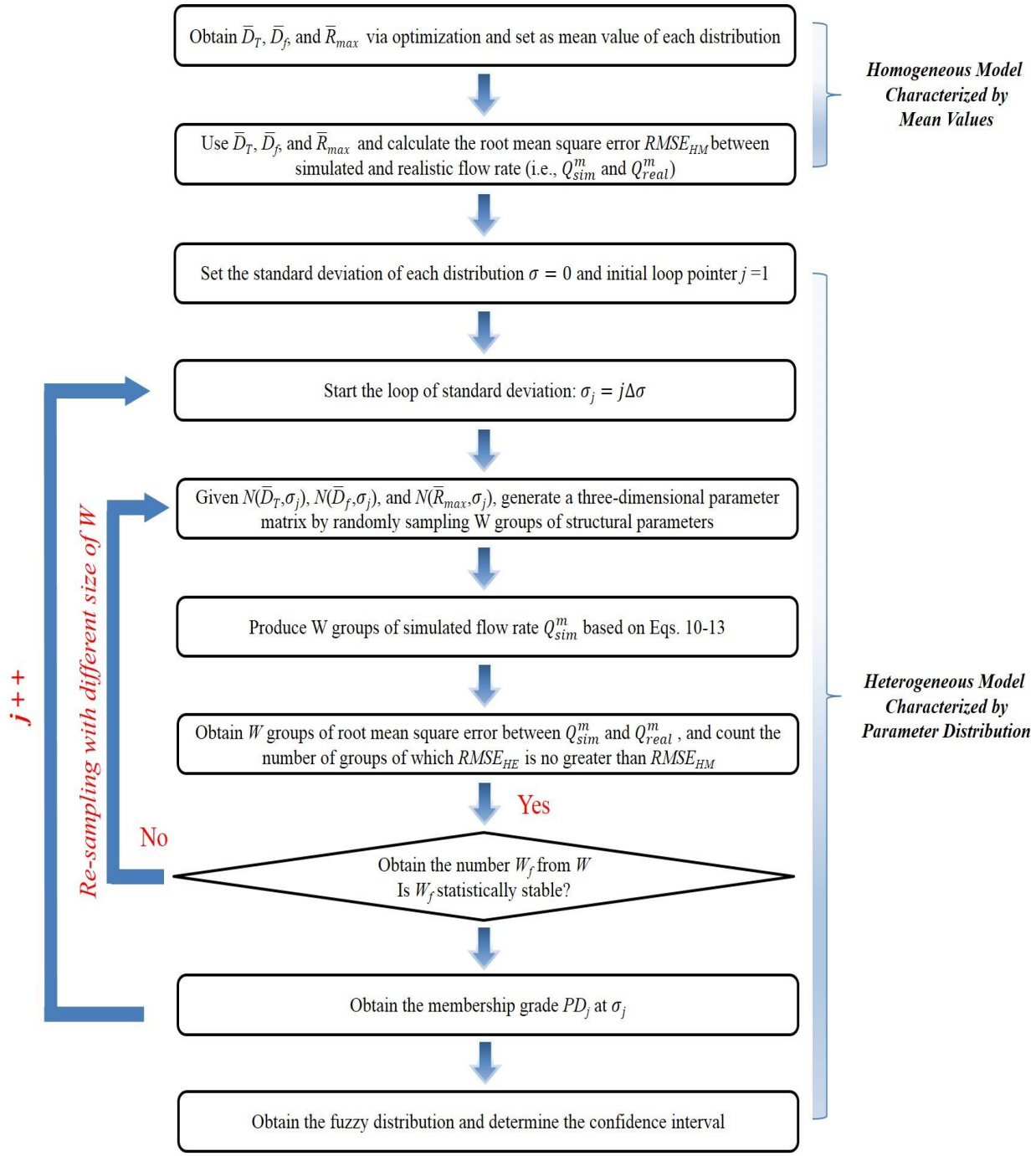

Figure 6.2: Flowchart of the fuzzy statistical method for the heterogeneous model.

6.3 Results and Discussion

To investigate the shale gas flow performance in the simplified dual-porosity system, the profile of pressure is simulated as shown in Figure 6.3. Note that the simulation is only run in a small

scale within a duration of 50 days given the exorbitant computational expenditure. In Figure 6.3, the color from yellow to blue indicates the decrease of pressures. It is seen that the pressure in shale matrix gradually decline due to the gas depletion to the hydraulic fracture, and then the gas transports from the fracture to the horizontal well in production. By comparison, the pressure in the hydraulic fracture drops much faster than the decline in the shale matrix because of the higher permeability (e.g., 50000 md).

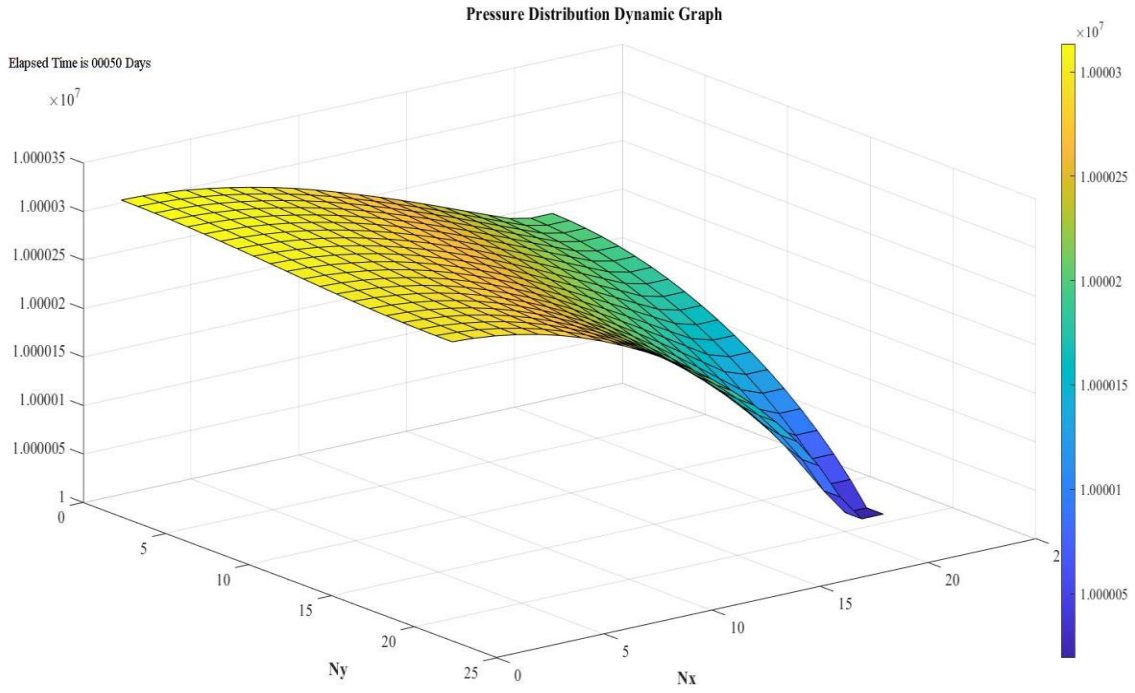

Figure 6.3: Pressure profile characterized by the discretized blocks in the dual-porosity system at the 50th day. The color from yellow to blue indicates the increase of pressures.

The tornado plot is utilized to analyze the influence of structural parameters on methane apparent permeability characterized by the homogeneous shale gas model in the unit block (i.e., Eq. 6.11) under reservoir pressures from 3.0 to 50.0 MPa. The apparent permeability baseline of the tornado plot is calculated using the parameters in Table 6.1. Besides, D_T, D_f, ϕ, R_{max}, and R_{min} are given as

1.5, 1.0, 0.05, 100 nm, and 2 nm, respectively. Subsequently, a 50% adjustment of the given structural parameters is carried out positively and negatively for the sensitivity analysis. Then, the maximum and minimum relative errors of the simulated apparent permeability with respect to the baseline are acquired as displayed in Figure 6.4. It is noticed that the tortuosity fractal dimension presents the largest impact on the apparent permeability which varies beyond 100%. The maximum pore radius exerts the second largest influence changing from -64.65% to 83.72%. In contrast, the minimum pore radius shows the least influence which can be negligible. According to the tornado plot, D_T, D_f, and R_{max} have dominant influences on the apparent permeability compared with ϕ and R_{min}. This indicates the importance of the fractal dimension of structural parameters and implies the tortuosity fractal dimension might be more critical for the gas transport than the pore size fractal dimension in shale matrix.

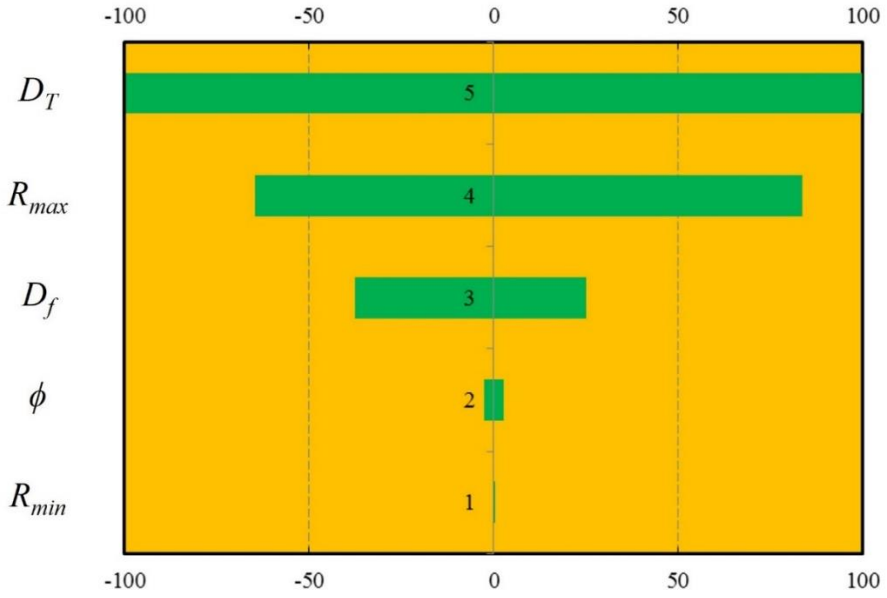

Figure 6.4: The tornado plot indicating the impacts of structural parameters on the apparent permeability in the upscaled unit matrix block.

Based on the sensitivity analysis in the unit shale block, only D_T, D_f, and R_{max} are further studied for the structural parameters influence on the gas flow rate in the horizontal well. As is illustrated in Figure 6.5, the optimized values of structural parameters are set up as the reference inputs to calculate the baseline of the gas flow rate in the duration of 50 days. Subsequently, the reference dataset is adjusted by 50% positively and negatively to generate inputs for the sensitivity analysis. The production profiles on the first row, the second row, and the third row correspond to the positive adjusted dataset, the negative adjusted dataset, and the reference dataset, respectively. It is found that the gas flow rate increases first and then gradually decrease with a long tail. This is consistent with the observed production rate in the field. In addition, it is observed that D_T has the most significant impact on the gas flow rate. In contrast, the D_f and R_{max} present similar impacts on the gas flow rate given the proximity in the curve shape and scale. This observation indicates that the fractal dimension for the tortuosity is more significant in the shale development which may be related to the stratification of the shale rocks.

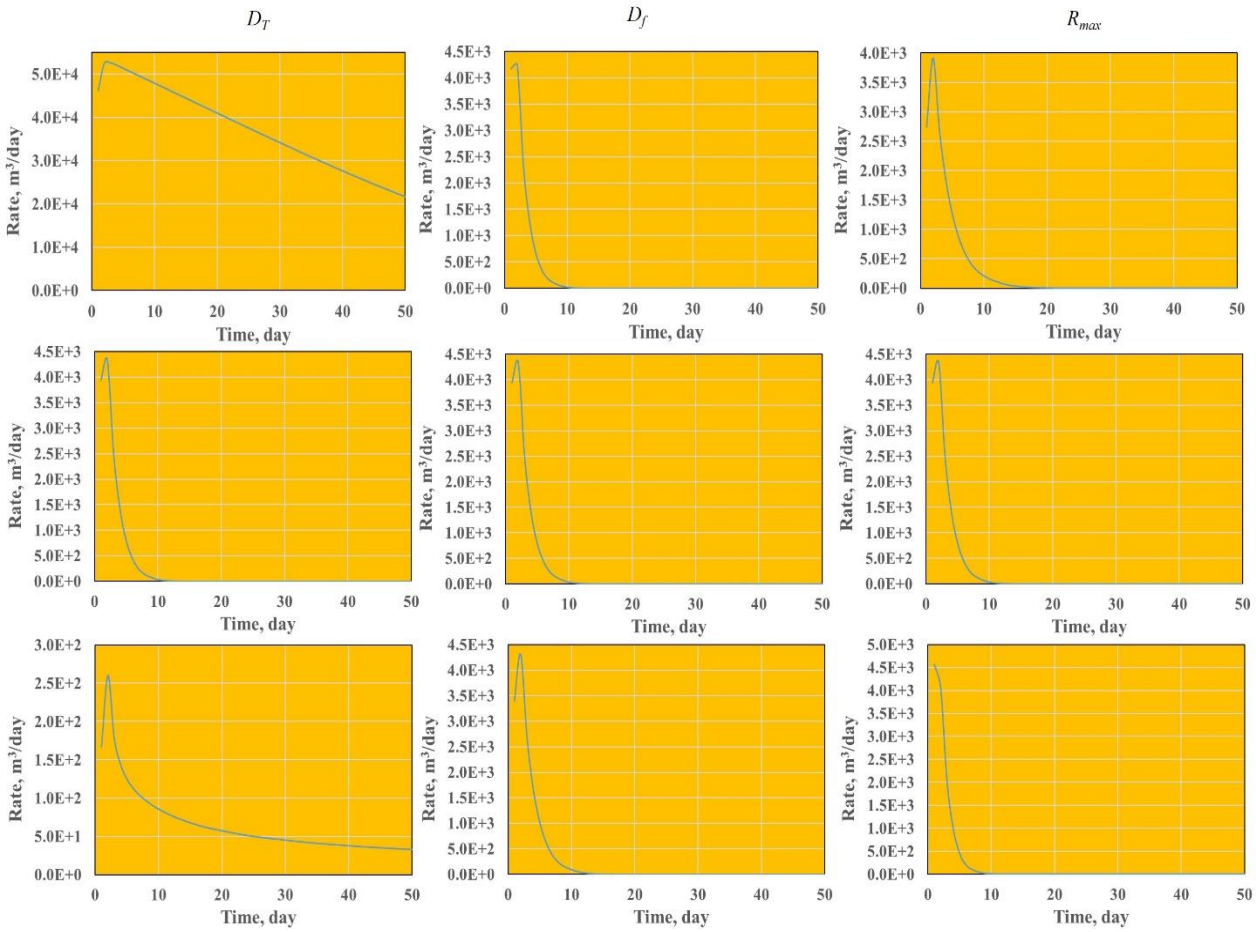

Figure 6.5: Sensitivity analyses of matrix structural parameters. The first, second and third column correspond to the influence of D_T, D_f, and R_{max} on the gas flow rate in horizontal well in the duration of 50 days.

Then, the fuzzy statistical method is implemented to quantify the uncertainty of production due to the reservoir heterogeneity. In the simulation, the varying bottom pressure data from the horizontal well in Fuling, China (You et al., 2019) are adopted as shown in Figure 6.6. It is noticed that the bottom pressures fluctuate in the decreasing trend as the production continues, and the fluctuation degree could change from -36.9 % to 25.0 % with respect to the average bottom pressure. The obvious oscillation is present between 53 to 238 days which spans over 6 months. This indicates that the fluctuations in the realistic production data cannot be avoided and ignored in the shale gas production prediction.

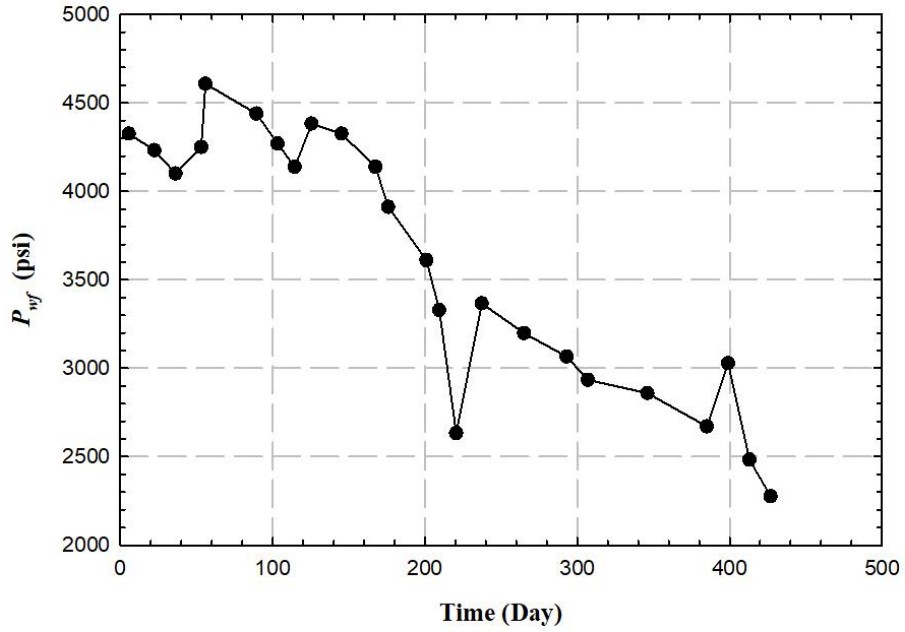

Figure 6.6: Bottom pressures at horizontal well in Fuling, China. The black dots show the collected bottom-hole pressure data within 450 days.

Subsequently, the Monte Carlo simulation is implemented: at each standard deviation from 0.001 to 2.00, the structural parameters from three distributions are randomly sampled to simulate the gas flow rate. Note that the sampling size W is not a fixed number because it is related to the stability of W which is caused by the randomness of Monte Carlo simulation. In the simulation, the W is typically set as 50. The membership distribution is illustrated in Figure 6.7. It is seen that the distribution curve drops from 0.96 to 0.09 as the standard deviation increases from 0.001 to 2.00. The decrease of curve indicates the closeness between the homogeneous model and heterogeneous model drops with the increment of the heterogeneity. In addition, it is observed that the distribution maintains above 0.90 within the standard deviation from 0.001 to 0.006 which is set as the confidence interval. It shows that within the confidence interval of the heterogeneous model, it is likely to obtain the identical flow rate with the homogeneous model. It also indicates

that the heterogeneity of structural parameters within the standard deviation of 0.006 would not generate significant influences on the optimization process for the flow rate. For the practical use, the fluctuations of the membership grades can be smoothed by the fuzzy distribution function (You et al., 2019). In addition, in Figure 6.8 three different curves are present indicating the realistic production rate (black dot curve), the simulated production rate for the heterogeneous model (blue dot curve), and the simulated production rate for the homogeneous model (red dot curve). The result of homogeneous model is simulated using the optimized parameters. Moreover, it shows that slightly better results could be achieved using the heterogeneous model. The obtained flow rate obtained from the heterogeneous model within the confidence interval presents identical trend as the homogeneous model.

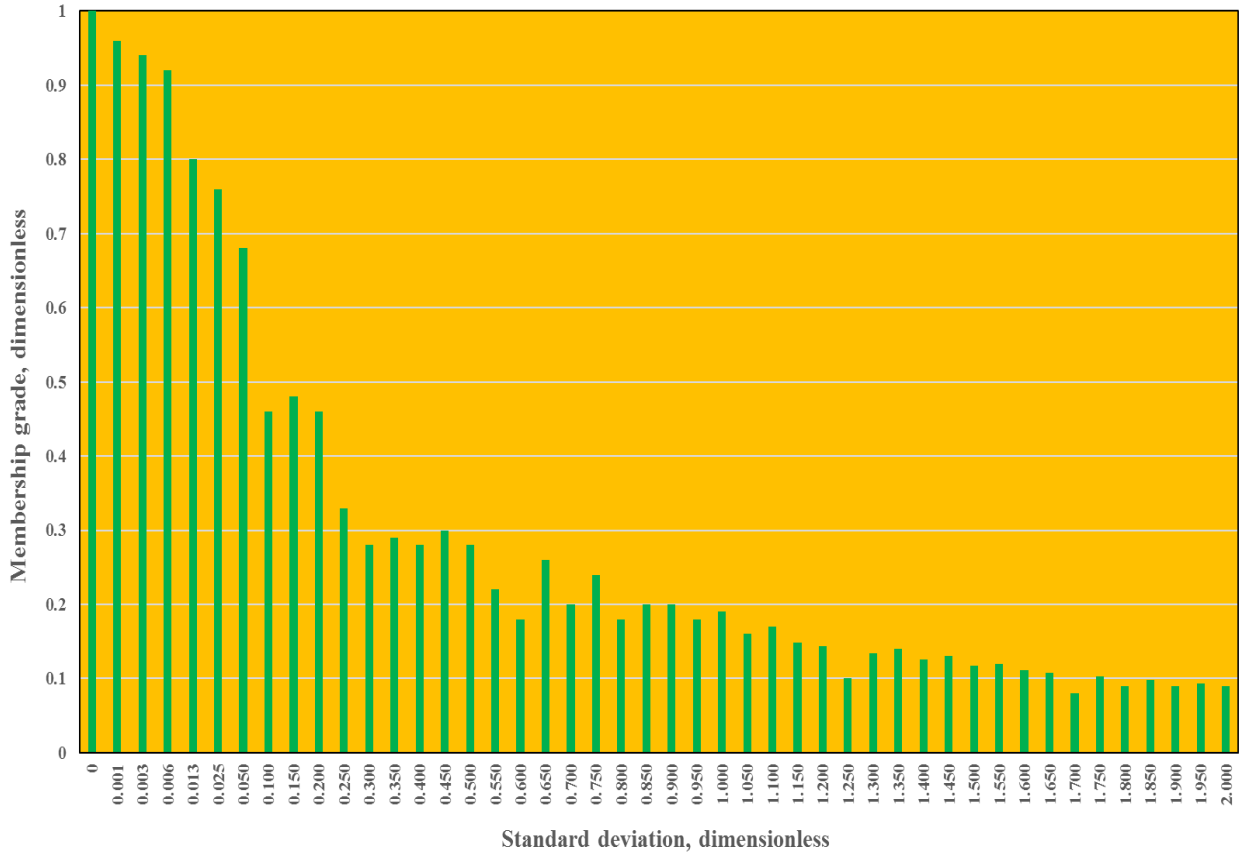

Figure 6.7: Membership distribution with the standard deviation from 0.00 to 2.00. Note that the illustrated standard deviation is not uniformly marked.

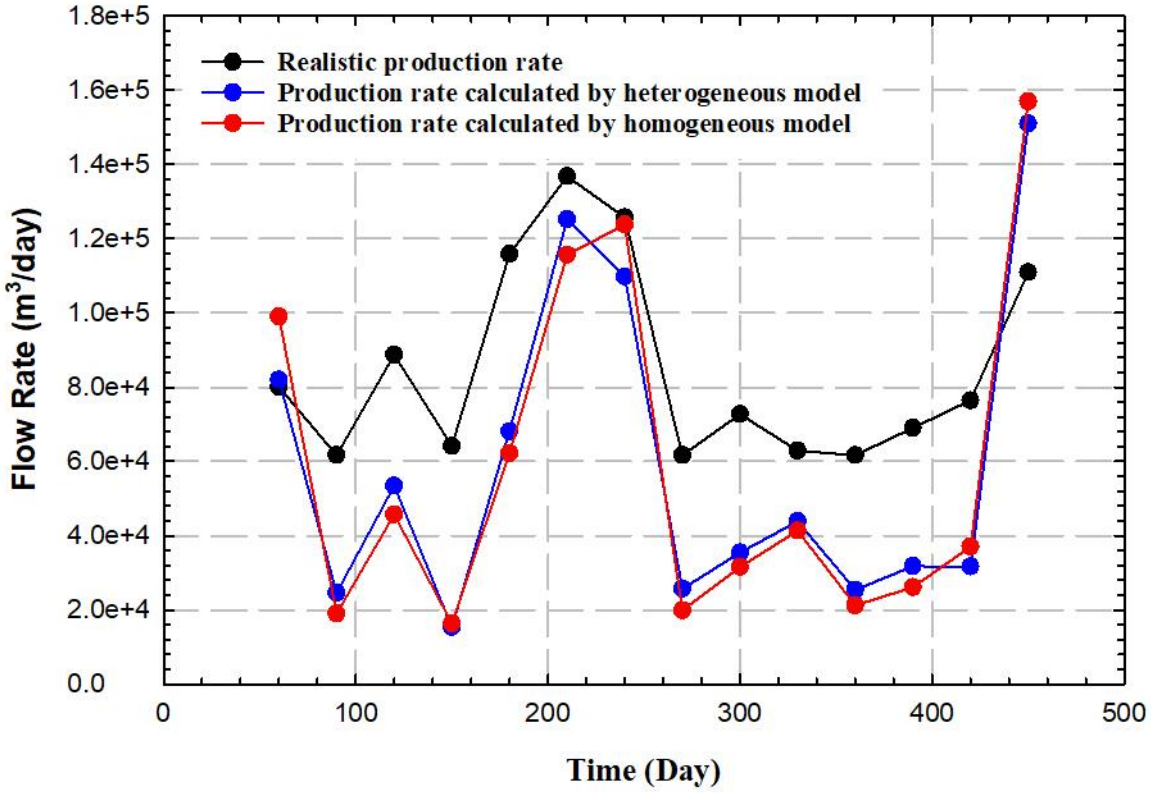

Figure 6.8: Flow rate of horizontal well for the realistic production (blue dot curve), heterogeneous model (orange dot curve), and homogeneous model (grey dot curve), respectively.

6.4 Summary

In this work, a fractal model is proposed to characterize the disordered pore structure and the multiscale effect on gas flow rate in the matrix-fracture dual-porosity system. The fuzzy statistical method is utilized to quantify the uncertainty of production rate because of the changing structural parameters. It is found that the fractal dimension of the tortuosity has the largest impact on the production rate than the pore size and the fractal dimension of pore size distribution. In addition, the fuzzy statistical method can quantify the confidence interval within which the satisfactory flow rate results can be acquired. The fuzzy statistical method enables more flexibility to predict the realistic production profile with significant fluctuation data.

CHAPTER 7: CONCLUSIONS

In this dissertation, a systematic framework is proposed to characterize the shale gas flow behaviors in the organic-rich shale formation. Three scales of gas transport are developed including the analytical model in nanopores, the numerical simulation in shale matrix, and the dual-porosity numerical scheme in the hydraulic-fractured formation.

At pore scale, the new analytical model considering viscous flow, Knudsen diffusion, and surface diffusion has been successfully developed to compute the gas transport over the full flow regime in both organic and inorganic pores where the virtual boundary between the viscous flow and Knudsen diffusion zones is firstly determined based on an analytical molecular kinetics approach. It is discovered that the rarefaction in nanopores is justified to be represented by the weighted Knudsen diffusion and slip flow. Besides, the Knudsen number of real gas flow increasingly deviates from that of ideal gas flow due to the impact of real gas effect at high pressures (≥ 20.0 MPa). Moreover, the increasing viscosity due to the real gas effect can reduce the total molar flux in the inorganic pores up to 66.0% under typical shale gas reservoir condition. In addition, it is found that the apparent permeability decreases with pressure in the pore size smaller than 100 nm and such a decline is more distinct as pore size shrinks. Given inorganic nanopores, the viscous flow is important at any pore sizes under reservoir conditions and the Knudsen diffusion cannot be neglected in the pore size below 5 nm under reservoir conditions and in the pore size below 10 nm when pressure is from 5.0 to 12.0 MPa, respectively. Given organic nanopores, the contribution of surface diffusion plays a dominant role when the pore size is below 20 nm and cannot be neglected when the pore size is below 150 nm. Meanwhile, the viscous flow is important when the pore size is larger than 80 nm and the Knudsen diffusion can be ignored under reservoir conditions.

Subsequently, a novel comprehensive model is proposed which is first coupled with multilayer adsorption, surface diffusion, and pore-confinement effect, and has been successfully validated using the efficient Batch-EnRML optimization method. It is found that the apparent permeability increases significantly as the adsorption layer number increases and the application of Langmuir model in existing gas transport models may extensively underestimate the apparent permeability. In addition, it is found the pore confinement effect is only in presence below the pore size of 50 nm, and the pore confinement effect declines significantly as the pore size approaches 50 nm. Furthermore, the significant increase of gas viscosity due to real gas effect under reservoir conditions cannot be ignored. The enhancement of pore confinement effect and multilayer adsorption can increase the real gas compressibility factor. In contrast, the coupling effect from pore-confinement and real gas effect exerts opposite impacts on methane viscosity at high and relatively low pressures.

The shale gas apparent permeability model is upscaled from nanopores to the shale core scale by the numerical method. Moreover, multiple mechanisms are incorporated and simplified to facilitate the simulation for practicability. Also, the numerical method can be applied for the pulse-decay test to calculate the petrophysical properties. In addition, the unknown shale properties can be estimated by the optimization method based on the numerical scheme. Next, a fractal model is proposed to characterize the disordered pore structure and the multiscale effect on gas flow rate in the matrix-fracture dual-porosity system. The fuzzy statistical method is utilized to quantify the uncertainty of production rate because of the changing structural parameters. It is found that the fractal dimension of the tortuosity has the largest impact on the production rate than the pore size

and the fractal dimension of pore size distribution. In addition, the fuzzy statistical method can quantify the confidence interval within which the satisfactory flow rate results can be acquired. The fuzzy statistical method enables more flexibility to predict the realistic production profile with significant fluctuation data.

REFERENCES

Adler, P.M. 1992. Porous Media: Geometry and Transports. Butterworth-Heinemann, NewYork.

Adzumi, H. 1937. Studies on the Flow of Gaseous Mixtures through Capillaries. I. The Viscosity of Binary Gaseous Mixtures. Bulletin of the Chemical Society of Japan, 1937, 12(5): 199-226.

Akkutlu, I.Y., Efendiev, Y., and Savatorova, V. 2015. Multi-Scale Asymptotic Analysis of Gas Transport in Shale Matrix. Transport in Porous Media, 107(1): 235-260.

Akkutlu, I.Y. and Fathi, E. 2012. Multiscale Gas Transport in Shales with Local Kerogen Heterogeneities. SPE Journal, 17(4): 1002-1011.

Al-Hussainy, R., Ramey, H.J., and Crawford, P.B. 1966. The Flow of Real Gases through Porous Media. Journal of Petroleum Technology, 18(5): 624-636.

Ali, I. and Malik, A.N. 2016. A Realistic Transport Model with Pressure-Dependent Parameters for Gas Flow in Tight Porous Media with Application to Determining Shale Rock Properties. Transport in Porous Media, 124(3): 723-742.

Alnoaimi, K.R. and Kovscek, A.R. 2013. Experimental and Numerical Analysis of Gas Transport in Shale Including the Role of Sorption. SPE-166375, presented at the SPE Annual Technical Conference and Exhibition, 30 September-2 October, New Orleans, LA.

Ambrose, R.J., Hartman, R.C., Diaz-Campos, M., Akkutlu, I.Y., and Sondergeld, C.H. 2012. Shale Gas-in-Place Calculations Part I: New Pore-Scale Considerations. SPE Journal, 17(1): 219-229.

Arkilic, E.B., Schmidt, M.A., and Breuer, K.S. 1997. Gaseous Slip Flow in Long Microchannels. Journal of Microelectromechanical Systems, 6(2): 167-178.

Azom, P.N. and Javadpour, F. 2012. Dual-Continuum Modeling of Shale and Tight Gas Reservoirs. Presented at SPE Annual Technical Conference and Exhibition, 8-10 October, San Antonio, Texas, USA.

Beskok, A. and Karniadakis, G.E. 1999. A Model for Flows in Channels, Pipes, and Ducts at Micro and Nano Scales. Microscale Thermophysical Engineering, 3(1): 43-77.

Binder, K., Horbach, J., Kob, W., Paul, W., and Varnik, F. 2004. Molecular Dynamics Simulations. Journal of Physics: Condensed Matter, 16(5): 429-453.

Bird, G.A. 1994. Molecular Gas Dynamics and the Direct Simulation of Gas Flows. Oxford University Press, Oxford, UK.

Bousige, C., Ghimbeu, C.M., Vix-Guterl, C., Pomerantz, A.E., Suleimenova, A., Vaughan, G., Garbarino, G., Feygenson, M., Wildgruber, C., Ulm, F.J., Pellenq, R.J., Coasne, B. 2016. Realistic Molecular Model of Kerogen's Nanostructure. Nature Materials, 15(5): 576-582.

Bowker, K.A. 2007. Barnett Shale Gas Production, Fort Worth Basin: Issues and Discussion. AAPG Bulletin, 91(4): 523-533.

Bravo, M.C. 2007. Effect of Transition from Slip to Free Molecular Flow on Gas Transport in Porous Media. Journal of Applied Physics, 102(7): 1-10.

Brown, G.P., Dinardo, A., Cheng, G.K., and Thomas K.S. 1946. The flow of Gases in Pipes at Low Pressures. Journal of Applied Physics, 17(10): 802-813.

Brunauer, S., Emmett, P.H., and Teller, E. 1938. Adsorption of Gases in Multimolecular Layers. Journal of American Chemical Society, 60(2): 309-319.

Bui, K. and Akkutlu, I.Y. 2017. Hydrocarbons Recovery from Model-Kerogen Nanopores. SPE Journal, 22(3): 854-862.

Carmichael, D.G. 1980. Computation of Pareto Optima in Structural Design. International Journal for Numerical Methods in Engineering, 15(6): 925-952.

Cercignani, C. 1964. Higher Order Slip According to the Linearized Boltzmann Equation. Institute of Engineering Research Report AS-64-19: University of California, Berkeley.

Chai, D. and Li, X. 2017. Characterization of Nanoscale Gas Transport in Shale Formations, AGU Fall Meeting, New Orleans.

Chai, D., Fan, Z., and Li, X. 2018. A Unified Convection-Diffusion Layered Model for Non-Ideal Rarefied Gas Flow in Nanoscale Porous Media. Presented at the 16th European Conference on the Mathematics of Oil Recovery, 3-6 September, Barcelona, Spain.

Chai, D., Fan, Z., and Li, X. 2019a. A New Unified Gas Transport Model for Gas Flow in Nano-Scale Porous Media. SPE Journal, 24(2): 1-22.

Chai, D., Yang, G., Fan, Z., and Li, X. 2019b. Gas Transport in Shale Matrix Coupling Multilayer Adsorption and Pore Confinement Effect. Chemical Engineering Journal, 370: 1534-1549.

Chai, D. and Li, X. 2020. Gas Apparent Permeability Prediction in Heterogeneous Shale Matrix Based on Fractal Theory and Fuzzy Statistical Method. Unconventional Resources Technology Conference, Austin, Texas.

Chalmers, G.R., Bustin, R.M., and Power, I.M. 2012. Characterization of Gas Shale Pore Systems by Porosimetry, Pycnometry, Surface Area, and Field Emission Scanning Electron Microscopy/Transmission Electron Microscopy Image Analyses: Examples from the Barnett, Woodford, Haynesville, Marcellus, and Doig Units. AAPG Bulletin, 2012, 96(6): 1099-1119.

Chapman, S., and Cowling, T.G. 1952. The Mathematical Theory of Non-Uniform Gases. Cambridge Engineering University Press, Cambridge, UK.

Chen, S. and Doolen, G. 1998. Lattice Boltzmann Method for Fluid Flows. Annual Review of Fluid Mechanics, 30: 329-364.

Chen, Y. and Oliver, D.S. 2012. Ensemble Randomized Maximum Likelihood Method as an Iterative Ensemble Smoother. Mathematical Geosciences, 44(1): 1-26.

Chen, Y.D. and Yang, R.T. 1991. Concentration Dependence of Surface Diffusion and Zeolitic Diffusion. AIChE Journal, 37(10): 1579-1582.

Chen, C., Hu, D., Westacott, D., and Loveless, D. 2013. Nanometer-Scale Characterization of Microscopic Pores in Shale Kerogen by Image Analysis and Pore-Scale Modeling. Geochemistry, Geophysics, Geosystems, 14, 4066-4075.

Chen, L., Zhang, L., Kang, Q., Viswanathan, H.S., Yao, J., and Tao, W. 2015. Nanoscale Simulation of Shale Transport Properties Using the Lattice Boltzmann Method: Permeability and Diffusivity. Scientific Reports, 5: 8089.

Choi, J.G., Do. D.D., and DO, H.D. 2001. Surface Diffusion of Adsorbed Molecules in Porous Media: Monolayer, Multilayer, and Capillary Condensation Regimes. Industrial and Engineering Chemistry Research, 40(19): 4005-4031.

Christou, C. and Dadzie, S.K. 2015. Direct Simulation Monte Carlo Method in Porous Media with Varying Knudsen Number. SPE-173314, presented at the SPE Reservoir Simulation Symposium, 23-25 February, Houston, TX, USA.

Civan, F. 2010. Effective Correlation of Apparent Gas Permeability in Low-Permeability Porous Media. Transport in Porous Media, 82(2): 375-384.

Civan, F., Rai, C.S., and Sondergeld, C.H. 2011. Shale-Gas Permeability and Diffusivity Inferred by Improved Formulation of Relevant Retention and Transport Mechanisms. Transport in Porous Media, 86(3): 925-944.

Clarkson, C.R., Bustin, R.M., and Levy, J.H. 1997. Application of the Monolayer/Multilayer and Adsorption Potential Theories to Coal Methane Adsorption Isotherms at Elevated Temperature and Pressure. Carbon, 35(12): 1689-1705.

Clarkson, C.R., Solano, N., Bustin, R.M. Bustin, A.M.M., Chalmers, G.R.L., He, L., Melnichenko, Y.B., Radliński, A.P., and Blach, T.P. 2013. Pore Structure Characterization of North American Shale Gas Reservoirs Using USANS/SANS, Gas Adsorption, and Mercury Intrusion. Fuel, 103: 606-616.

Coppens, M.O. and Dammers, A.J. 2006. Effects of Heterogeneity on Diffusion in Nanopores—From Inorganic Materials to Protein Crystals and Ion Channels. Fluid Phase Equilibria, 241(1): 308-316.

Cui, X., Bustin, A.M., and Bustin, R. 2009. Measurements of Gas Permeability and Diffusivity of Tight Reservoir Rocks, Different Approaches and Their Applications. Geofluids, 9(3): 208-223.

Cunningham, R.E. and Williams, R.J.J. 1980. Diffusion in Gases and Porous Media, Plenum Press, New York.

Curtis, J.B. 2002. Fractured shale-gas systems. AAPG Bulletin, 86(11): 1921-1938.

Darabi, H., Ettehad, A., Javadpour, F., and Sepehrnoori, K. 2012. Gas Flow in Ultra-Tight Shale Strata. Journal of Fluid Mechanics, 710: 641-658.

Darrah, T.H., Vengosh, A., Jackson, R.B., Warner, N.R., and Poreda, R.J. 2014. Noble Gases Identify the Mechanisms of Fugitive Gas Contamination in Drinking-Water Wells Overlying the Marcellus and Barnett Shales. Proceedings of the National Academy of Sciences, 111(39): 14076-14081.

Didar, B.R. and Akkutlu, I.Y. 2013. Pore-size Dependence of Fluid Phase Behavior and Properties in Organic-Rich Shale Reservoirs. SPE-164099, presented at SPE International Symposium on Oilfield Chemistry, 8-10 April, Woodlands, TX.

Do, H.D., Do, D.D., and Prasetyo, I. 2001. Surface Diffusion and Adsorption of Hydrocarbons in Activated Carbon. AIChE Journal, 47(11): 2515-2525.

Dong, H. and Blunt, M.J. 2009. Pore-Network Extraction from Micro- Computerized-Tomography Images. Physical Review E, 80(3): 036307.

Doyen, P.M. 1988. Permeability, Conductivity, and Pore Geometry of Sandstone, Journal of Geophysical Research, 93(B7): 7729-7740.

Energy Information Administration (EIA). 2013. Annual Energy Outlook.

Energy Information Administration (EIA). 2018. Annual Energy Outlook.

Ertekin, T., King, G.A., and Schwerer, F. 1986. Dynamic Gas Slippage: A Unique Dual-Mechanism Approach to the Flow of Gas in Tight Formations. SPE Formation Evaluation, 1(1): 43-52.

Ewart, T., Perrier, P., Graur, I., and Méolans, J.G. 2007. Tangential Momentum Accommodation in Microtube. Microfluid Nanofluidics, 3(6): 689-695.

Fan, Z., Yang, D., Chai, D., and Li, X. 2018. Estimation of Relative Permeability and Capillary Pressure for PUNQ-S3 Model Using a Modified Iterative Ensemble Smoother. Journal of Energy Resource Technology, 141(2): 1-9.

Fathi, E. and Akkutlu, I.Y. 2009. Nonlinear Sorption Kinetics and Surface Diffusion Effects on Gas Transport in Low-permeability Formations. SPE-124478, presented at the SPE Annual Technical Conference and Exhibition, 4-7 October, New Orleans, LA.

Firouzi, M., Alnoaimi, K., Kovscek, A., and Wilcox, J. 2014. Klinkenberg Effect on Predicting and Measuring Helium Permeability in Gas Shales. International Journal of Coal Geology, 123: 62-68.

Florence, F.A. Rushing, J.A., Newsham, K.E., and Blasingame, T.A. 2007. Improved Permeability Prediction Relations for Low-Permeability Sands. SPE-107954, presented at the SPE Rocky Mountain Oil and Gas Technology Symposium, 16-18 April, Denver, CO.

Frenkel, D. and Smit, B. 2001. Understanding Molecular Simulation (Second Edition). Academic Press, Orlando, FL, USA.

Gad-el-Hak, M. 1999. The Fluid Mechanics of Microdevices — The Freeman Scholar Lecture. Journal of Fluids Engineering, 121(1): 5-33.

Gelb, L., Gubbins, K., Radhakrishnan, R., and Sliwinska-Bartkowiak, M. 1999. Phase Separation in Confined Systems. Reports on Progress in Physics, 62: 1573-1659.

Ghanbarian, B. and Javadpour, F. 2017. Upscaling Pore Pressure-Dependent Gas Permeability in Shales. Journal of Geophysical Research: Solid Earth, 122: 2541-2552.

Guidry, K., Luffel, D., and Curtis, J. 1995. Development of Laboratory and Petrophysical Techniques for Evaluating Shale Reservoirs. Gas Research Institute Report GRI-95/0496, 1995.

Hadjiconstantinou, N.G. 2003. Comment on Cercignani's Second-Order Slip Coefficient. Physics of Fluids, 15: 2352-2354.

Haimes, Y.Y., Lasdon, L.S., and Wismer, D.A. 1971. On a Bicriterion Formulation of the Problems of Integrated System Identification and System Optimization. IEEE Transactions on Systems, Man and Cybernetics, 1(3): 296-297.

Hao, S., Chu, W., Jiang, Q., and Yu, X. 2014. Methane Adsorption Characteristics on Coal Surface above Critical Temperature through Dubinin–Astakhov Model and Langmuir Model. Colloids and Surfaces A: Physicochemical and Engineering Aspects, 444: 104-113.

Hazlett, R.D. 1997. Statistical Characterization and Stochastic Modeling of Pore Networks in Relation to Fluid Flow. Mathematical Geology, 29(6): 801-822.

Higashi, K., Ito, H., and Oishi, J. 1963. Surface Diffusion Phenomena in Gaseous Diffusion: I. Surface Diffusion of Pure Gas. Journal of the Atomic Energy Society of Japan, 5: 846-853.

Hughes, J.D. 2013. A Reality Check on the Shale Revolution. Nature, 497: 307-308.

Hwang, S.T. and Kammermeyer, K. 1966. Surface Diffusion in Microporous Media. The Canadian Journal of Chemical Engineering, 44(2): 82-89.

Ingebrigtsen, T.S. and Dyre, J.C. 2014. The Impact Range for Smooth Wall–Liquid Interactions in Nanoconfined Liquids. Soft Matter, 10(24): 4324-4331.

Javadpour, F., Fisher, D., and Unsworth, M. 2007. Nanoscale Gas Flow in Shale Gas Sediments. Journal of Canadian Petroleum Technology, 46(10): 55-61.

Javadpour, F. 2009. Nanopores and Apparent Permeability of Gas Flow in Mudrocks (Shales and Siltstone). Journal of Canadian Petroleum Technology, 48(8): 16-21.

Jia, B., Tsau, J., and Barati, R. 2018a. Different Flow Behaviors of Low-Pressure and High-Pressure Carbon Dioxide in Shales. SPE Journal, 23(4): 1452-1468.

Jia, B., Tsau, J., and Barati, R. 2018b. A Workflow to Estimate Shale Gas Permeability Variations during the Production Process. Fuel, 220: 879-889.

Jones, F.O. and Owens, W.W. 1980. A Laboratory Study of Low-Permeability Gas Sands. Journal of Petroleum Technology, 1631-1640.

Joekar-Niasar, V. and Hassanizadeh, S.M. 2012. Analysis of Fundamentals of Two-Phase Flow in Porous Media Using Dynamic Pore-Network Models: A Review. Critical Reviews in Environmental Science and Technology, 42(18): 1895-1976.

Kang, S.M., Fathi, E., Ambrose, R.J., Akkutlu, I.Y., and Sigal, R.F. 2011. Carbon Dioxide Storage Capacity of Organic-Rich Shales. SPE Journal, 16(4): 842-855.

Kapoor, A. and Yang, R.T. 1990. Surface Diffusion on Energetically Heterogeneous Surfaces—An Effective Medium Approximation Approach. Chemical Engineering Science, 45(11): 3261-3270.

Karniadakis, G., Beskok, A., and Aluru, N.R. 2005. Microflows and Nanoflows: Fundamentals and Simulations. New York: Springer.

Katz, S., Aminzadeh, F., Long, W., Chilingar, G., and Lackpour, M. 2019. Rock Permeability Forecasts Using Machine Learning and Monte Carlo Committee Machines. Journal of Sustainable Energy Engineering, 4(2): 182-200.

Kazemi, M. and Takbiri-Borujeni, A. 2016. Non-Equilibrium Molecular Dynamics Simulation of Gas Flow in Organic Nanochannels. Journal of Natural Gas Science and Engineering, 33: 1087-1094.

Keehm, Y., Mukerji, T., and Nur, A. 2004. Permeability Prediction from Thin Sections: 3D Reconstruction and Lattice-Boltzmann Flow Simulation. Geophysical Research Letters, 31, L04606.

Kennard, E.H. 1938. Kinetic Theory of Gasses. McGraw-Hill Book Co. Inc., New York.

Kirkpatrick, S. 1973. Percolation and Conduction. Reviews of Modern Physics, 45: 574-588.

Klinkenberg, L.J. 1941. The Permeability of Porous Media to Liquids and Gases. API-41-200, presented at the Drilling and Productions Practices, 1 January, New York, New York.

Könitzer, S.F., Davies, S.J., Stephenson, M.H., and Leng, M.J. 2014. Depositional Controls on Mudstone Lithofacies in a Basinal Setting: Implications for the Delivery of Sedimentary Organic Matter. Journal of Sedimentary Research, 84:198-214.

Kou, Rui, Alafnan, S.F.K., and Akkutlu, I.Y. 2017. Multi-Scale Analysis of Gas Transport Mechanisms in Kerogen. Transport in Porous Media, 116(2): 493-519.

Landauer, R. 1978. Electrical Conductivity in Inhomogeneous Media. AIP Conference Proceedings, 40(1): 2-45.

Landry, C.J., Prodanović, M. and Eichhubl, P. 2016. Direct Simulation of Supercritical Gas Flow in Complex Nanoporous Media and Prediction of Apparent Permeability. International Journal of Coal Geology, 159: 120-134.

Liu, Q. Shen, P., and Yang, P. 2002. Pore Scale Network Modelling of Gas Slippage in Tight Porous Media. Contemporary Mathematics, 295: 367-376.

Loebenstein, W.V. 1971. Calculations and Comparisons of Nonideal Gas Corrections for Use in Gas Adsorption. Journal of Colloid and Interface Science, 36(3): 397-400.

Long, W., Chai, D., and Aminzadeh, F. 2016. Pseudo Density Log Generation Using Artificial Neural Network. SPE Western Regional Meeting, Anchorage, Alaska.

Loucks, R.G., Reed, R.M., Ruppel, S.C., and Jarvie, D.M. 2009. Morphology, Genesis, and Distribution of Nanometer-Scale Pores in Siliceous Mudstones of the Mississippian Barnett Shale. Journal of Sedimentary Research, 79(12): 848-861.

Loucks, R.G., Reed, R.M., Ruppel, S.C., and Hammes, U. 2012. Spectrum of Pore Types and Networks in Mudrocks and a Descriptive Classification for Matrix-Related Mudrock Pores. AAPG Bulletin, 96(6): 1071-1098.

Loyalka, S. and Hamoodi, S. 1990. Poiseuille Flow of a Rarefied Gas in a Cylindrical Tube, Solution of Linearized Boltzmann Equation. Physics of Fluids A: Fluid Dynamics, 2(11): 2061-2065.

Lu, X., Li, F., and Watson, A.T. 1995. Adsorption Measurements in Devonian Shales. Fuel, 74: 599-603.

Mahmoud, M.A. 2013. Development of a New Correlation of Gas Compressibility Factor (Z-Factor) for High Pressure Gas Reservoir. SPE-164587, presented at the North Africa Technical Conference and Exhibition, 15-17 April, Cairo, Egypt.

Majumder, M., Chopra, N., and Hinds, B.J. 2011. Mass Transport through Carbon Nanotube Membranes in Three Different Regimes: Ionic Diffusion and Gas and Liquid Flow. ACS Nano, 5(5): 3867-3877.

Mason, E.A., Malinauskas III, A.P., and Evans, R.B. 1967. Flow and Diffusion of Gases in Porous Media. Journal of Chemical Physics, 46(8): 3199-3216.

Maurer, J., Tabeling, P., Joseph, P., and Willaime, H. 2003. Second-Order Slip Laws in Microchannels for Helium and Nitrogen. Physics of Fluids, 15: 2613-2621.

McCain, W.D. 1990. The Properties of Petroleum Fluids. 2nd Edition, PennWell Books, PennWell Publishing Company, Tulsa.

Mehmani, A., Prodanovic´, M., and Javadpour, F. 2013. Multiscale, Multiphysics Network Modeling of Shale Matrix Gas Flows. Transport in Porous Media, 99(2): 377-390.

Michalis, V.K., Kalarakis, A.N., Skouras, E.D., and Burganos, V.N. 2010. Rarefaction Effects on Gas Viscosity in the Knudsen Transition Regime. Microfluid Nanofluid, 9: 847.

Michel, V.G.G., Sigal, R.F., Civan, F., and Devegowda, D. 2011. Parametric Investigation of Shale Gas Production Considering Nano-Scale Pore Size Distribution, Formation Factor, and Non-

Darcy Flow Mechanisms. SPE-147438, presented at the SPE Annual Technical Conference and Exhibition, 30 October-2 November, Denver, CO.

Middleton, S.R., Gupta, R., Hyman, D.J., and Viswanathan, S.H. 2017. The Shale Gas Revolution: Barriers, Sustainability, and Emerging Opportunities. Applied Energy, 199:88-95.

Milliken, K.L., Rudnicki, M., Awwiller, D.N., and Zhang, T. 2013. Organic Matter-Hosted Pore System, Marcellus Formation (Devonian), Pennsylvania. AAPG Bulletin, 97(2): 177-200.

Miyahara, M. and Gubbins, K. 1997. Freezing/Melting Phenomena for Lennard-Jones Methane in Slit Pores: A Monte Carlo Study. The Journal of Chemical Physics, 106(7): 2865-2880.

Moncrieff, J. 2009. Microstructure of Shale. Presented at SPWLA Annual Meeting, Houston, Texas.

Nelson, P.H. 2009. Pore-Throat Sizes in Sandstones, Tight Sandstones, and Shales. AAPG Bulletin, 93(3): 329-340.

Nordsieck. A. and Hicks, B. 1967. Monte Carlo Evaluation of the Boltzmann Collision Integral. Rarefied Gas Dynamics. Academic Press, New York, 695-710.

Okamoto, N., Kobayashi, K., Liang, Y., Murata, S., Matsuoka, T., Akai, T., and Takagi, S. 2017. Slip Velocity of Methane Flow in Nanopores with Kerogen and Quartz Surfaces. SPE Journal, 23(1): 1-15.

Oran, E., Oh, C., and Cybyk, B. 1998. Direct Simulation Monte Carlo: Recent Advances and Applications. Annual Review of Fluid Mechanics, 30: 403-441.

Passey, Q.R., Bohacs, K.M., Esch, W.L., Klimentidis, R., and Sinha, S. 2010. From Oil-Prone Source Rock to Gas-Producing Shale Reservoir: Geologic and Petrophysical Characterization of Unconventional Shale-Gas Reservoirs. Presented at International Oil and Gas Conference and Exhibition in China, 8-10 June, Beijing, China.

Peng, D. and Robinson, D.B. 1976. A New Two-Constant Equation of State. Industrial and Engineering Chemistry Fundamentals, 15(1): 59-64.

Pong, K.C., Ho, C.M., Liu, J.Q., and Tai, Y.C. 1994. Non-Linear Pressure Distribution in Uniform Micro-Channels. Applications of Microfabrication to Fluid Mechanics. In: ASMEFED, 197: 51-56.

Prud'homme, A. 2014. Hydrofracking: What Everyone Needs to Know. Oxford University Press, Oxford, U.K.

Quiblier, J.A. 1984. A New Three-Dimensional Modeling Technique for Studying Porous Media. Journal of Colloid Interface Science, 98(1): 84-102.

Rahmanian, M.R., Aguilera, R., and Kantzas, A. 2013. A New Unified Diffusion —Viscous-Flow Model Based on Pore-Level Studies of Tight Gas Formations. SPE Journal, 18(1): 38-49.

Ren, W., Li, G., Tian, S., Sheng, M., and Fan, X. 2016. An Analytical Model for Real Gas Flow in Shale Nanopores with Non-Circular Cross-Section. AlChE Journal, 62: 2893-2901.

Revil, A., Woodruff, W.F., Torres-Verdín, C., and Prasad, M. 2013. Complex Conductivity Tensor of Anisotropic Hydrocarbon-Bearing Shales and Mudrocks, Geophysics, 78(6): D403-D418.

Riewchotisakul, S. and Akkutlu, I.Y. 2016. Adsorption Enhanced Transport of Hydrocarbons in Organic Nanopores. SPE Journal, 21(6): 1960-1969.

Roohi, E. and Darbandi, M. 2009. Extending the Navier-Stokes Solutions to Transition Regime in Two-dimensional Micro- and Nanochannel Flows Using Information Preservation Scheme. Physics of Fluids, 21(8): 1-12.

Roth, A. 1982. Vacuum Technology (Revised 2nd edition). Elsevier, Amsterdam: North Holland.

Roy, S., Raju, R., Chuang, H.F., Cruden, B.A., and Meyyappan, M. 2003. Modeling Gas Flow through Microchannels and Nanopores. Journal of Applied Physics, 93(8): 4870-4879.

Ruiz-Canales, P. and Rufian-Lizana, A. 1995. A Characterization of Weakly Efficient Points. Mathematical Programming, 68(1-3): 205-212.

Sahimi, M. 2003. Heterogeneous Materials I: Linear Transport and Optical Properties. Springer, Berlin.

Sakhaee-Pour, A. and Bryant, S. 2012. Gas Permeability of Shale. SPE Reservoir Evaluation and Engineering, 15(4): 401-409.

Sampath, C.W. and Keighin, K. 1982. Factors Affecting Gas Slippage in Tight Sandstones. Journal of Petroleum Technology, 34: 2715-2720.

Santos, J.M. and Akkutlu, I.Y. 2013. Laboratory Measurement of Sorption Isotherm under Confining Stress with Pore-Volume Effects. SPE Journal, 18(5): 924-931.

Schaaf, S.A. and Chambre, P.L. 1961. Flow of Rarefied Gases. Princeton University Press, Princeton.

Scott, D.S. and Dullien, F.A.L. 1962. Diffusion of Ideal Gases in Capillaries and Porous Solids. AIChE Journal, 8: 113-117.

Shen, C. 2005. Rarefied Gas Dynamics: Fundamentals, Simulations and Micro Flows. Springer.

Sheng, G., Wang, W., Zhao, H., Lun, Z., Xu, Y., Zhang, Q., Yu, W., Chai, D., Li, X., and Lou, Y. 2020. Study of Fracturing Fluid Imbibition Impact on Gas-Water Two Phase Flow in Shale Fracture-Matrix System. Unconventional Resources Technology Conference, Austin, Texas.

Silin, D. and Patzek, T. 2006. Pore Space Morphology Analysis Using Maximal Inscribed Spheres. Physica A: Statistical Mechanics Applications, 371(2): 336-360.

Singh, S.K., Sinha, A., Deo, G., and Singh, J.K. 2009. Vapor-Liquid Phase Coexistence, Critical Properties, and Surface Tension of Confined Alkanes. The Journal of Physical Chemistry C, 113(17): 7170-7180.

Singh, H., Javadpour, F., Ettehadtavakkol, A., and Darabi, H. 2014. Nonempirical Apparent Permeability of Shale. SPE Reservoir Evaluation & Engineering, 17(3): 414-424.

Slatt, R.M. and Brien, R.O. 2011. Pore Types in the Barnett and Woodford Gas Shales: Contribution to Understanding Gas Storage and Migration Pathways in Fine-Grained Rocks. AAPG Bulletin, 95(12): 2017-2030.

Smith, D.M. and Williams, F.L. 1984. Diffusional Effects in the Recovery of Methane from Coalbeds. SPE Journal, 24, 529-535.

Sondergeld, C.H., Newsham, K.E., Comisky, K.J., Morgan, C.R., and Rai, C.S. 2010. Petrophysical Considerations in Evaluating and Producing Shale Gas Resources. Presented at SPE Unconventional Gas Conference, 23-25 February, Pittsburgh, Pennsylvania, USA.

Song, W., Yao, J., Li, Y., Sun, H., Zhang, L., Yang, Y., Zhao, J., and Sui, H. 2016. Apparent Gas Permeability in an Organic-Rich Shale Reservoir. Fuel, 181: 973-984.

Sreekanth, A.K. 1969. Slip Flow through Long Circular Tubes. Presented in Proceedings of Sixth International Symposium on Rarefied Gas Dynamics, 1: 667-680.

Srisutthiyakorn, N. and Mavko, G.M. 2017. What is the Role of Tortuosity in the Kozeny-Carman Equation?. Interpretation, 5(1): SB57–SB67.

Standing, M.B. and Katz, D.L. 1942. Density of Natural Gases. Transactions of the AIME, 146(1): 140-149.

Stephenson, M.H. 2016. Shale Gas in North America and Europe. Energy Science and Engineering, 4(1): 4-13.

Sutton, R.P. 2007. Fundamental PVT Calculations for Associated and Gas/Condensate Natural-Gas Systems. SPE Journal, 10 (3), 270-284.

Swami, V., Clarkson, C.R., and Settari, A. 2012. Non-Darcy Flow in Shale Nanopores: Do We Have a Final Answer? SPE-162665, presented at the SPE Canadian Unconventional Resources Conference, 30 October-1 November, Calgary, AB, Canada.

Tahmasebi, P., Hezarkhani, A., and Sahimi, M. 2012. Multiple-Point Geostatistical Modeling Based on the Cross-Correlation Functions. Computational Geosciences, 16(3): 779-797.

Tartakovsky, D.M. 2000. Real Gas Flow through Heterogeneous Porous Media: Theoretical Aspects of Upscaling. Stochastic Environmental Research and Risk Assessment, 14(2): 109-122.

Thomas, M.M. and Clouse, J.A. 1990. Primary Migration by Diffusion through Kerogen: II. Hydrocarbon Diffusivities in Kerogen. Geochimica et Cosmochimica Acta, 54(10): 2781-2792.

Thommes, M., and Findenegg, G.H. 1994. Pore Condensation and Critical-Point Shift of a Fluid in Controlled-Pore Glass. Langmuir, 10(11): 4270-4277.

Tison, S.A. 1993. Experimental Data and Theoretical Modeling of Gas Flows through Metal Capillary Leaks. Vacuum, 44(11-12): 1171-1175.

Veltzke, T. and Thöming, J. 2012. An Analytically Predictive Model for Moderately Rarefied Gas Flow. Journal of Fluid Mechanics, 698: 406-422.

Wang, H., and Marongiu-Porcu, M. 2015. Impact of Shale-Gas Apparent Permeability on Production: Combined Effects of Non-Darcy Flow/Gas-Slippage, Desorption, and Geomechanics. SPE Reservoir Evaluation and Engineering, 18(4): 495-507.

Wang, Q., Chen, X. Jha, A.N., and Rogers, H. 2014. Natural Gas from Shale Formation – The Evolution, Evidences and Challenges of Shale Gas Revolution in United States. Renewable and Sustainable Energy Reviews, 30:1-28.

Wang, J., Luo, H., Liu, H., Cao, F., Li, Z., and Sepehrnoori, K. 2017. An Integrative Model To Simulate Gas Transport and Production Coupled With Gas Adsorption, Non-Darcy Flow, Surface Diffusion, and Stress Dependence in Organic-Shale Reservoirs. SPE Journal, 22(1): 244-264.

Wang, S., Feng, Q., Javadpour, F., Yang, Y. 2016. Breakdown of Fast Mass Transport of Methane through Calcite Nanopores, Journal of Physical Chemistry C, 120(26): 14260-14269.

Wang Q., Wang, T., Liu, W., Zhang, J., Feng, Q., Lu, H., and Peng, P. 2019. Relationships Among Composition, Porosity and Permeability of Longmaxi Shale Reservoir in the Weiyuan Block, Sichuan Basin, China. Marine and Petroleum Geology, 102: 33-47.

Wasaki, A. and Akkutlu, I.Y. 2015. Permeability of Organic-Rich Shale. SPE Journal, 20(6): 1384-1396.

Weida, S.D., Lambert, S.W., and Boyer, C.M. 2005. Challenging the Traditional Coalbed Methane Exploration and Evaluation. SPE-98069, presented at the SPE Eastern Regional Meeting, Morgantown, West Virginia.

Whitaker, S. 1999. The Method of Volume Averaging. Netherlands, Kluwer Academic Publishers.

Wu, K.L., Li, X.F., Guo, C.H., Wang, C.C., and Chen, Z.X. 2016. A Unified Model for Gas Transfer in Nanopores of Shale Gas Reservoirs: Coupling Pore Diffusion and Surface Diffusion. SPE Journal, 21(5): 1583-1611.

Wu, K., Chen, Z., and Li, X. 2015. Real Gas Transport through Nanopores of Varying Cross-section Type and Shape in Shale Gas Reservoirs. Chemical Engineering Journal, 281:813-825.

Wu, K., Dijke, M.I.J., Couples, G.D., Jiang, Z., Ma, J., Sorbie, K.S., Crawford, J., Young, I., and Zhang, X. 2006. 3D Stochastic Modelling of Heterogeneous Porous Media—Applications to Reservoir Rocks. Transport in Porous Media, 65(3): 443-467.

Wu, K., Li, X., Guo, C., Wang, C., and Chen, Z. 2016. A Unified Model for Gas Transfer in Nanopores of Shale Gas Reservoirs: Coupling Pore Diffusion and Surface Diffusion. SPE Journal, 21(5): 1583-1611.

Wu, K.L., Chen, Z.X., Li, J., Li, X.F., Xu, J.Z., and Dong, X.H. 2017. Wettability Effect on Nanoconfined Water Flow. Proceedings of the National Academy of Sciences, 114(13): 3358-3363.

Xiong, X., Devegowda, D., Michel, G.G., Sigal, R.F., and Civan, F. 2012. A Fully-Coupled Free and Adsorptive Phase Transport Model for Shale Gas Reservoirs Including Non-Darcy Flow Effects. SPE-159758-MS, Presented at the SPE Annual Technical Conference and Exhibition, 8–10 October, San Antonio, TX.

Yamaguchi, H., Hanawa, T., Yamamoto, O., Matsuda, Y. Egami, Y., and Niimi, T. 2011. Experimental Measurement on Tangential Momentum Accommodation Coefficient in a Single Microtube, Microfluidics and Nanofluidics, 11(1): 1613-4982.

Yang, R.T., Fenn, J.B., and Haller, G.L. 1973. Modification to the Higashi Model for Surface Diffusion. AIChE Journal, 19(5): 1052-1053.

Yang, G., Chai, D., Fan, Z., and Li, X. 2019a. Analytical Investigation of the Confinement Effect on Capillary Condensation Pressure of Fluids in Nanopores. SPE-195273, presented at SPE Western Regional Meeting, 23-26 April, San Jose, CA.

Yang, G., Chai, D., Fan, Z., and Li, X. 2019b. Capillary Condensation of Single-and Multicomponent Fluids in Nanopores. Industrial & Engineering Chemistry Research, 58(41): 19302-19315.

Yang, G., Fan, Z., and Li, X. 2019c. Determination of Confined Fluid Phase Behavior Using Extended Peng-Robinson Equation of State. Chemical Engineering Journal, 378: 122032.

Yeh, Y.T. and Yang, R.T. 1989. Diffusion in Zeolites Containing Mixed Cations. AIChE Journal, 35(10): 1659-1666.

You, X., Liu, J., Jia, C., Li, J., Liao, X., and Zheng, A. 2019. Production Data Analysis of Shale Gas Using Fractal Model and Fuzzy Theory: Evaluating Fracturing Heterogeneity. Applied Energy, 250:1246-1259.

Yu, H., Fan, J., Chen, J., Zhu, Y., and Wu, H. 2018. Pressure-Dependent Transport Characteristic of Methane Gas in Slit Nanopores. International Journal of Heat and Mass Transfer, 123: 657-667.

Yu, H., Zhu, Y., Jin, X., Liu, H., and Wu, H. 2019. Multiscale Simulations of Shale Gas Transport in Micro/Nano-Porous Shale Matrix Considering Pore Structure Influence. Journal of Natural Gas Science and Engineering, 64: 28-40.

Yu, W., Sepehrnoori, K., and Patzek, T.W. 2016. Modeling Gas Adsorption in Marcellus Shale with Langmuir and BET Isotherms. SPE Journal, 21(2): 589-600.

Zadeh, L.A. 1965. Fuzzy Sets. Information and Control, 8(3):338–53.

Zhao, S. and Alexandroff, A. 2019. Current and Future Struggles to Eliminate Coal. Energy Policy, 129: 511-520.

Zheng, R., Chai, D., Yang, G., Fan, Z., and Li, X. 2019. Analytical Investigations of Permeability for Ultra-Tight Reservoir Rock Based on BET Adsorption Isotherm, AGU Fall Meeting, San Francisco.

Zoback, M. D. and Arent, D. J. 2014. Shale Gas Development Opportunities and Challenges. Proceedings of the National Academy of Sciences.

APPENDIX

A. Derivation of Maxwell Slip Model

Chapman and Cowling (1970) claimed that the slip velocity, u_s, can be roughly expressed as average velocity of two parts including the tangential velocity of molecules from external flow (i.e., u_λ) and ones reflected from the control surface. Moreover, it is presumed that σ fraction of reflected molecules present diffuse reflection and $(1-\sigma)$ fraction of reflected molecules show specular reflection. Thus, slip velocity is given as

$$u_s = \frac{1}{2}\left[u_\lambda + (1-\sigma)u_\lambda + \sigma u_w\right] \tag{A.1}$$

where σ also represents TMAC. Note that u_w is wall tangential velocity which is zero. Since u_λ is at the outer boundary of non-equilibrium layer where the gas behavior is governed by the kinetic theory, it can be defined as an implicit function of mean free path (i.e., λ) which is $u_\lambda = f(\lambda)$. Subsequently, Taylor series expansion of u_λ about u_s up to the second order is implemented as follows.

$$u_\lambda = u_s + \lambda\left(\frac{\partial u}{\partial r}\right)_s + \frac{1}{2}\lambda^2\left(\frac{\partial^2 u}{\partial r^2}\right)_s \tag{A.2}$$

where $\left(\partial u/\partial r\right)_s$ and $\left(\partial^2 u/\partial r^2\right)_s$ denote the first derivative and second derivative of velocity with respect to normal direction of control surface, respectively. Given Eqs. A.1 and A.2, the slip velocity, u_s, can be written as

$$u_s = \frac{2-\sigma}{\sigma}\left[\lambda\left(\frac{\partial u}{\partial r}\right)_s + \frac{1}{2}\lambda^2\left(\frac{\partial^2 u}{\partial r^2}\right)_s\right] \tag{A.3}$$

For the sake of simplicity, σ is equal to 1. Then Eq. A.3 can be generalized as following expression.

$$u_s = C_1 Kn\left(\frac{\partial u}{\partial n}\right)_s + C_2 Kn^2\left(\frac{\partial^2 u}{\partial n^2}\right)_s \tag{A.4}$$

where C_1 and C_2 are slip coefficients for the first and second order terms, respectively.

B. Rearrangement of Advection-Diffusion Model

According to the ADM model, the mass flux, F_t, can be expressed as

$$F_t = w_c F_c + w_f F_f \tag{B.1}$$

Singh et al. (2014) have developed a non-empirical model to describe shale gas flow where weights w_c and w_f are both assigned as unity. Accordingly, Eq. B.1 can be arranged as

$$F_t = -\frac{r_o^2}{8}\frac{\bar{P}M}{\mu RT}\nabla P - \frac{2r_o}{3}\sqrt{\frac{8M}{\pi RT}}\nabla P \tag{B.2}$$

Since Knudsen number is given as $Kn = \mu\sqrt{\pi RT/(2M)}\Big/\left(\bar{P}r_o\right)$, Eq. B.2 can be parameterized with Knudsen number and written as follows.

$$F_t = -\frac{r_o^2}{8}\frac{\bar{P}M}{\mu RT}\nabla P - \frac{8r_o^2}{3}Kn\frac{\bar{P}M}{\mu\pi RT}\nabla P \tag{B.3}$$

Subsequently, Eq. B.3 can be expressed in terms of the first-order velocity model.

$$F_t = -\frac{r_o^2\bar{P}M}{8\mu RT}\left(1+\frac{64}{3\pi}Kn\right)\nabla P \tag{B.4}$$

C. Derivation of Fraction of Inter-Molecular Collisions in the Tube

Chapman and Cowling (1970) derived the expression of molecular properties using Maxwellian velocity distribution. The derivations are based on Maxwell's assumptions: i) the model only treats the simple gas (i.e., molecules in the gas are all identical); ii) gas molecules are spherically symmetrical possessing only energy of translation; and iii) gas molecules are subject to no external forces; iv) the gas is in the Maxwellian velocity distribution and gas density is independent of spatial position and time. Then, the number of molecules in the unit volume during unit time is found by Chapman and Cowling (1970) as

$$\iiint f(\boldsymbol{v})d\boldsymbol{v}\left(\boldsymbol{v}\cdot d\boldsymbol{S}\right)dt \tag{C.1}$$

where $f(\boldsymbol{v})$ is the Maxwellian velocity distribution with respect to the velocity vector $_{\boldsymbol{v}}$, $d\boldsymbol{S}$ is the cross-section surface area vector. Note the direction of $d\boldsymbol{S}$ is normal to the cross-section surface area. The number of molecules in the unit volume of the central zone during the unit time can be expressed based on Eq. C.1,

$$\iiint |\boldsymbol{v}_c| cos\varphi\, f\left(\boldsymbol{v}_c\right)d\boldsymbol{v}dSdt \tag{C.2}$$

where $|\boldsymbol{v}_c|$ is the magnitude of the velocity vector in the central zone, φ is the angle between $\boldsymbol{v}_c$ and $d\boldsymbol{S}$. It is noted that φ should be acute since the flow is along the positive direction. Eq. C.2 can be further simplified as

$$n\overline{|\boldsymbol{v}_c| cos\varphi}dSdt \tag{C.3}$$

where n is the number density, $\overline{|\boldsymbol{v}_c| cos\varphi}$ (i.e., $\bar{V}_{nc}$) is the average velocity component normal to the central zone cross-section. $n\overline{|\boldsymbol{v}_c| cos\varphi}$ in Eq. C.3 is deduced from the relation

$n\overline{|\boldsymbol{v}_c|cos\varphi} = \int |\boldsymbol{v}_c| cos\varphi\, f\,(\boldsymbol{v}_c) d\boldsymbol{v}$ (Chapmen and Cowling, 1970). Thus, the total number of molecules in the central zone with virtual radius of *r* during time Δt is calculated by

$$n\overline{|\boldsymbol{v}_c|cos\varphi}\iint dSdt = n\overline{|\boldsymbol{v}_c|cos\varphi}\pi r^2\Delta t \tag{C.4}$$

Similarly, the total number of molecules in the cylindrical tube (without adsorption layer) with outer radius of R_e during time Δt is determined by

$$n\overline{|\boldsymbol{v}_t|cos\varpi}\pi R_e^2\Delta t \tag{C.5}$$

where $|\boldsymbol{v}_t|$ is the magnitude of the velocity vector in the cylindrical tube (without adsorption layer), ϖ is the angle between $\boldsymbol{v}_t$ and $d\boldsymbol{S}$. $\overline{|\boldsymbol{v}_t|cos\varpi}$ (i.e., $\bar{v}_{nt}$) is the average velocity component normal to the cylindrical-tube cross-section. $\overline{|\boldsymbol{v}_c|cos\varphi}$ (i.e., $\bar{v}_{nc}$) and $\overline{|\boldsymbol{v}_t|cos\varpi}$ (i.e., $\bar{v}_{nt}$) can be constrained by inequalities as follows,

$$0 < \left(\overline{|\boldsymbol{v}_c|cos\varphi} = \frac{1}{x}\sum v_x \cos\varphi_x\right) \le \frac{1}{x}\sum v_x \tag{C.6}$$

$$0 < \left(\overline{|\boldsymbol{v}_t|cos\varpi} = \frac{1}{y}\sum v_y \cos\varpi_y\right) \le \frac{1}{y}\sum v_y \tag{C.7}$$

where *x* and *y* respectively denote the number of molecules in the central zone and cylindrical tubes (without adsorption layer). v_x and v_y respectively denote the individual-molecule velocity magnitude in the central zone and cylindrical tube (without adsorption layer). According to inequalities, we further parameterize Eq. C.6 and Eq. C.7 as follows,

$$\overline{|\boldsymbol{v}_c|cos\varphi} = \chi\frac{1}{x}\sum v_x = \chi\bar{v} \tag{C.8}$$

$$\overline{|\mathbf{v}_t|cos\varpi} = \upsilon \frac{1}{y}\sum v_y = \upsilon\bar{v} \tag{C.9}$$

where χ and υ is the estimate of average cosine function values for central zone and cylindrical tube (without adsorption layer), respectively. According to Eqs. C.4 and C.5, we obtain the number of molecules in the central zone and cylindrical tube (without adsorption layer), respectively,

$$N_c = n\pi r^2 \chi\bar{v}\Delta t = n\pi r^2 \bar{v}_{nc}\Delta t \tag{C.10}$$

$$N_t = n\pi R_e^2 \upsilon\bar{v}\Delta t = n\pi R_e^2 \bar{v}_{nt}\Delta t \tag{C.11}$$

The fraction of inter-molecular collisions in the cylindrical tube can also be derived as

$$\frac{N_c}{N_t} = \frac{n\pi r^2 \chi\bar{v}\Delta t}{n\pi R_e^2 \upsilon\bar{v}\Delta t} = \kappa\frac{r^2}{R_e^{\ 2}} \tag{C.12}$$

D. Expansion of Diffusivity Equation

The $\rho\vec{u}$ term (i.e., momentum gradient with respect to the spatial coordinates) can be expanded coupling Eq. 5.18 as follows.

$$\nabla\cdot\left(\rho\vec{u}\right) = \nabla\cdot\left[\frac{\rho}{\mu}\mathbf{K}\cdot\left(\nabla p + \rho g\nabla H\right)\right] \tag{D.1}$$

Then, Eq. D.1 can be further arranged as

$$
\begin{aligned}
&\nabla\cdot\left[\frac{\rho}{\mu}\mathbf{K}\cdot\left(\nabla p+\rho g\nabla H\right)\right]\\
&=\frac{\partial}{\partial x^l}\overrightarrow{g^l}\cdot\left(\frac{\rho}{\mu}K^{ij}\overrightarrow{g_i}\overrightarrow{g_j}\cdot\frac{\partial p}{\partial x^k}\overrightarrow{g^k}\right)+\nabla\cdot\left[\frac{\rho}{\mu}\mathbf{K}\cdot\left(\rho g\nabla H\right)\right]\\
&=\frac{\partial}{\partial x^l}\overrightarrow{g^l}\cdot\left(\frac{\rho}{\mu}K^{ij}\frac{\partial p}{\partial x^j}\overrightarrow{g_i}\right)+\nabla\cdot\left[\frac{\rho}{\mu}\mathbf{K}\cdot\left(\rho g\nabla H\right)\right]\\
&=\overrightarrow{g^l}\cdot\left[\frac{\partial}{\partial x^l}\left(\frac{\rho}{\mu}K^{ij}\right)\frac{\partial p}{\partial x^j}\overrightarrow{g_i}+\frac{\partial^2 p}{\partial x^l\partial x^j}\left(\frac{\rho}{\mu}K^{ij}\right)\overrightarrow{g_i}+\frac{\rho}{\mu}K^{ij}\frac{\partial p}{\partial x^j}\Gamma_{il}^{p}\overrightarrow{g_p}\right]\\
&+\nabla\cdot\left[\frac{\rho}{\mu}\mathbf{K}\cdot\left(\rho g\nabla H\right)\right]
\end{aligned}
\tag{D.2}
$$

where $\overrightarrow{g_i}$, $\overrightarrow{g_j}$, $\overrightarrow{g_p}$ are unit covariant vectors, $\overrightarrow{g^i}$, $\overrightarrow{g^l}$, $\overrightarrow{g^k}$ are unit contravariant vectors, Γ_{il}^{p} is Christoffel symbol. Note that the Christoffel symbol is not a tensor but it contains all the information about the curvature of the coordinate system and is equal to zero if the coordinates are straightened. Since the coordinate system in the work is Cartesian coordinate, thus the Christoffel symbol is set to be zero. Then, Eq. D.2 can be written as

$$
\begin{aligned}
&\overrightarrow{g^l}\cdot\left[\frac{\partial}{\partial x^l}\left(\frac{\rho}{\mu}K^{ij}\right)\frac{\partial p}{\partial x^j}+\frac{\partial^2 p}{\partial x^l\partial x^j}\left(\frac{\rho}{\mu}K^{ij}\right)\right]\overrightarrow{g_i}+\nabla\cdot\left[\frac{\rho}{\mu}\mathbf{K}\cdot\left(\rho g\nabla H\right)\right]\\
&=\delta_i^l\left[\frac{\partial}{\partial x^l}\left(\frac{\rho}{\mu}K^{ij}\right)\frac{\partial p}{\partial x^j}+\frac{\partial^2 p}{\partial x^l\partial x^j}\left(\frac{\rho}{\mu}K^{ij}\right)\right]+\nabla\cdot\left[\frac{\rho}{\mu}\mathbf{K}\cdot\left(\rho g\nabla H\right)\right]\\
&=\frac{\partial}{\partial x^i}\left(\frac{\rho}{\mu}K^{ij}\right)\frac{\partial p}{\partial x^j}+\frac{\partial^2 p}{\partial x^i\partial x^j}\left(\frac{\rho}{\mu}K^{ij}\right)+\nabla\cdot\left[\frac{\rho}{\mu}\mathbf{K}\cdot\left(\rho g\nabla H\right)\right]
\end{aligned}
\tag{D.3}
$$

Subsequently, Eq. D.3 can be expressed as the follows.

$$
\begin{aligned}
&\frac{\partial}{\partial x^i}\left(\frac{\rho}{\mu}K^{ij}\right)\frac{\partial p}{\partial x^j}+\frac{\partial^2 p}{\partial x^i\partial x^j}\left(\frac{\rho}{\mu}K^{ij}\right)+\nabla\cdot\left[\frac{\rho}{\mu}\mathbf{K}\cdot\left(\rho g\nabla H\right)\right]\\
&=\nabla\cdot\left(\frac{\rho}{\mu}\mathbf{K}\right)\cdot\nabla p+\nabla\nabla p:\left(\frac{\rho}{\mu}\mathbf{K}\right)+\nabla\cdot\left[\frac{\rho}{\mu}\mathbf{K}\cdot\left(\rho g\nabla H\right)\right]
\end{aligned}
\tag{D.4}
$$

If the permeability tensor is simplified as the scalar, then Eq. D.3 can be written as

$$\begin{aligned}&\frac{\partial}{\partial x^i}\left(\frac{\rho}{\mu}K^{ij}\right)\frac{\partial p}{\partial x^j}+\frac{\partial^2 p}{\partial x^i \partial x^j}\left(\frac{\rho}{\mu}K^{ij}\right)+\nabla\cdot\left[\frac{\rho}{\mu}\mathbf{K}\cdot\left(\rho g\nabla H\right)\right]\\&=\nabla\left(\frac{\rho}{\mu}K\right)\cdot\nabla p+\left(\frac{\rho}{\mu}K\right)\nabla^2 p+\nabla\cdot\left[\frac{\rho}{\mu}K\left(\rho g\nabla H\right)\right]\end{aligned} \tag{D.5}$$

E. Discretization of Diffusivity Equation

The right-hand side of Eq. 5.22 can be discretized as following expression. Note that the flow regime is uniformly discretized.

$$\begin{aligned}&\frac{\left(\frac{\rho}{\mu}k_{tr}\frac{\partial p}{\partial x}\right)_{i+\frac{1}{2}}-\left(\frac{\rho}{\mu}k_{tr}\frac{\partial p}{\partial x}\right)_{i-\frac{1}{2}}}{\Delta x}\\&=\left(\frac{\rho k_{tr}}{\mu\left(\Delta x\right)^2}\right)_{i+\frac{1}{2}}\left(p_{i+1}-p_i\right)-\left(\frac{\rho k_{tr}}{\mu\left(\Delta x\right)^2}\right)_{i-\frac{1}{2}}\left(p_i-p_{i-1}\right)\end{aligned} \tag{E.1}$$

The harmonic average is utilized to calculate the fluid properties between the neighboring blocks, which are defined as follows.

$$\left(\frac{\rho k_{tr}}{\mu\left(\Delta x\right)^2}\right)_{i+\frac{1}{2}}=\frac{2\left(\rho k_{tr}\right)_i\left(\rho k_{tr}\right)_{i+1}}{\left(\Delta x\right)^2\left(\rho k_{tr}\right)_{i+1}\mu_i+\left(\Delta x\right)^2\left(\rho k_{tr}\right)_i\mu_{i+1}} \tag{E.2}$$

$$\left(\frac{\rho k_{tr}}{\mu\left(\Delta x\right)^2}\right)_{i-\frac{1}{2}}=\frac{2\left(\rho k_{tr}\right)_i\left(\rho k_{tr}\right)_{i-1}}{\left(\Delta x\right)^2\left(\rho k_{tr}\right)_{i-1}\mu_i+\left(\Delta x\right)^2\left(\rho k_{tr}\right)_i\mu_{i-1}} \tag{E.3}$$

The left-hand side of Eq. 5.22 is discretized as follows.

$$\left[\rho\phi c_1+\left(1-\phi\right)qc_2\right]_i\frac{\partial p}{\partial t}=\left[\rho\phi c_1+\left(1-\phi\right)qc_2\right]_i\frac{p_i^{n+1}-p_i^n}{\Delta t} \tag{E.4}$$